National Library of Canada
Canadian Theses Service
Ottawa, Canada
K1A 0N4

Bibliothèque nationale du Canada
Services des thèses canadiennes

CANADIAN THESES

THÈSES CANADIENNES

NOTICE

The quality of this microfiche is heavily dependent upon the quality of the original thesis submitted for microfilming. Every effort has been made to ensure the highest quality of reproduction possible.

If pages are missing, contact the university which granted the degree.

Some pages may have indistinct print especially if the original pages were typed with a poor typewriter ribbon or if the university sent us an inferior photocopy.

Previously copyrighted materials (journal articles, published tests, etc.) are not filmed.

Reproduction in full or in part of this film is governed by the Canadian Copyright Act, R.S.C. 1970, c. C-30. Please read the authorization forms which accompany this thesis.

AVIS

La qualité de cette microfiche dépend grandement de la qualité de la thèse soumise au microfilmage. Nous avons tout fait pour assurer une qualité supérieure de reproduction.

S'il manque des pages, veuillez communiquer avec l'université qui a conféré le grade.

La qualité d'impression de certaines pages peut laisser à désirer, surtout si les pages originales ont été dactylographiées à l'aide d'un ruban usé ou si l'université nous a fait parvenir une photocopie de qualité inférieure.

Les documents qui font déjà l'objet d'un droit d'auteur (articles de revue, examens publiés, etc.) ne sont pas microfilmés.

La reproduction, même partielle, de ce microfilm est soumise à la Loi canadienne sur le droit d'auteur, SRC 1970, c. C-30. Veuillez prendre connaissance des formules d'autorisation qui accompagnent cette thèse.

THIS DISSERTATION
HAS BEEN MICROFILMED
EXACTLY AS RECEIVED

LA THÈSE A ÉTÉ
MICROFILMÉE TELLE QUE
NOUS L'AVONS REÇUE

NL 339 (r. 86/01)

Canada

193

National Library of Canada
Bibliothèque nationale du Canada

0-315-23387-7

Canadian Theses Division
Division des thèses canadiennes

Ottawa, Canada
K1A 0N4

PERMISSION TO MICROFILM — AUTORISATION DE MICROFILMER

• Please print or type — Écrire en lettres moulées ou dactylographier

Full Name of Author — Nom complet de l'auteur

SIMON JOHN HOOK

Date of Birth — Date de naissance	Country of Birth — Lieu de naissance
15/06/1961	ENGLAND

Permanent Address — Résidence fixe

1. GREYSTONES DR.
SHEFFIELD. S11 7JQ ENGLAND

Title of Thesis — Titre de la thèse

Integrated Landsat - MSS and - TM and geophysical data applications in geological mapping and mineral exploration for W. Nfld.

University — Université

ALBERTA

Degree for which thesis was presented — Grade pour lequel cette thèse fut présentée

MSc

Year this degree conferred — Année d'obtention de ce grade	Name of Supervisor — Nom du directeur de thèse
1985	PROF R. D. MORTON

Permission is hereby granted to the NATIONAL LIBRARY OF CANADA to microfilm this thesis and to lend or sell copies of the film.

The author reserves other publication rights, and neither the thesis nor extensive extracts from it may be printed or otherwise reproduced without the author's written permission.

L'autorisation est, par la présente, accordée à la BIBLIOTHÈQUE NATIONALE DU CANADA de microfilmer cette thèse et de prêter ou de vendre des exemplaires du film.

L'auteur se réserve les autres droits de publication; ni la thèse ni de longs extraits de celle-ci ne doivent être imprimés ou autrement reproduits sans l'autorisation écrite de l'auteur.

Date	Signature
23rd July 1985	Simon J. Hook

NL-91 (4/77)

THE UNIVERSITY OF ALBERTA

Integrated Landsat-MSS and -TM and geophysical data applications in geological mapping and mineral exploration for W. Nfld.

by

Simon John Hook

©

A THESIS

SUBMITTED TO THE FACULTY OF GRADUATE STUDIES AND RESEARCH

IN PARTIAL FULFILMENT OF THE REQUIREMENTS FOR THE DEGREE

OF Master of Science

Geology

EDMONTON, ALBERTA

Fall, 1985

THE UNIVERSITY OF ALBERTA

RELEASE FORM

NAME OF AUTHOR Simon John Hook

TITLE OF THESIS Integrated Landsat-MSS and-TM and geophysical data applications in geological mapping and mineral exploration for W. Nfld.

DEGREE FOR WHICH THESIS WAS PRESENTED Master of Science

YEAR THIS DEGREE GRANTED Fall, 1985

Permission is hereby granted to THE UNIVERSITY OF ALBERTA LIBRARY to reproduce single copies of this thesis and to lend or sell such copies for private, scholarly or scientific research purposes only.

The author reserves other publication rights, and neither the thesis nor extensive extracts from it may be printed or otherwise reproduced without the author's written permission.

(SIGNED) ..... S. Hook .....

PERMANENT ADDRESS:

1 Greystones Dr.,
Sheffield, S11 7JQ
ENGLAND

DATED 23rd July 1985

THE UNIVERSITY OF ALBERTA

FACULTY OF GRADUATE STUDIES AND RESEARCH

The undersigned certify that they have read, and recommend to the Faculty of Graduate Studies and Research, for acceptance, a thesis entitled Integrated Landsat-MSS and-TM and geophysical data applications in geological mapping and mineral exploration for W. Nfld. submitted by Simon John Hook in partial fulfilment of the requirements for the degree of Master of Science.

.....
Supervisor

.....

.....

Date.....July 23, 1985.....

Dedication

To family and friends

Abstract

Landsat 4 Multispectral Scanner (MSS) and Thematic Mapper (TM) digital data were evaluated in conjunction with optical radar and aeromagnetic data as to their applications in geological mapping and in mineral exploration in Western Newfoundland. Research concentrated upon three areas, namely:

1. Lineament Analysis
2. Spectral Analysis
3. Integration of Aeromagnetic data

Lineament analysis, using a band 3 (700- to 800-nm) Landsat image and a hard-copy L band (25cm) radar image, established two points. Firstly, the lineament orientation pattern obtained from the major geological units increased in complexity with increasing age of the geological unit. Secondly, there was a strong correlation of increasing lineament density with increasing discovery of mineral occurrences.

Spectral analysis of laboratory-and field ratio-spectra from the geological units in the area suggested discrimination of limonite and serpentinite should be possible using digital Landsat MSS and TM data. Discrimination of these alteration products and also of several rock types, including the separation of dunite from pyroxene- bearing ultramafic rocks, was achieved using digital Landsat MSS and TM data.

Aeromagnetic data were interpreted using upward and downward continuation and fourier transforms and revealed three points. Firstly, there was a strong visual correlation of aeromagnetic lineaments with Landsat lineaments. Secondly, most of the major mineral occurrence clusters were located on or near aeromagnetic anomalies. Thirdly, most of the mineral occurrence clusters were located on or near aeromagnetic lineaments.

Finally, it was concluded Landsat MSS and TM digital data and aeromagnetic and radar data could provide a valuable tool for low-cost and rapid geological mapping and mineral exploration in a northern maritime environment.

Acknowledgements

Initially I would like to thank the numerous people who provided encouragement, assistance and friendship throughout the duration of this project.

Special thanks go to my supervisor Dr. R. D. Morton who suggested a remote sensing project and provided useful suggestions throughout its course. Dr. R. Slaney at Radarsat is thanked for suggesting Newfoundland as potential study area, and together with J. Harris also at Radarsat, for providing useful discussions on lineament analysis. Dr. H. A. K. Charlesworth, D. Proudfoot, and D. Wynne are thanked for access to some of the programs used in the lineament analysis.

P. Lawrence of Barringer-Magenta Ltd. is thanked for providing their portable hand held ratioing radiometer (HHRR) for fieldwork and laboratory spectra of field samples. James A. Hook is acknowledged for useful support in the field.

The Canadian Center of Remote Sensing (CCRS) is acknowledged for allowing me to obtain the TM data through the Canadian LIDQA experiment. The staff of the Alberta Remote Sensing Center are thanked for use of the image analysis facilities, especially F. MacCallum and G. Reichert who helped operate the ARIES II system. Dr. P. Crown also gave me access to the ARIES II system at the University of Alberta and provided numerous fruitful discussions. Special thanks go to Dr. J Samson who provided all the programs used for analysis of the aeromagnetic data and aided with the interpretation of the results.

Financial support for the project was provided by the Department of Energy, Mines and Resources and the University of Alberta Central Research Fund.

Finally, I am grateful for the friendship provided by the faculty, fellow graduates and undergraduates in the Department. The editing skills and friendship of M. Brearley are gratefully acknowledged and K. M. Ansdell is especially thanked for continuous encouragement, support and friendship.

Table of Contents

Chapter

Page

I. Introduction 1

II. Regional Geology 3

A. Geological Setting 3

B. Physiography and Glaciation 3

C. The Bay of Islands Study Area 4

D. The Hare Bay Study Area 12

III. Lineament Analysis 15

A. Introduction 15

B. Orientation Plots 16

Method 16

Landsat Data Interpretation 18

Radar Data Interpretation 26

C. Lineament Density Diagrams 34

Introduction 34

Method 34

Interpretation 40

D. Conclusions 50

IV. Spectral Analysis 51

Introduction 51

A. Laboratory Spectra 52

Introduction 52

Spectral Features 52

Spectral Data Collection and Analysis 54

Basement Granitic Rocks 54

Ultramafics and Serpentinites 54

The Gabbros 57

Sheeted Dykes 59

Pillow Basalts 60

B. General Features 61

C. Ground Truth Spectra 61
Introduction 61
Basement - MSS Ratio Data 62
Ultramafic - MSS Ratio Data 62
Gabbros - MSS Ratio Data 65
Sheeted Dykes - MSS Ratio Data 67
Pillow Basalts - MSS Ratio Data 69
Summary of MSS Ratio Data from Analyses of the Ophiolite and Basement. 69
Basement - TM Ratio Data 69
Ultramafics and Serpentinites - TM Ratio Data 72
Gabbros - TM Ratio Data 73
Sheeted Dykes - TM Ratio Data 73
Pillow Basalts - TM Ratio Data 74
Summary of TM Ratio Data from Analyses of Ophiolite and Basement ... 74
V. Image Analysis 76
A. Introduction 76
B. Image Analysis Techniques 77
Geometric Correction 77
Compositing and Contrast Stretching 77
Ratioing 78
Atmospheric Correction 78
Classification 79
C. MSS Data Interpretation 79
Regional Study 79
Detailed Interpretation of the Four Massifs of the Bay of Islands Assemblage 80
Classification 84
D. TM Data Interpretation 85
Band Ratio Imagery 86
E. Conclusions 88
VI. Geophysical Data Integration 93

A. Introduction 93
B. Methodology 93
C. Interpretation 94
D. Conclusions 106
VII. Conclusions and Future Recommendations 118
VIII. References 120
IX. APPENDIX I 127
Radiometer Design 128
Measurement Technique 128
X. APPENDIX II 130
A. Initial Data Costs 131

List of Tables

Table 1. Rock groups and structural slices within the Humber Arm and Hare Bay Allochthons, listed from structurally lowest (bottom) to structurally highest (top) in each Allochthon, after Williams, (1975).....8

Table 2. Multispectral Scanner (MSS) and Thematic Mapper (TM) Wavelength Ranges.....52

Table 3. Mean values ± one standard deviation for a set of pixels from various rock types in the MSS bands and several band ratios. 81

Table 4. Operator stretches applied to band ratio imagery. 83

Table 5. Mean reflectance values ± one standard deviation for a set of pixels from the dunites (light brown) and the pyroxene-bearing ultramafic rocks (dark brown) in the TM bands and selected band ratios.....86

Table 6. Sub areas chosen for detailed analysis of their aeromagnetic signatures. 94

List of Figures

Figure 1. Location of Study Areas in Western Newfoundland.....5

Figure 2. Major Geological Units of the Bay of Islands Study Area.....6

Figure 3. The Four Massifs of the Bay of Islands Slice Aseemblage.....9

Figure 3a. Geology of Table and North Arm Mounta in, after Williams, (1972) and Elthon *et al., (1984).* -Key also applies to Figures 3b and 3c.....10

Figure 3b. Geology of Blow Me Down Mountain, after Williams, (1973). (Key: see Figure 3a).....11

Figure 3c. Geology of the Lewis Hills, after Karson, (1984). (Key: see Figure 3a).....12

Figure 4. The Geology of the northern part of the Hare Bay Allochthon (after Smyth, 1973 and Williams, 1975).....13

Figure 5. Histogram Types, St. Georges Data.....17

Figure 6. Smoothed Rose Histogram - Precambrian Basement Data.....19

Figure 7. Smoothed Rose Histogram - Cambrian Clastics Metamorphosed Data.....20

Figure 8. Smoothed Rose Histogram - Cambrian Clastics Data.....21

Figure 9. Smoothed Rose Histogram - Transported Sediment Data.....22

Figure 10. Smoothed Rose Histogram - Ophiolite Data.....23

Figure 11. Smoothed Rose Histogram - Ordovician Carbonate Data.....24

Figure 12. Smoothed Rose Histogram - Deer Lake Data.....25

Figure 13. Smoothed Rose Histogram - Precambrian Basement Radar Data.....27

Figure 14. Smoothed Rose Histogram - Cambrian Clastics Metamorphosed Radar Data.....28

Figure 15. Smoothed Rose Histogram - Cambrian Clastics Radar Data.....29

Figure 16. Smoothed Rose Histogram - Transported Clastics Radar Data.....30

Figure 17. Smoothed Rose Histogram - Ophiolite Radar Data.....31

Figure 18. Smoothed Rose Histogram - Ordovician Carbonate Radar Data.....32

Figure 19. Smoothed Rose Histogram - Deer Lake Radar Data.....33

Figure 20. Distribution of Metalliferous Mineral Occurrences with respect to Lineament Density.....36

Figure 21. Distribution of Non-Metalliferous Mineral Occurrences with respect to Lineament Density.....37

Figure 22. Distribution of Lineament-Related Mineral Occurrences with respect to Lineament Density.....38

Figure 23. Distribution of Non Lineament-Related Mineral Occurrences with respect to Lineament Density.....39

Figure 24. Number of Metalliferous compared to Non Metalliferous Mineral Occurrences

discovered with distance from the nearest Landsat Lineament Density High. 42

Figure 25. Number of Lineament-Related compared to Non Lineament-Related mineral Occurrences discovered with distance from the nearest Landsat Lineament Density High. 43

Figure 26. Percentage of total Lineament-Related mineral occurrences discovered from the nearest lineament density high within the Ophiolte Suite, and its relation to the percentage of the total area of the Ophiolite Suite.....44

Figure 27. Distribution of Metalliferous Mineral Occurrences with respect to Fluvio-Structural Density.....46

Figure 28. Distribution of Non-Metalliferous Mineral Occurrences with respect to Fluvio-Structural Density.....47

Figure 29. Distribution of Lineament-Related Mineral Occurrences with respect to Fluvio-Structural Density.....48

Figure 30. Distribution of Non Lineament-Related Mineral Occurrences with respect to Fluvio-Structural Lineament Density.....49

Figure 31. Number of Metalliferous compared to Non-Metalliferous mineral occurrences discovered with distance from the nearest Fluvio-Structural density high.....50

Figure 32. Spectral Relectance Curves for Samples from the Basement 55

Figure 33. Spectral Reflectance Curves For Samples of Ultramafics and Serpentintes. 56

Figure 34. Spectral Reflectance Curves for Gabbros. 58

Figure 35. Spectral Reflectance Curves for the Sheeted Dykes. 59

Figure 36. Spectral Reflectance Curves for the Samples of Pillow Basalts. 60

Figure 37. MSS and TM Band Ratio Field Data for the Basement. 63

Figure 38.', ' MSS and TM Band Ratio Field Data for the Ultramafics and Serpentinites. 64

Figure 39. MSS and TM Band Ratio Field Data from the Gabbros. 66

Figure 40. MSS and TM Field Ratio Data from the Sheeted Dykes. 68

Figure 41. MSS and TM Ratio Field Data from the Pillow Basalts.....70

Figure 42. Mean and Mean Values ± 1 standard deviation for the MSS Field Ratio Data. ...71

Figure 43. Mean and Mean Value ± 1 standard deviation for the TM Field Ratio Data.....75

Figure 44. Lewis Hills detrended aeromagnetic data and interpreted lineaments. 95

Figure 45. Lewis Hills Landsat lineament map. 96

Figure 46. Waveform and Fast Fourier Amplitude Plot for a 2 N-S trending lineaments. 97

Figure 47. Fourier Amplitude plot of the Lewis Hills detrended aeromagnetic data 98

Figure 48. Lewis Hills detrended aeromagnetic data continued up 1.5 grid units and interpreted lineaments. 99

Figure 49. Fourier amplitude plot of the Lewis H ills detrended aeromagnetic data continued up 1.5 grid units..... 100

Figure 50. Lewis Hills detrended aeromagnetic data continued down 1.5 grid units and interpreted lineaments..... 101

Figure 51. Fourier amplitude plot of the Lewis Hills detrended aeromagnetic data continued down 1.5 grid units. 102

Figure 52. Blow Me Down Mountain detrended aeromagnetic data and interpreted lineaments. 103

Figure 53. Blow Me Down Mountain Landsat lineament map..... 104

Figure 54. Fourier amplitude plot for the Blow Me Down Mountain detrended aeromagnetic data..... 105

Figure 55. Blow Me Down Mountain detrended aeromagnetic data continued up 1.5 grid units and interpreted lineaments. 107

Figure 56. Fourier amplitude plot of the Blow Me Down Mountain detrended aeromagnetic data continued up 1.5 grid units. 108

Figure 57. Blow Me Down Mountain detrended aeromagnetic data continued down 1.0 grid units and interpreted lineaments. 109

Figure 58. Fourier amplitude plot of the Blow Me Down Mountain detrended aeromagnetic data continued down 1.0 grid units..... 110

Figure 59. Table Mountain and North Arm Mountain detrended aeromagnetic data and interpreted lineaments..... 111

Figure 60. Table Mountain and North Arm Mountain Landsat lineament map..... 112

Figure 61. Fourier amplitude plot of the Table Mountain and North Arm Mountain detrended aeromagnetic data..... 113

Figure 62. North Arm Mountain and Table Mountain detrended aeromagnetic data continued up 1.5 grid units and interpreted lineaments..... 114

Figure 63. Fourier amplitude plot of Table Mountain and North Arm Mountain detrended aeromagnetic data continued up 1.5 grid units. 115

Figure 64. Table Mountain and North Arm Mountain detrended aeromagnetic data continued down 1.0 grid units and interpreted lineaments. 116

Figure 65. Fourier amplitude plot of the Table Mountain and North Arm Mo[illegible]n detrended aeromagnetic data continued down 1.0 grid units..... 117

List of Plates

Plate 1. Colour Infrared Composite of the Bay of Islands Study Area. 4-B, 5-G, 7-R.....89

Plate 2. Band Ratio Composite of North Arm Mtn. 4/5-B, 5/6-G, 6/7-R.....90

Plate 3. Atmospherically Corrected Band Ratio Composite of North Arm Mtn. 4/5-B, 5/6-G, 6/7-R.....90

Plate 4. Atmospherically Corrected Band Ratio Composite of Blow Me Down Mtn. 4/5-B, 5/6-G, 6/7-R.....90

Plate 5. Atmospherically Corrected Band Ratio Composite of the Lewis Hills. 4/5-B, 5/6-G, 6/7-R.....91

Plate 6. 4/5 Band Ratio Image of Table Mountain. 91

Plate 7. Supervised Classification of Limonite and Snow on North Arm Mtn.....91

Plate 8. Supervised Classification of Limonite and Snow on Blow Me Down Mtn. 92

Plate 9. Supervised Classification of Limonite and Snow on the Lewis Hills. 92

Plate 10. TM Colour Composite of the Hare Bay Area. 1-B, 2-G, 3-R.....92

I. Introduction

The objective of this study was evaluate the use of Landsat Multispectral Scanner (MSS) and Thematic Mapper (TM) data integrated with radar and aeromagnetic data for lithological mapping and mineral exploration in Western Newfoundland.

Western Newfoundland, was selected as the study area for several reasons:

1. A large variety of lithologies and proven mineral potential.
2. Availability of digital Landsat MSS and TM data, hard-copy Radar data and digital aeromagnetic data.
3. A large variation in exposure from maximum rock exposure and minimum vegetation cover to minimum rock exposure and maximum vegetation cover.

The research proceedure adopted concentrated in four areas each of which form a part of the thesis. These are:

1. Lineament Analysis
2. Spectral Analysis
3. Image Analysis
4. Integration of aeromagnetic data.

Lineament analysis involved the establishment of a rapid computerised technique for analysis of lineaments in terms of their orientation and density. The lineament orientation data were used to determine if there was a relationship between the complexity of the lineament orientation pattern and the age of the geological unit from which it was obtained. Lineament density data were used to determine if a spatial relationship existed between mineral occurrence distribution and lineament density.

Spectral analysis involved the collection of full spectra and field ratio spectra in the MSS and TM wavelength ranges from various geological units in the study area. Special emphasis was placed on obtaining a complete set of spectral data from the Bay of Islands ophiolite suite which lent itself to remote identification due to its sparse vegetation cover. These data were used to determine the the most suitable wavelength ranges for lithological mapping and the discrimination of alteration products (limonite and serpentinite) using digital Landsat MSS and TM data.

Image analysis was concerned with the development of techniques for the extraction of reflectance data for lithological and alteration mapping with Landsat MSS and TM data. These

techniques were refined and improved using data obtained in the spectral analysis.

Finally, aeromagnetic data were processed using upward and downward continuation and Fourier transforms to map aeromagnetic lineaments. These lineaments were compared lineaments interpreted from Landsat 4, band 3 (700- to 800-nm) hard-copy data to determine if they were inter-related. The aeromagnetic lineaments and anomalies were compared with the spatial distribution of the mineral occurrences to establish if they were related.

II. Regional Geology

A. Geological Setting

Western Newfoundland consists of four major tectonic elements, namely :

1. A crystalline Precambrian basement.
2. An autochthonous Cambrian-Ordovician sequence which unconformably overlies the Precambrian basement
3. Two major allocthonous sequences termed the Hare Bay Allocthon and Humber Arm Allochthon in the north and south respectively. These were emplaced during Middle Ordovician times and are composed of a series of structural slices. The lower structural slices consist mainly of Cambrian to Lower Ordovician clastic sedimentary rocks, whereas the higher structural slices comprise igneous and metamorphic rocks. The highest part of each tectonic slice represents part of an ophiolite suite with an associated metamorphic aureole. Each slice is separated from its neighbours and from the underlying autochthon by thin zones of black shale melange.
4. An unconformable, autochthonous Carboniferous cover.

B. Physiography and Glaciation

The topography of Western Newfoundland is dominated by the contrasting major tectonic components. The Precambrian basement forms the backbone of the Great Northern Peninsula, represented by the Long Range Mountains in the north and by the Red Indian Range in the south. It is characterised by a mainly hilly topography with elevations exceeding 610m. The forest cover is sparse and low and rock outcrop is frequent, within the major valleys (Wells *et al.*, 1972).

The autochthonous Cambro-Ordovician sequence forms the coastal lowlands, which are characterised by a rolling topography which is quite hilly in places. The rolling ground tends to be underlain by till deposits in the form of hummocky moraine, and the hilly areas have ground moraine and colluvial deposits. The forest cover is high and dominated by balsam fir (Wells *et al.*, 1972).

The allochthonous terrane produces two types of topography, due to the different nature of the structurally lower and upper parts. The lower sedimentary parts of the allochthon

composed of carbonate, sandstone and shale, form a rolling, largely tree-covered topography. The higher igneous and metamorphic parts of the allochthon vary in vegetation cover with bedrock mineralogy. The ultramafic terranes are essentially devoid of vegetation, and have a strong iron oxide stain from the weathering of olivine and pyroxene. They give rise to a barren terrane with an orange brown hue. Vegetation increases on the overlying gabbros and sheeted dyke complexes to a sparse shrub cover with frequent peat bogs in the hollows. The overlying pillow basalts and sedimentary rocks are largely tree-covered. The glacial till on the upper igneous and metamorphic parts is thin and patchy with frequent large glacial erratics exposed.

The present study was undertaken in two areas, here termed the Bay of Islands area and the Hare Bay area. The location of these areas within Western Newfoundland is given in Figure 1.

C. The Bay of Islands Study Area

The Bay of Islands study area encompasses parts of NTS 1:250,000 maps 12A, 12B, 12G and 12H whose equivalent geological maps are: Red Indian Lake (W. Half) Map 8-1957, Stephenville Map 117A, Bay of Islands Map 1355A and Sandy Lake (W. Half) Map 47-1959 respectively. The geology of the Bay of Islands study areas has been summarised in Figure 2.

These can be further grouped into three major units, namely a Precambrian basement, an autochthonous Palaeozoic cover and an allochthonous Cambrian - Ordovician terrane, termed the Humber Arm Allochthon. The autochthonous Palaeozoic cover consists of the Cambrian clastics (metamorphosed and unmetamorphosed), the Ordovician carbonates, and the overlying Carboniferous cover (Deer Lake and St. Georges) (Figure 2). The allochthonous cover includes the ophiolites and the transported clastics (Figure 2).

Precambrian basement occurs in the northern and southern portions of the study area as part of the Long Range Mountains in the north and Red Indian Range in the south (Figure 2). The basement comprises a high-grade, granite-gneiss complex considered to represent an inlier of the Grenville province in the miogeoclinal belt of the Appalachian Orogen (Erdmer, 1984). The northern basement consists of felsic banded gneisses (Baird, 1958), which are cut by numerous diabase dykes of the Long Range Swarm. These dykes vary in width from 1 to 40m (Erdmer, 1984). Metamorphic grade ranges from the granulite facies in the west to the amphibolite facies in the east. The basement in the south consists of foliated granitic and basic

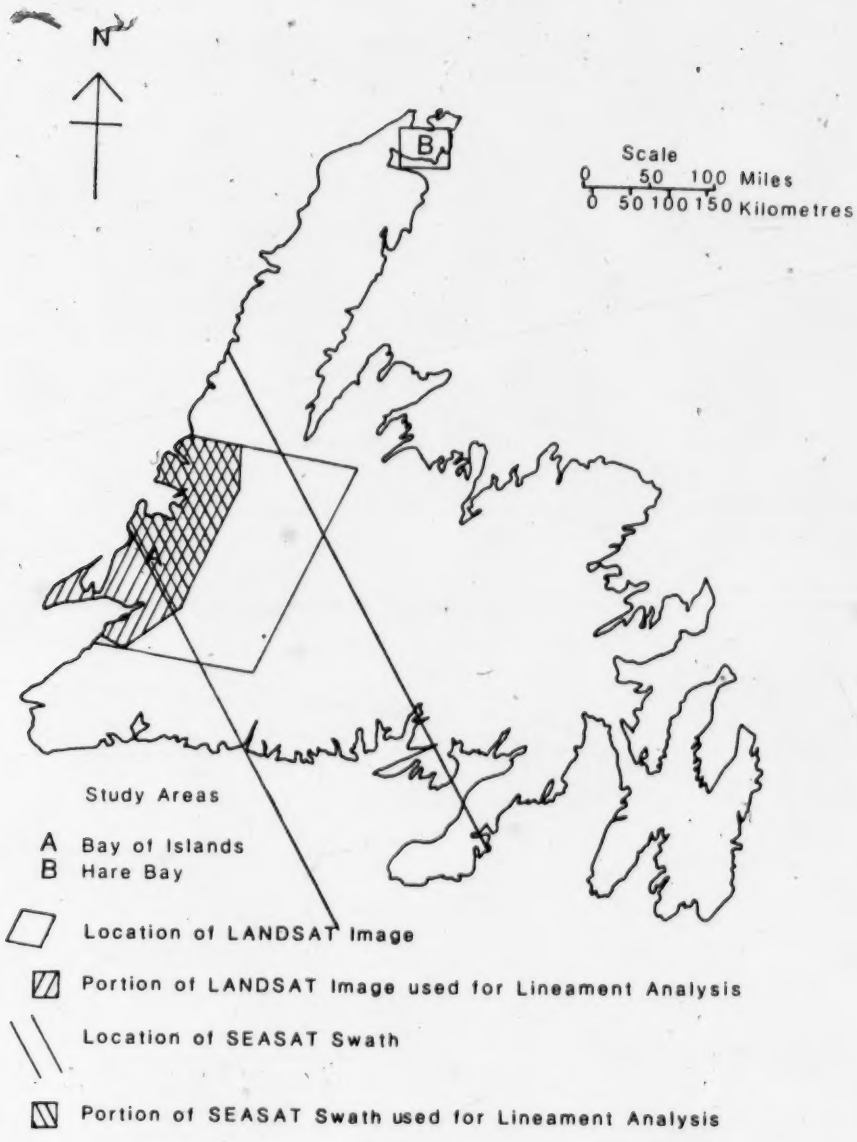

Figure 1. Location of Study Areas in Western Newfoundland.

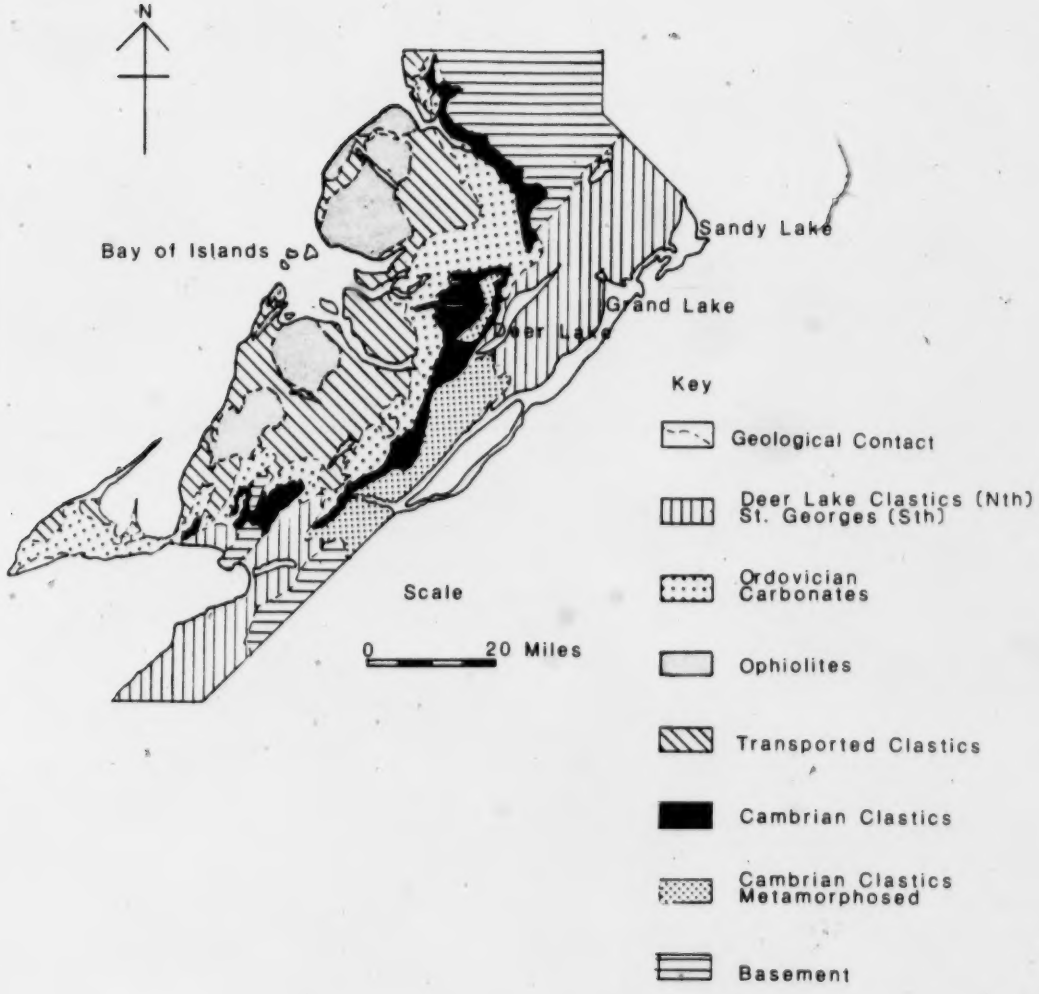

Figure 2. Major Geological Units of the Bay of Islands Study Area.

rocks metamorphosed in the amphibolite facies (Riley, 1953).

The autochthonous terrane may be separated into rocks of Cambrian-Ordovician age that have been affected by an Early to Mid Palaeozoic deformation, and a subhorizontal cover of Carboniferous rocks (Williams *et al.*, 1981). The Cambrian-Ordovician rocks consist of platformal carbonates (limestone breccia, limestone and dolomite) which grade upward into sandstone and shale. These are referred to as the Cambrian clastics, metamorphosed Cambrian clastics and the Ordovician Carbonates (Figure 2).

The overlying Carboniferous rocks consist of conglomerates, sandstones, limestone, siltstone, shale and gypsum. These are subhorizontal and undeformed west of Deer Lake and overturned and deformed east of Deer Lake (Williams *et al.*,1981). These are referred to as the Deer Lake rocks in the north and the St. George's rocks in the south (Figure 2).

The allochthonous Cambrian-Ordovician cover, named the Humber Arm Allochthon, is made up of a variety of sedimentary, volcanic and plutonic rocks which originated in the east. The sedimentary rocks and igneous rocks are referred to as the 'transported clastics' and 'ophiolites' respectively (Figure 2). These can be further subdivided into five, contrasting rock assemblages (Table 1)(Williams, 1973). Each of the five rock assemblages is made up of one or more structural slices (Williams, 1975). Where two or more slices are superposed or occur side by side, the slices are referred to as a "slice assemblage" (Table 1). Each slice and each slice assemblage occurs in a consistent position with respect to the overlying and underlying slices and slice assemblages (Table 1). For example, if the Bay of Islands and Humber Arm Supergroup slice assemblages were present in the same area, the Bay of Islands slice assemblage would always be structurally above the Humber Arm slice assemblage. Furthermore, the structural slices within each assemblage would always occur in a specific stacking order (Williams, 1975). The present study was chiefly concerned with the Bay of Islands Complex in the Humber Arm Allochthon. The Bay of Islands Complex is composed of four separate massifs which form the Bay of Islands slice assemblage. These are from north to south: Table Mountain, North Arm Mountain, Blow Me Down Mountain and Lewis Hills (Figure 3). The geology of these massifs is given in Figures 3a, 3b and 3c. The two northernmost massifs are separated by strike-slip faults. The rock units of the three northernmost massifs form synclines with north-east trending axes. The base of each massif is subhorizontal, resulting from structural truncation (Williams, 1975). The Bay of Islands Complex includes a complete

Table 1. Rock groups and structural slices within the Humber Arm and Hare Bay Allochthons, listed from structurally lowest (bottom) to structurally highest (top) in each Allochthon, after Williams, (1975).

Rock Group, Formation, or Complex	Slice or slice assemblage	Lithic description
	Humber Arm Allochthon	
Bay of Islands Complex	Bay of Islands slice assemblage	Ophiolite suite with basal metamorphic aureole
Little Port Complex	Little Port slice assemblage	Amphibolitic gabbro, massive to foliated sodic granite, mafic dikes and flows
Old Man Cove Formation	Old Man Cove slice	Polydeformed greenschists
Skinner Cove Formation	Skinner Cove slice assemblage	Alkali basalt, agglomerate, siltstone and minor limestone
Humber Arm Supergroup	Humber Arm slice assemblage	Shale, graywacke, limestone breccias
	Hare Bay Allochthon	
St. Anthony Group	St. Anthony slice	Harzburgite and underlying aureole
Cape Onion Formation	Cape Onion slice	Mafic pillow lava, black shale
Milan Arm Mélange	Milan Arm slice	Graywacke, plutonic and volcanic ophiolite-suite blocks in black shale
Grandois Group	Grandois slice	Polymictic conglomerate, sandy limestone
Maiden Point Formation	Maiden Point slice assemblage	Graywacke, quartz-pebble conglomerate, mafic pyroclastic rocks and pillow lava
Northwest Arm Formation	Northwest Arm slice	Black and green shale, buff siltstone, limestone, and limestone breccia

ophiolite suite from ultramafic rocks, through gabbros and sheeted dykes to mafic pillow lavas. The complex has a metamorphic aureole at its base and sediments at its top. The ultramafic rocks consist mainly of peridotites and dunites that have been strongly serpentinized in places. These pass upwards into layered gabbros which give way to more massive gabbros. The massive gabbros grade into sheeted dykes and dyke breccias through a broad transition zone. The sheeted dykes and dyke breccias are overlain by mafic pillow basalts.

The Bay of Islands ophiolite suite has been interpreted by most recent workers as former oceanic crust and upper mantle. Williams and Smyth (1973), have interpreted the metamorphic aureole at its base as a dynamothermal effect produced by obduction and transport of hot mantle. The aureole rocks are amphibolites and greenschists. The whole sequence is overlain with marked angular unconformity by sediments consisting of sandstone, shale and conglomerate (Casey and Kidd, 1981).

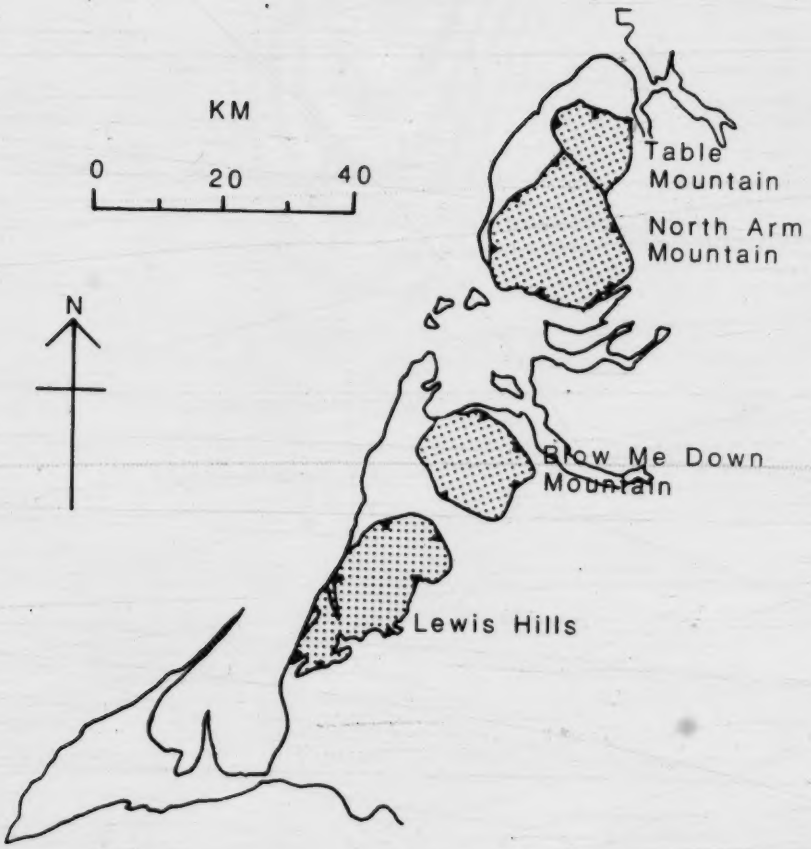

Figure 3. The Four Massifs of the Bay of Islands Slice Aseemblage.

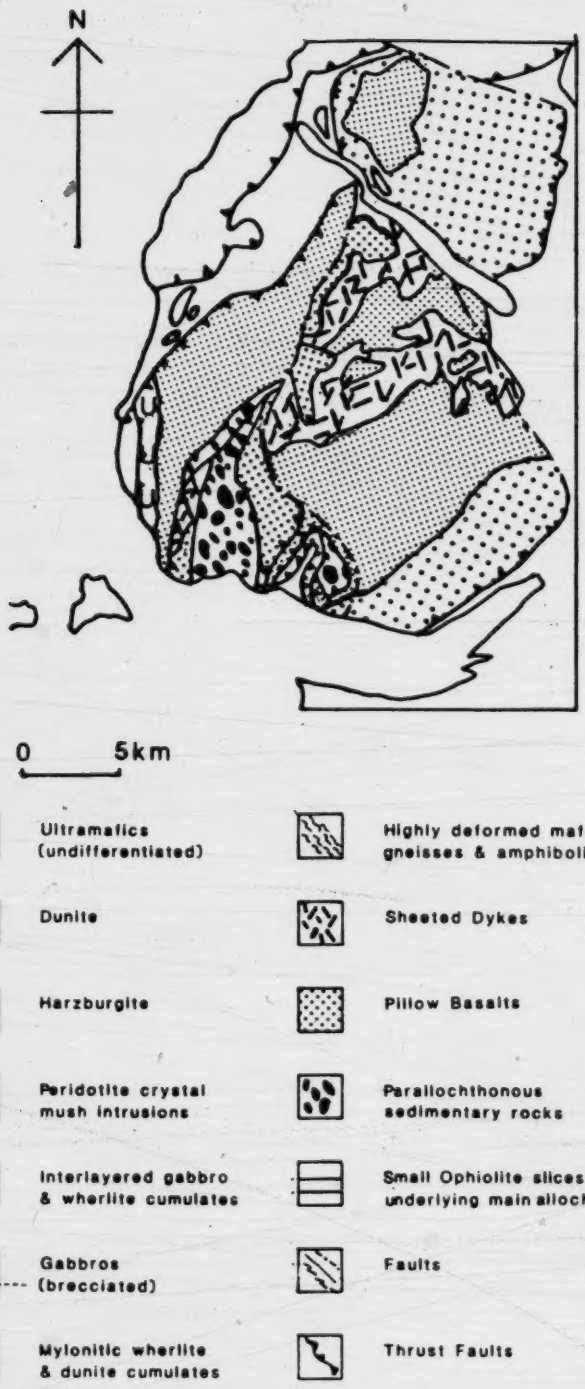

Figure 3a. Geology of Table and North Arm Mountain, after Williams, (1972) and Elthon *et al.*, (1984). - Key also applies to Figures 3b and 3c.

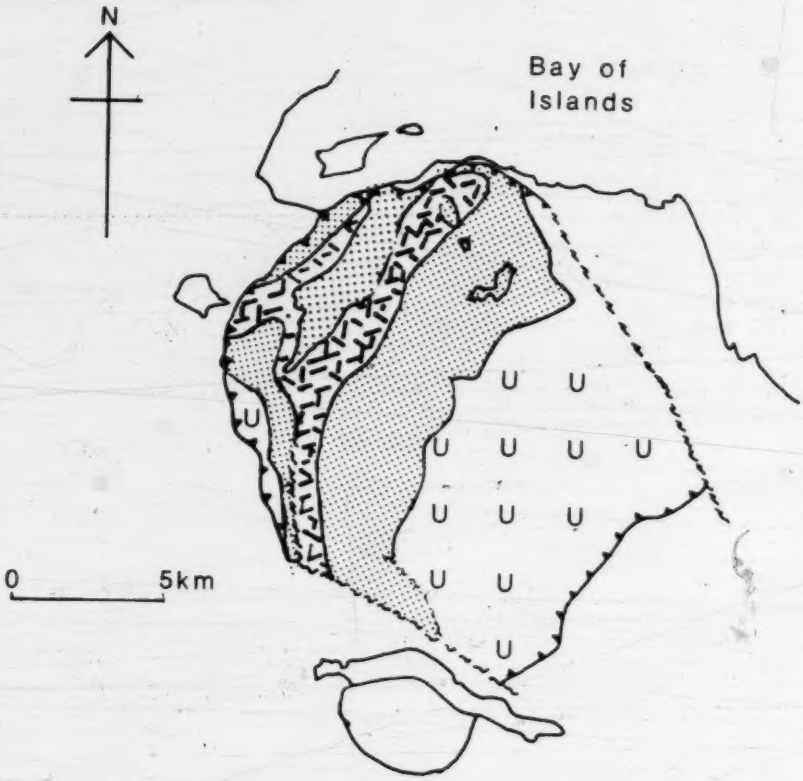

Figure 3b. Geology of Blow Me Down Mountain, after Williams, (1973). (Key: see Figure 3a).

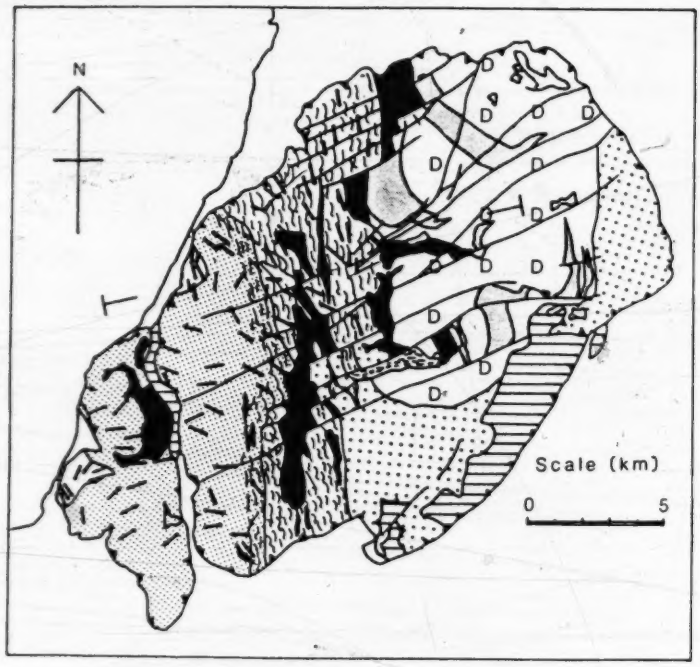

Figure 3c. Geology of the Lewis Hills, after Karson, (1984).
(Key: see Figure 3a).

D. The Hare Bay Study Area

The Hare Bay study area is located on the northeast corner of the Great Northern Peninsula, on NTS 1:250,000 sheets 12P and 2M. The equivalent geological map is the Strait of Belle Isle Area Map 1495A sheet 2. The study area is contained within the rocks of the St. Anthony Complex. Williams and Smyth (1983), consider the St. Anthony Complex to be the highest structural rock group of the six contrasting rock groups which comprise the Hare Bay Allochthon (see Table 1). The St. Anthony Complex is a polygenetic assemblage of ultramafic and metavolcanic rocks (Figure 4). Williams and Smyth (1983), divided the metavolcanic rocks into three formations based upon structural style and metamorphic grade. These were the Ireland Point Volcanics, the Goose Cove Schist and the Green Ridge Amphibolite. The Ireland Point Volcanics are structurally the lowest formation and consist of cleaved and flattened agglomerates and pillow lavas. These grade upward into the polydeformed Goose Cove Schist,

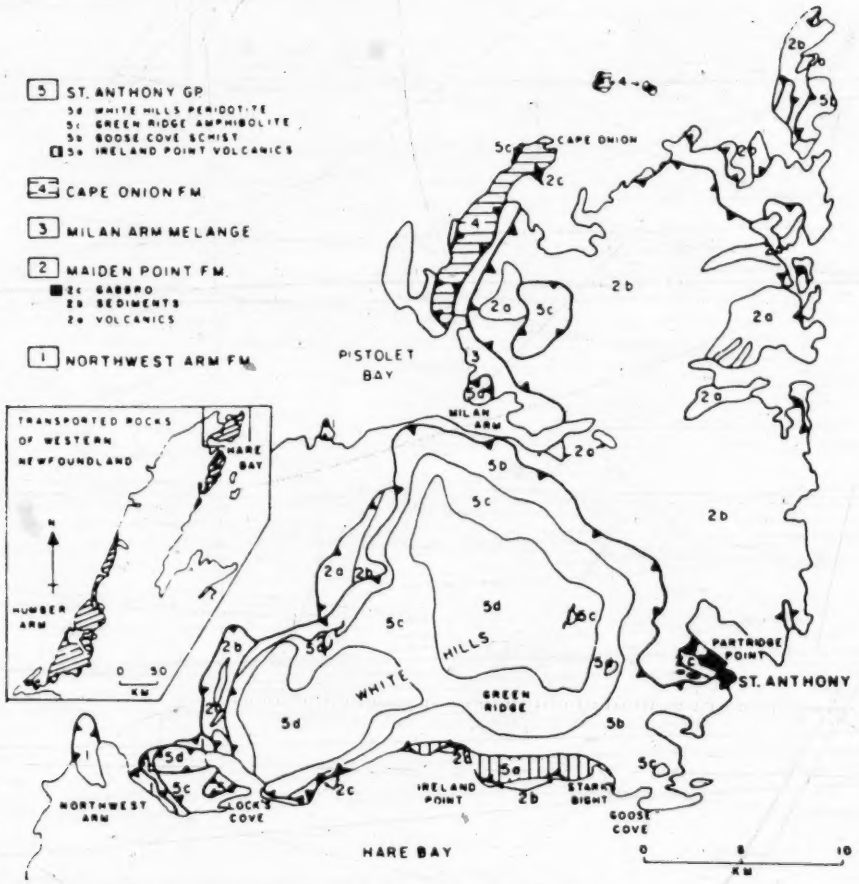

Figure 4. The Geology of the northern part of the Hare Bay Allochthon (after Smyth, 1973 and Williams, 1975).

which passes into the Green Ridge Amphibolite. These formations form a metamorphic aureole beneath the overlying ultramafic rocks, previously referred to as the White Hills Peridotite (Cooper, 1937). The present structural base of the St. Anthony Complex crosscuts the aureole rocks indicating the latter bear no genetic relationship to the original aureole base (Williams and Smyth, 1983). The ultramafic rocks consist of harzburgite and dunite with minor pyroxenite and are devoid of vegetation. The harzburgites have a rough surface, due to flattened resistent orthopyroxene crystals weathering in high relief above the surrounding partially serpentinized olivine. The dunites are finer grained and weather brownish yellow (Williams and Smyth, 1983).

The ultramafic rocks of the White Hills Peridotite form two tabular erosional remnants of a once complete slice and correspond to the eastern and western portions of the White Hills

(Williams and Smyth, 1983). Two smaller bodies occur west of Howe Harbour, (see Figure 3), and are interpreted by Williams and Smyth (1983), to be a continuation and the White Hills ultramafic rocks and their associated aureole.

III. Lineament Analysis

A. Introduction

The aim of this part of the study was to establish a rapid technique for classifying, on the basis of orientation and density, large quantities of lineament [1] data, obtained from different remote sensor sources in hard-copy form. Two sources were used, firstly a Band 3 (700-800-nm) Landsat 4, geometrically uncorrected image, acquired on the 11th October 1982, produced at a scale of 1:250,000. Secondly an L band (25cm) Seasat image acquired on September 22nd 1978, produced at a scale of 1:500,000. The Landsat image had less than 10% cloud cover, however, it did show a light dusting of snow on the high ground. The location of the images in Newfoundland and the portions used in this study are given in Figure 1. The Landsat image had a sun elevation angle of 30° from the east. The Seasat image had a "look"[2] direction to the N-E with a depression angle of 67° to 73°. The lineaments were classified according to the major host geological units (see Figure 2). The end points of each lineament were digiized. If a lineament was curved, it was separated into constituent straight line segments, each of which were then considered as individual lineaments. As the Landsat image was geometrically uncorrected, all the lineaments were rotated to the northwest. This rotation was removed by initially digitizing a line of known length which represents true north. The orientation of any vectors plotted thereafter is obtained with respect to this initial line. The length of this line was entered by the operator and if the entered length was different from the lines true length, any vectors entered thereafter were scaled accordingly. A map of the lineaments entered can be produced by the operator, if required. Orientation data from lineaments may be displayed as the number of lineaments per azimuth interval or as the total length of lineaments per azimuth interval (Siegal and Short, 1977). During this study orientation data were plotted in terms of total length, which minimizes errors resulting from segmentation of curvilinears during digitization. Total lineament length was determined by setting a minimum length, in this case of 2.5km. The minimum length was divided into each lineament to obtain a weighting factor. The weighting factor governed the number of times that

---

[1] A Lineament is defined as a mappable, simple or composite linear feature of a surface, whose parts are aligned in a rectilinear or curvilinear relationship which differs distinctly from the patterns of adjacent features and presumably reflects a subsurface phenomenon (O'Leary, 1976).

[2] The "look direction refers to the direction of transmission of the radar pulse, and is at a right angles to the orbit vector of Seasat.

a lineament orientation was entered into a master file. For example, using a minimum length of 2.5km a weighting factor of 4 would be obtained for a lineament 10km long. This lineament orientation would therefore be entered 4 times into the master file. The lineaments used were in three forms: raw data, weighted data (including lengths less than 2.5km) and weighted data (excluding lengths less than 2.5km).

B. Orientation Plots

Method

The digitized data were plotted on three types of histogram. A rose histogram, a moving average histogram and a smoothed histogram (Figure 5). The counting interval on the rose and moving average histograms was 5°.

To produce a smoothed histogram, a smoothing factor (K value) had to be obtained. This is a statistical value which accounts for operator variation in lineament measuring. The K value is derived by re-measuring a set of lineaments of various orientations and lengths. 43 lineaments were re-measured 10 times and to determine two K values. The lower K value (1154) included values less than 2.5km. The higher K value (1523) excluded values less than 2.5km. K values range from zero to infinity, the higher the K value, the less smoothing is done. Therefore smoothed plots produced using the higher K value show more of a resemblance to the rose histogram than plots using the lower K value. A lower K value indicates a lower precision, thus it was more difficult to re-measure lineaments less than 2.5km. Weighted data excluding values less than 2.5km were used for the interpretation.

Eigenvectors and eigenvalues were simultaneously determined for each data set (see Figure 5). These are statistical values which quantify the fit of the data about the major lineament directions. The maximum and minimum eigenvectors represent the major and minor lineament directions respectively. The higher the maximum eigenvalue, the better the fit of the data about the major lineament direction (maximum eigenvector). These relationships of eigenvectors and their accompanying eigenvalues to lineament directions are dependent on the data being unimodally distributed. Mark (1973), points out that for bimodally or multimodally distributed data the eigenvalue approach will produce an eigenvector which lies midway between the two major axes (lineament directions). Therefore the eigen approach should not be used

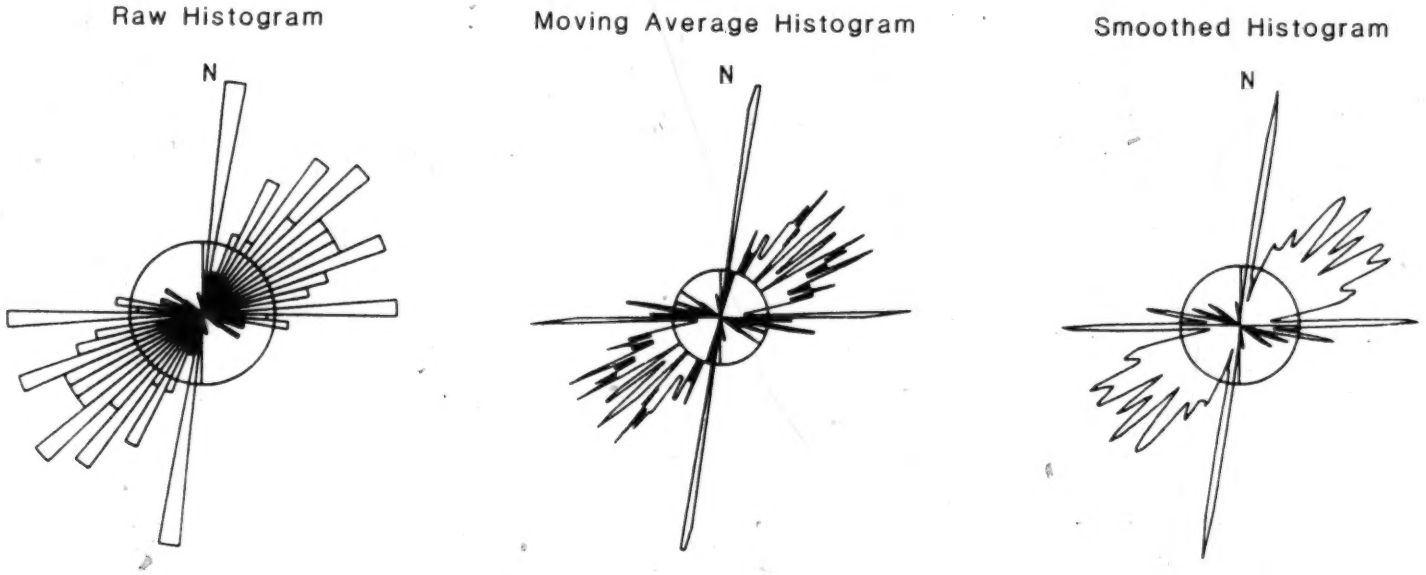

ST. GEORGES WEIGHTED EXCLUDING VALUES LESS THAN

2.5km K=1523 N=121

TREND	PLUNGE	EIGENVALUE/N
53.9	0.0	0.7887
143.9	0.0	0.2113
0.0	90.0	0.0

Figure 5. Histogram Types, St. Georges Data.

quantitatively where the data are not unimodal (Mark, 1973)

It is important to note the low sun elevation angle and easterly location of the sun will preferentially enhance N-S trending features; whereas for the Seasat data the low angle "look" direction from the SW will preferentially enhance NW-SE trending features. Therefore, little attempt has been made to quantitatively compare the two sets of data. Finally Siegal and Short (1977), show that operator variation in the recognition of and determination of the length and orientation of lineaments is significant. Thus extreme care should be taken when comparing these data to data obtained by other operators.

Landsat Data Interpretation

The best results were obtained using weighted data, excluding lengths less than 2.5km, plotted on smoothed histograms and these are presented here.

All the generated histograms are characterised by a broad NE trend (Figures 6 to 12), except for the data from the ophiolite terranes (Figure 10). The NE trend is recognised as a fold and fault trend in these units by (Bostock, 1983; Kennedy, 1979; Nyman *et al.*, 1982; Schilleref and Williams, 1978 and Williams and Gillespie, 1981). Certain histograms also have a minor W to NW trend which Kennedy (1982), observed as a fault trend in those units (Figures 6, 7 and 9). Bostock (1983), also observed the W to NW fault trend in the basement (Figure 6). Therefore the orientation data from all the geological units except the ophiolites can be explained by published structural data.

In a more general sense, the orientation plots increase noticeably in complexity with age. This is especially obvious when comparing the histogram for oldest rocks (Figure 6) with that for the youngest rocks (Figure 12). The increase is complexity is primarily related to the geological history of the unit, and secondly, to the rheology of the unit. Older geological units produce more complex lineament patterns for they have been subject to more deformational episodes. Unfortunately, the relationship between age and complexity does not hold true throughout the succession. This latter case is especially evident in the ophiolite suites, which have the most complex pattern (Figure 10). These data may be spurious for the following reasons. Firstly, very few lineaments have been measured (N = 105). Thus, if each counting division contains a few lineaments, there would be insufficient data to produce an impression of the overall trend. Secondly, the ophiolite suites, unlike any of the other geological units, are

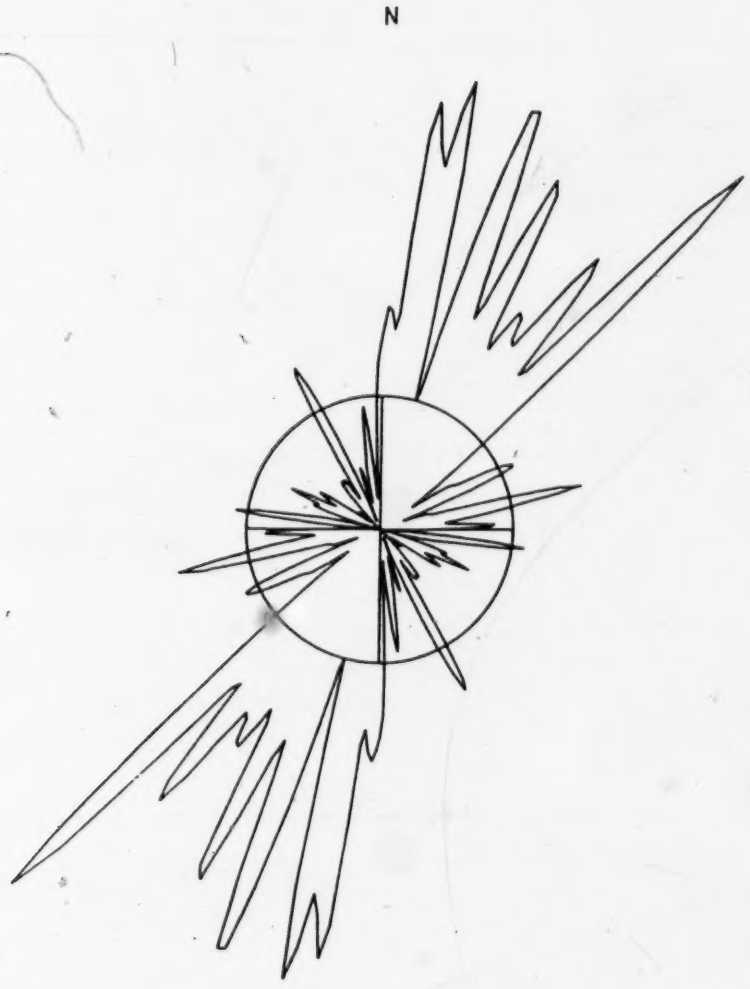

BASEMENT WEGHTED EXCLUDING VALUES LESS THAN

2.5km. K=1523 N=281

TREND	PLUNGE	EIGENVALUE/N
27.7	0.0	0.7309
117.7	0.0	0.2691
0.0	90.0	0.0

Figure 6. Smoothed Rose Histogram - Precambrian Basement Data.

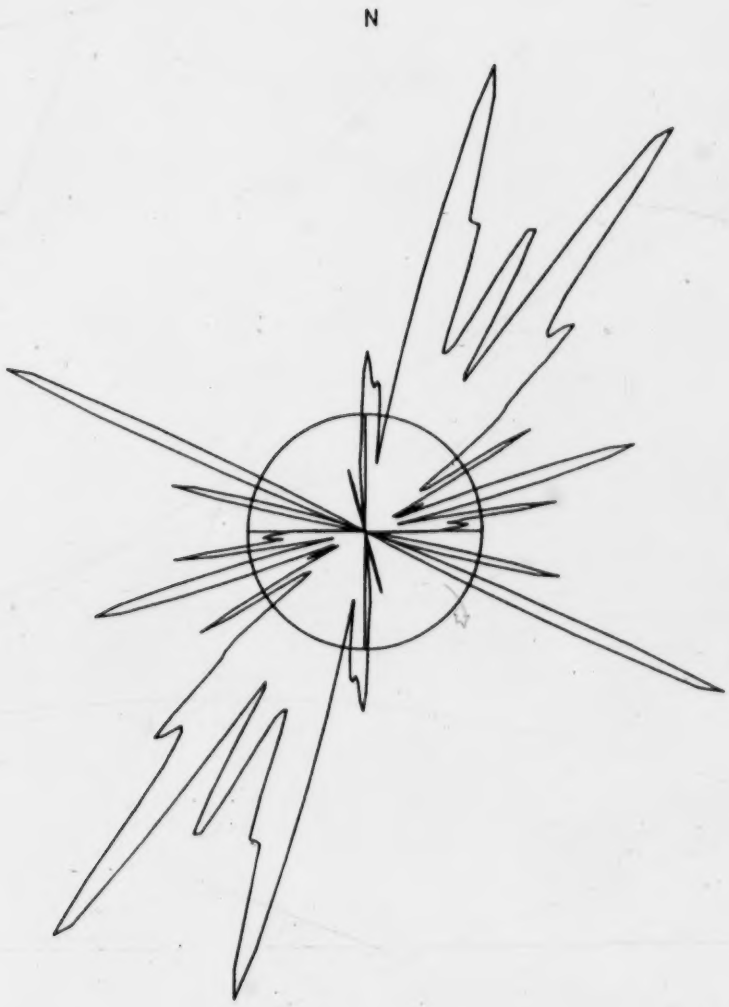

CAMBRIAN CLASTICS METAMORPHOSED WEIGHTED

EXCLUDING VALUES LESS THAN 2.5km K=1523 N=90

TREND	PLUNGE	EIGENVALUE/N
38.8	0.0	0.7506
128.8	0.0	0.2494
0.0	90.0	0.0

Figure 7. Smoothed Rose Histogram - Cambrian Clastics Metamorphosed Data.

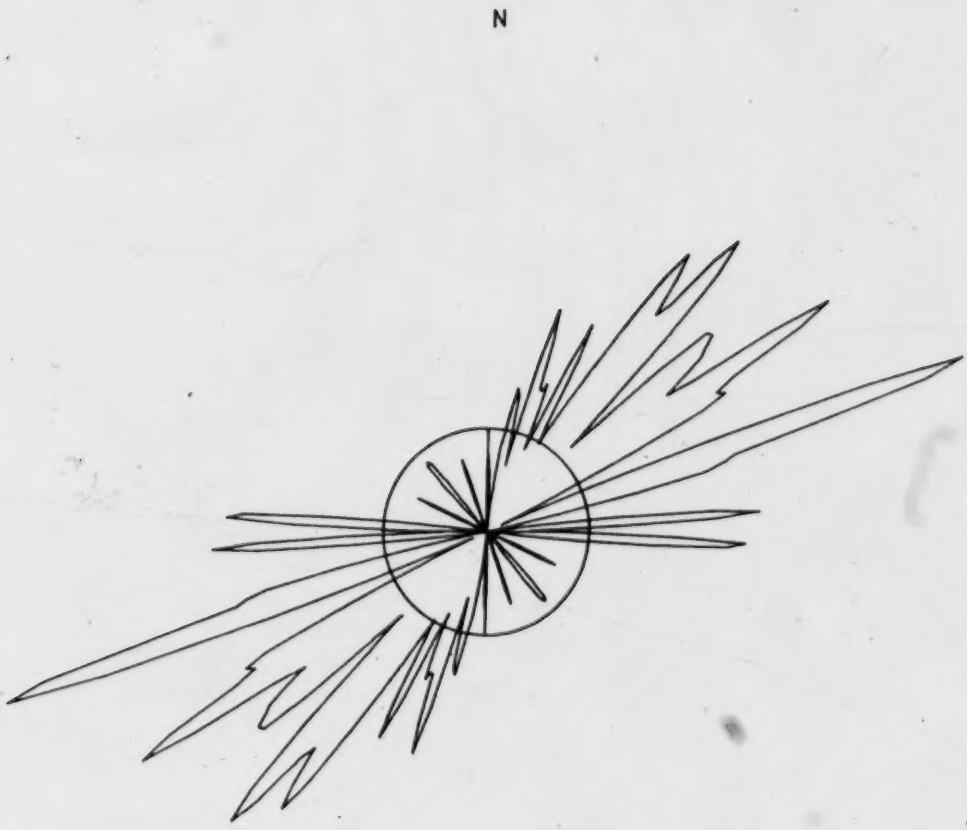

CAMBRIAN CLASTICS WEIGHTED EXCLUDING VALUES

LESS THAN 2.5km K=1523 N=66

TREND	PLUNGE	EIGENVALUE/N
51.2	0.0	0.8064
141.2	0.0	0.1936
0.0	90.0	0.0

Figure 8. Smoothed Rose Histogram - Cambrian Clastics Data.

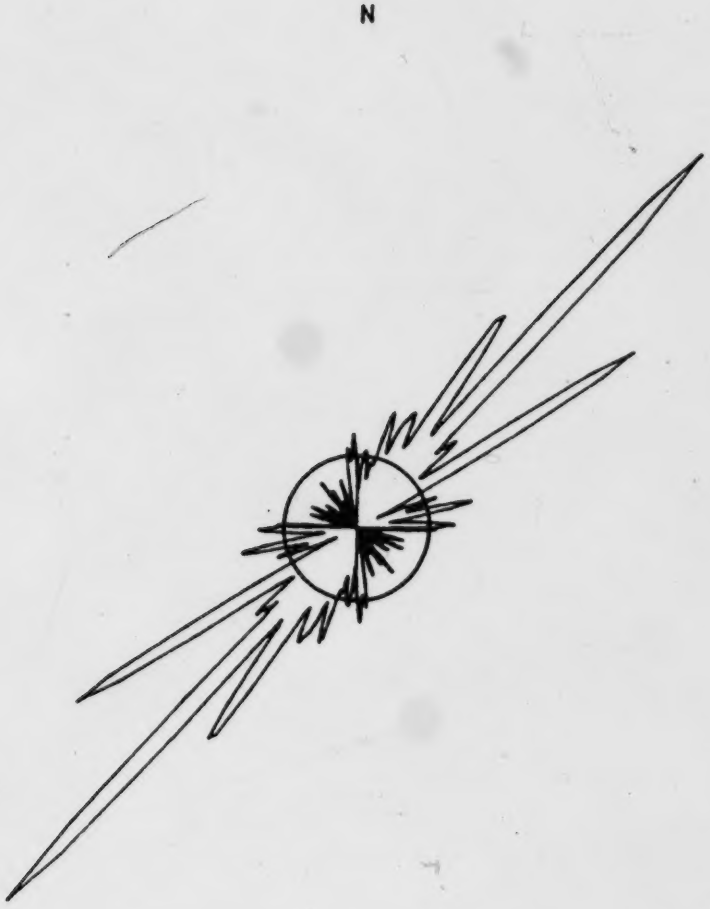

TRANSPORTED CLASTICS WEIGHTED EXCLUDING VALUES

LESS THAN 2.5km K=1523 N=224

TREND	PLUNGE	EIGENVALUE/N
42.4	0.0	0.7560
132.4	0.0	0.2440
0.0	90.0	0.0

Figure 9. Smoothed Rose Histogram - Transported Sediment Data.

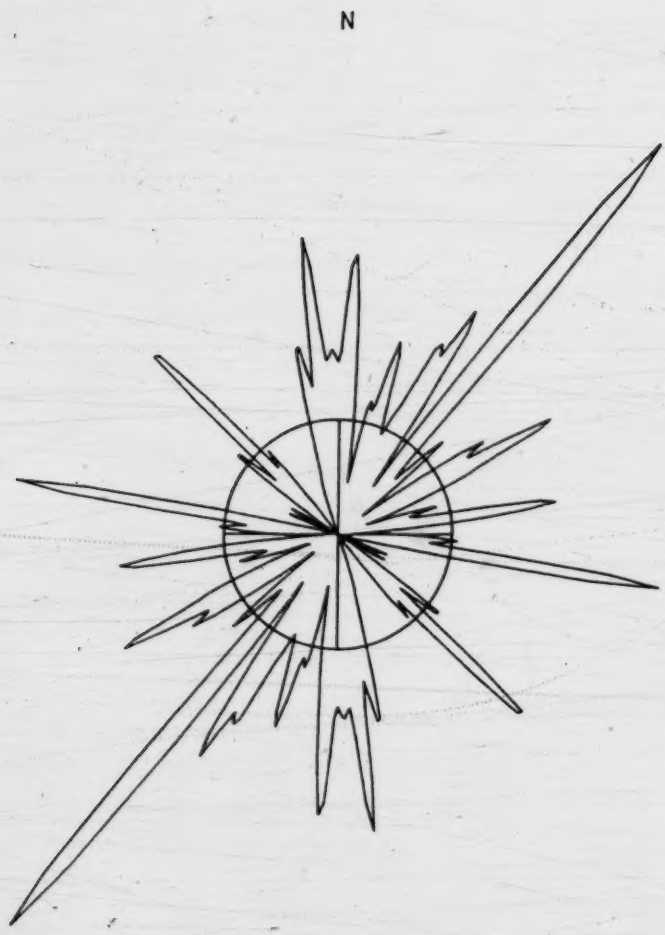

OPHIOLITES WEIGHTED EXCLUDING VALUES LESS THAN

2.5km K=1523 N=105

TREND	PLUNGE	EIGENVALUE/N
31.8	0.0	0.6336
121.8	0.0	0.3664
0.0	90.0	0.0

Figure 10. Smoothed Rose Histogram - Ophiolite Data.

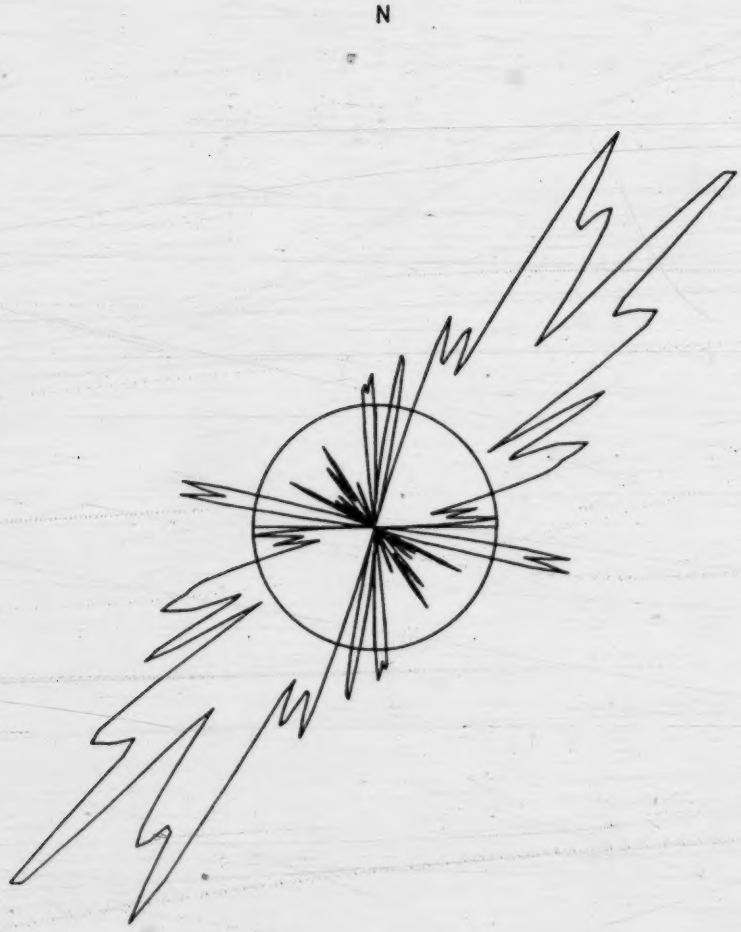

CARBONATES WEIGHTED EXCLUDING VALUES LESS THAN

2.5km K=1523 N=124

TREND	PLUNGE	EIGENVALUE/N
46.0	0.0	0.7708
136.0	0.0	0.2292
0.0	90.0	0.0

Figure 11. Smoothed Rose Histogram - Ordovician Carbonate Data.

DEER LAKE CLASTICS WEIGHTED EXCLUDING VALUES LESS THAN 2.5km K=1523 N=185

TREND	PLUNGE	EIGENVALUE/N
33.8	0.0	0.9352
123.8	0.0	0.0648
0.0	90.0	0.0

Figure 12. Smoothed Rose Histogram - Deer Lake Data.

inhomogeneous, in that they are composed of several rock types.

Radar Data Interpretation

The histograms for the RADAR data demonstrate that with a look direction from the southwest, the NW-SE trend is enhanced (Figures 13 to 19). This is in contrast to the Landsat data in which the N-S trend is enhanced by the low sun angle in the east. However the principle NE-SW or Appalachian trend still dominates each data set, except for that for the ophiolite suites (Figure 17). The ophiolite suite data do not exhibit a principle trend, as was observed with the Landsat data from the same units. This results from differing deformational behaviour of the components of the ophiolite suite as was suggested with Landsat lineament data

Certain data sets have a W to NW trend, (see Figures 13, 14 and 18), as was the case with their Landsat counterparts. This was recognised as a fold and fault trend in these units by (Bostock, 1983; Kennedy, 1979; Nyman et al., 1982; Shilleref and Williams, 1978 and Williams and Gillespie, 1981). This trend is also apparent in the Cambrian clastics (Figure 15).

Finally, the relationship of decreasing complexity with age suggested for the Landsat lineaments is supported in the radar histograms and their accompanying eigenvalues.

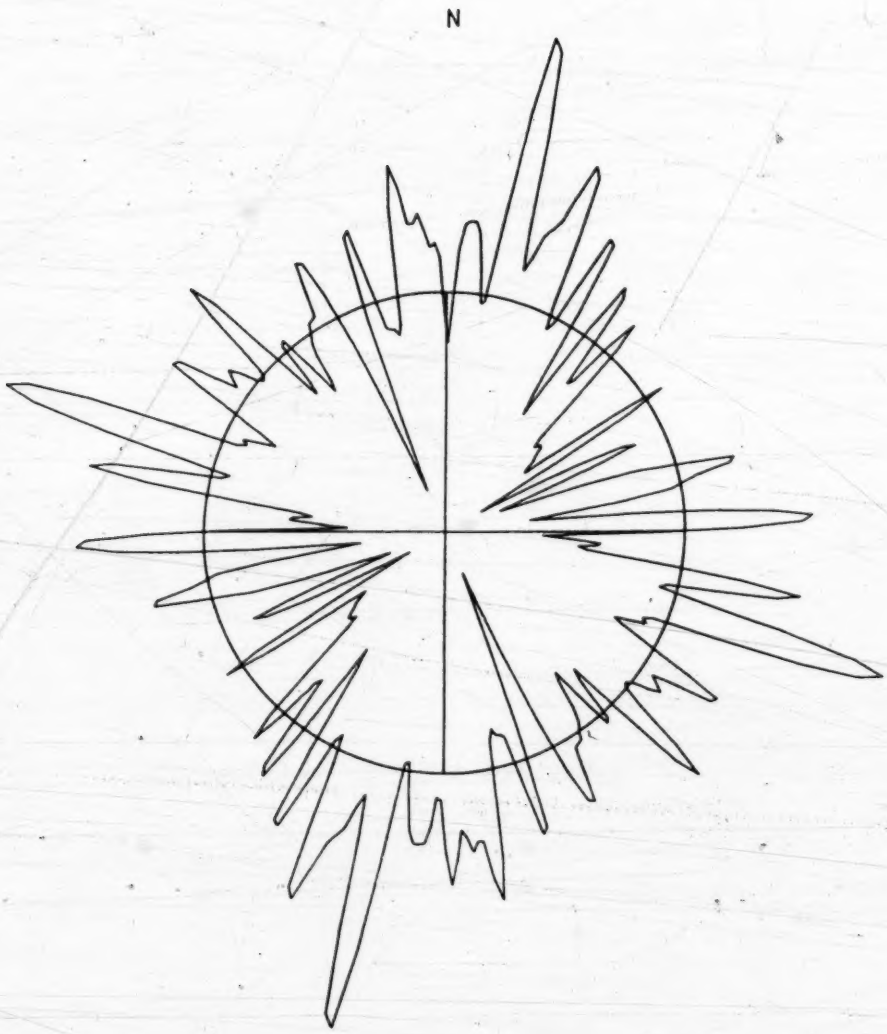

RADAR -BASEMENT WEIGHTED EXCLUDING VALUES

LESS THAN 2.5km K=1523 N=610

TREND	PLUNGE	EIGENVALUE/N
344.7	0.0	0.5474
74.7	0.0	0.4525
0.0	90.0	0.0

Figure 13. Smoothed Rose Histogram - Precambrian Basement Radar Data.

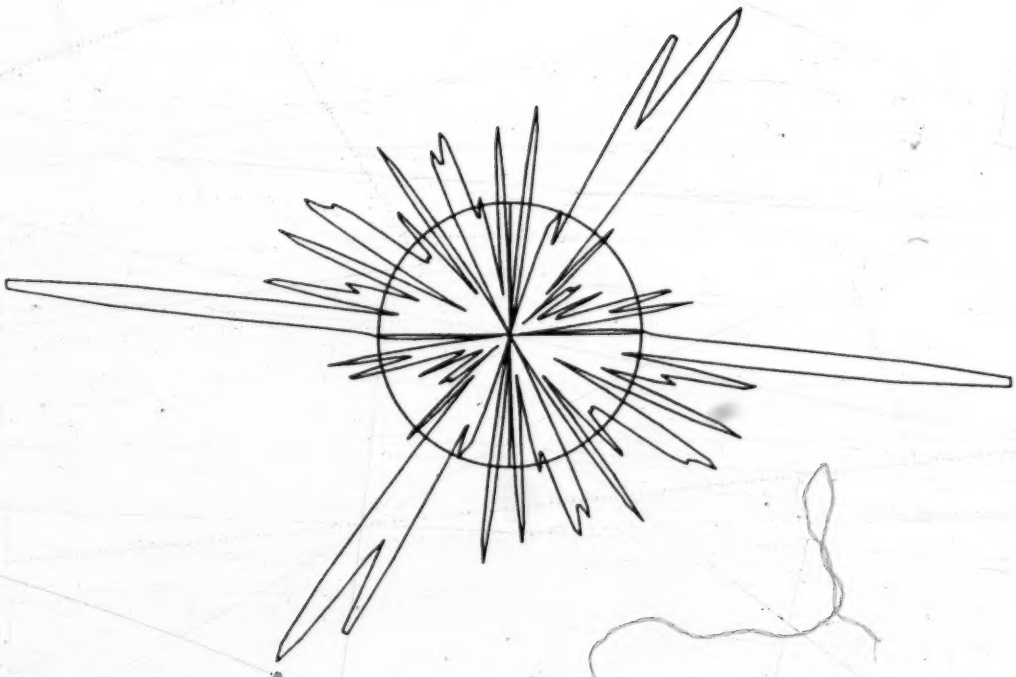

RADAR -CAMBRIAN CLASTICS METATAMORPHOSED WEIGHTED

EXCLUDING VALUES LESS THAN 2.5km K=1523 N=247

TREND	PLUNGE	EIGENVALUE/N
288.4	0.0	0.5435
18.4	0.0	0.4565
0.0	90.0	0.0

Figure 14. Smoothed Rose Histogram - Cambrian Clastics Metamorphosed Radar Data.

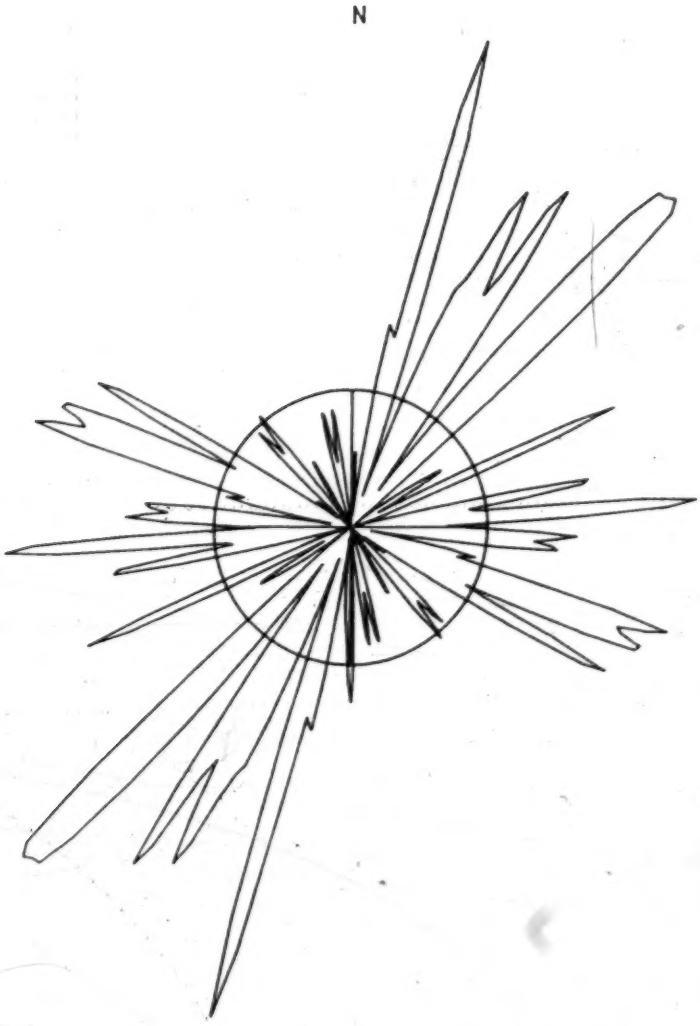

RADAR -CAMBRIAN CLASTICS WEIGHTED EXCLUDING VALUES LESS THAN 2.5km K=1523 N=160

TREND	PLUNGE	EIGENVALUE/N
53.7	0.0	0.6104
143.7	0.0	0.3896
0.0	90.0	0.0

Figure 15. Smoothed Rose Histogram - Cambrian Clastics Radar Data.

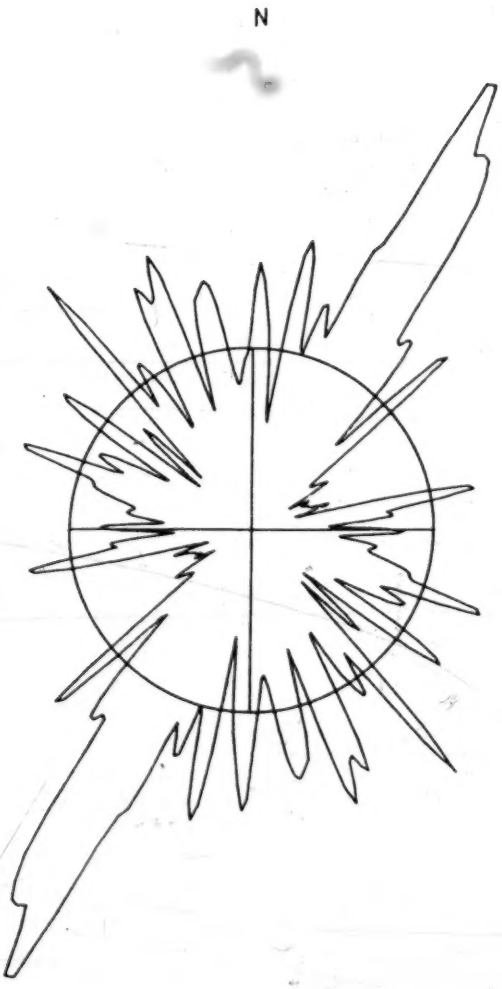

RADAR -TRANSPORTED CLASTICS WEIGHTED EXCLUDING

VALUES LESS THAN 2.5km K=1523 N=804

TREND	PLUNGE	EIGENVALUE/N
6.9	0.0	0.5973
96.9	0.0	0.4026
0.0	90.0	0.0

Figure 16. Smoothed Rose Histogram - Transported Clastics Radar Data.

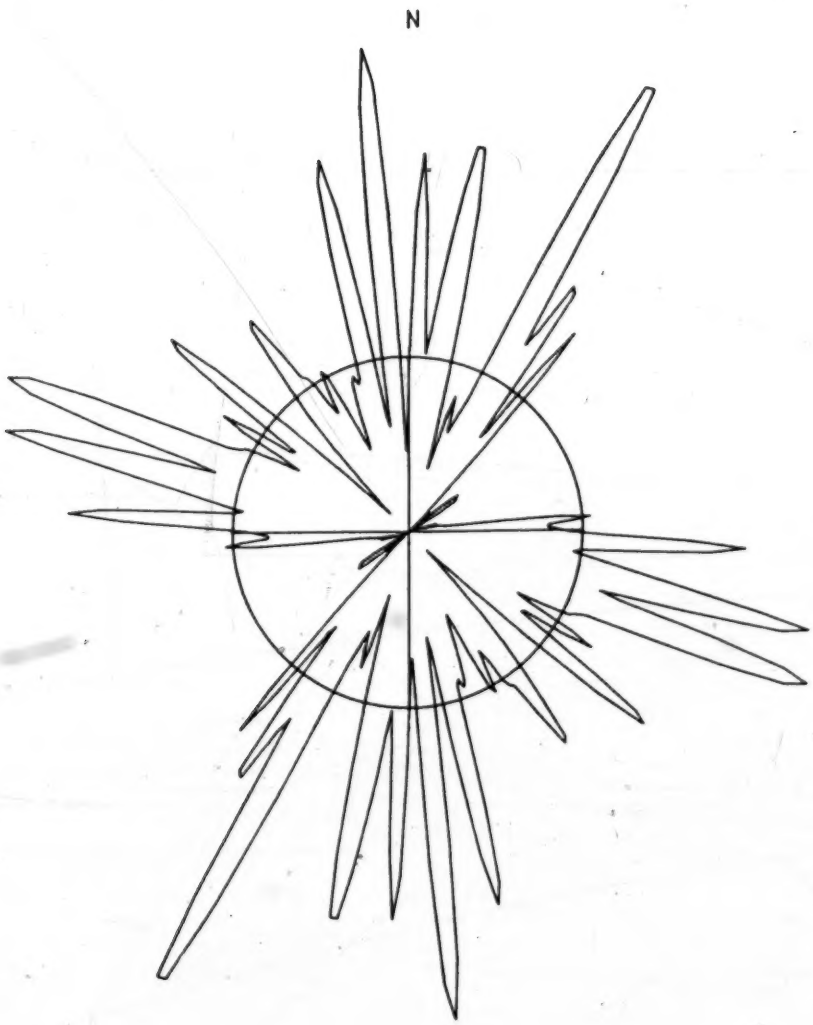

RADAR -OPHIOLITES WEIGHTED EXCLUDING VALUES

LESS THAN 2.5km K=1523 N=300

TREND	PLUNGE	EIGENVALUE/N
338.6	0.0	0.5985
68.6	0.0	0.4015
0.0	90.0	0.0

Figure 17. Smoothed Rose Histogram - Ophiolite Radar Data.

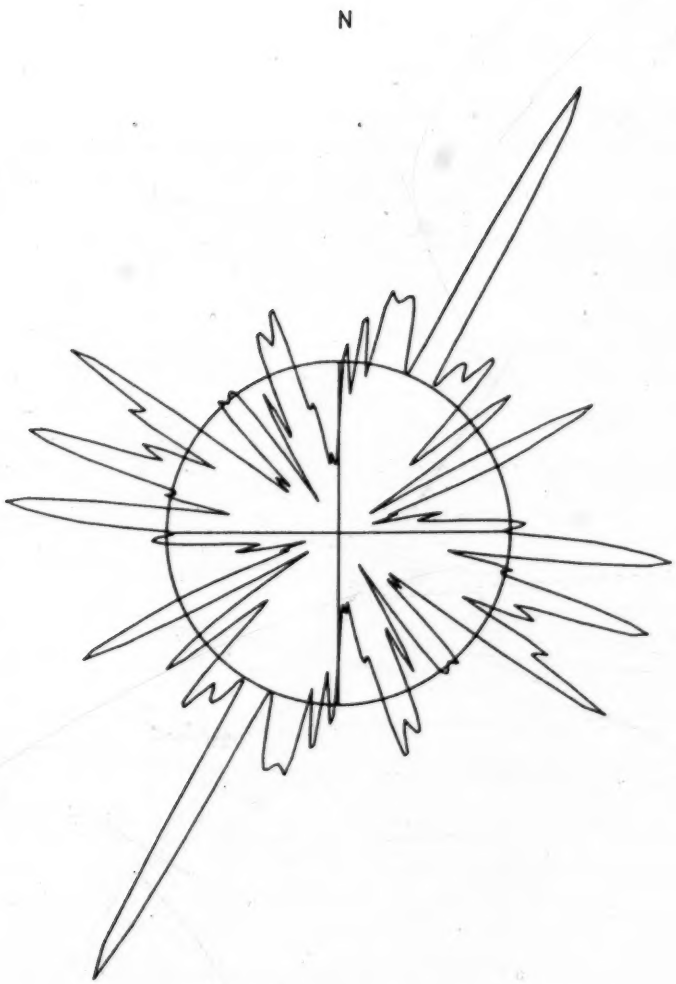

RADAR -ORDOVICIAN CARBONATES WEIGHTED EXCLUDING

VALUES LESS THAN 2.5km K=1523 N=440

TREND	PLUNGE	EIGENVALUE/N
34.1	0.0	0.5180
124.1	0.0	0.4820
0.0	90.0	0.0

Figure 18. Smoothed Rose Histogram - Ordovician Carbonate Radar Data.

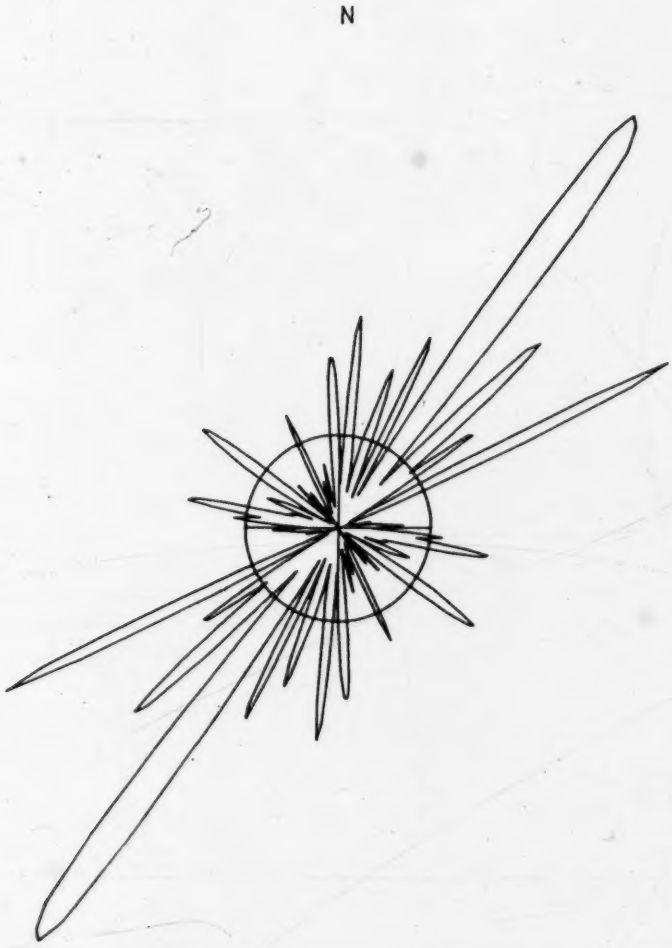

RADAR -DEER LAKE CLASTICS WEIGHTED EXCLUDING VALUES

LESS THAN 2.5km K=1523 N=279

TREND	PLUNGE	EIGENVALUE/N
37.2	0.0	0.6668
127.2	0.0	0.3332
0.0	90.0	0.0

Figure 19. Smoothed Rose Histogram - Deer Lake Radar Data.

C_4 Lineament Density Diagrams

Introduction

Previous lineament studies have commonly concentrated on producing linear feature maps (*e.g.*, Harris and Slaney, 1982; Heyl, 1983) or relating the density of major lineaments to mineralized districts (*e.g.*, Lang, 1982; Favorskaya and Volchanskaya, 1983). The aim of this part of the present study was two-fold:

1. To establish whether a spatial relationship exists between mineral occurrence distribution and lineament density highs, on a small scale.
2. To determine the regional structural trends of the area, using lineaments.

These objectives were achieved by contouring the density of lineaments over the area. Lineament density contouring enhances regional structural trends and reduces interpretation biases due to analyst subjectivity (Sawatzky and Raines, 1982). Furthermore, by superimposing the mineral occurrence distribution upon the lineament density contour map it is possible to establish if a visual spatial relationship exists between mineral occurrence distribution and lineament density. Areas of high lineament density should play host to more epigenetic mineral occurrences than areas of low lineament density, for faults provide passageways along which mineralizing fluids may travel.

Two types of density contour map were produced in this study, a Landsat Lineament Density Map and a Fluvio-Structural Lineament Density Map. Landsat lineaments were contoured for the first density map. Rivers and proven geological structures were contoured for the Fluvio-Structural Lineament Density Map.

Method

A grid with an interval of 6km by 6km was overlain on the lineament map used in the lineament orientation study. The grid was overlain so the N-S axis of the grid corresponded to the N-S direction of the image. The length of the lineaments (in mm) for each square of the grid was measured and this length and the centre coordinates of each grid square were entered into a master file. The master file was used as input for the contouring program of the Surface

II FORTRAN package. The contour interval was 10mm, which is equivalent to a 2.5 km lineament on the ground (see Figure 20). Initially the contour map produced from this package was placed on an optical reducer and the coastline and mineral occurrences superimposed upon this map from a topographic map. This technique proved to be inaccurate, due to the spherical aberration inherent in the optical reducer, this caused mineral occurrences and portions of the coastline at the extremities of the map to be mislocated. The problem was solved by digitizing each individual mineral location and the shorelines. These data were then overlain onto the lineament density contour map to produce an accurate map. Prior to location on the lineament density map, the mineral occurrences were separated into two groups. The first group was subdivided into metalliferous and non-metalliferous mineral occurrences (see Figures 20 and 21 respectively). The second group was subdivided into metalliferous, non-metalliferous lineament-related mineral occurrences and metalliferous, non-metalliferous non lineament-related mineral occurrences (see Figures 22 and 23 respectively). Division of the second group was based upon published geological information (see Mineral Development Division, Dept. of Mines and Energy Open File Nfld., 888, 1976). A mineral occurrence was ignored if there were insufficient data to determine whether or not it was lineament-related. The same method was used to obtain the fluvio-structural density map, but the lineaments were replaced by streams and geological structures (Figure 26).

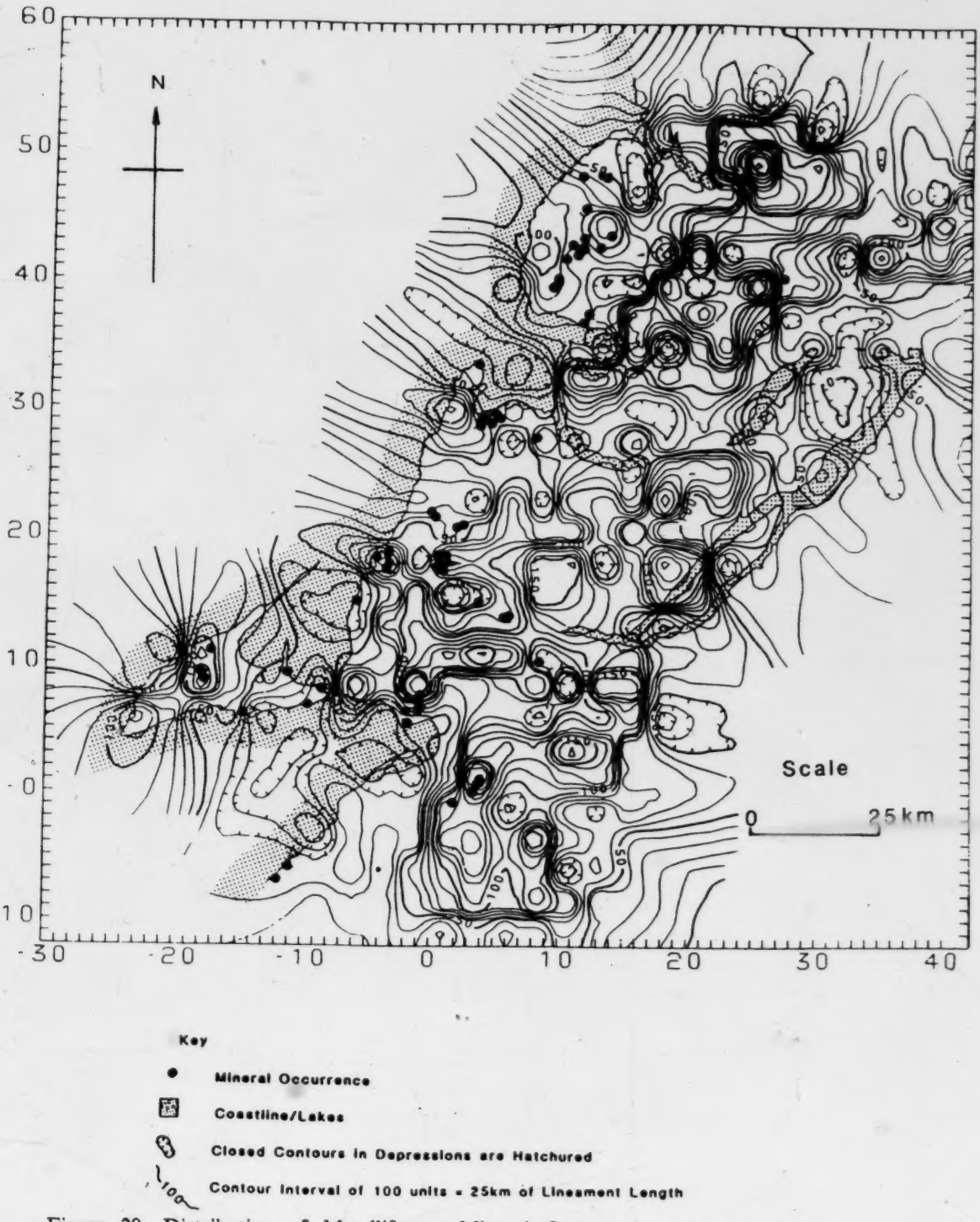

Key

- Mineral Occurrence
- Coastline/Lakes
- Closed Contours in Depressions are Hatchured
- Contour Interval of 100 units = 25km of Lineament Length

Figure 20. Distribution of Metalliferous Mineral Occurrences with respect to Lineament Density.

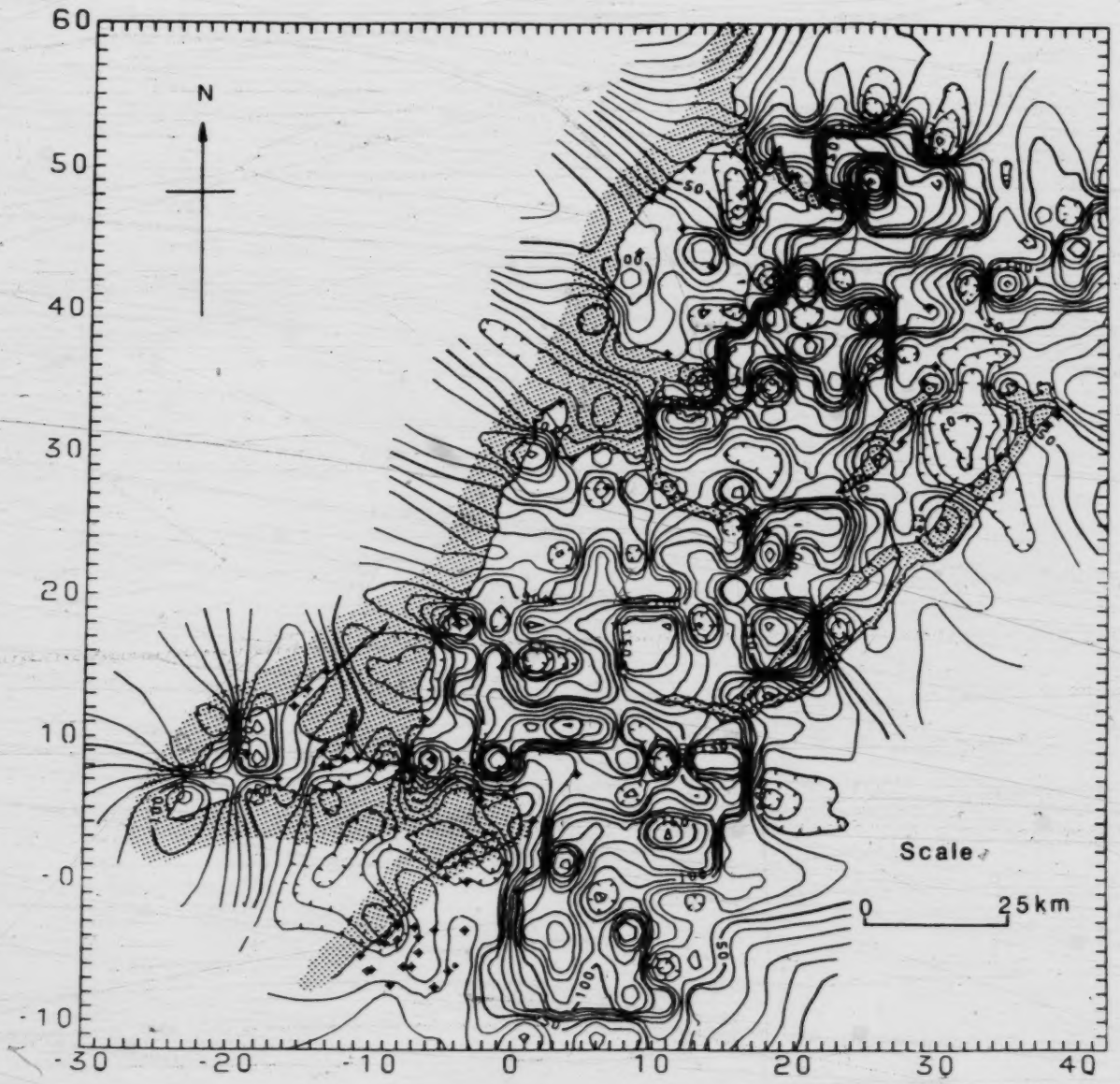

Figure 21. Distribution of Non-Metalliferous Mineral Occurrences with respect to Lineament Density

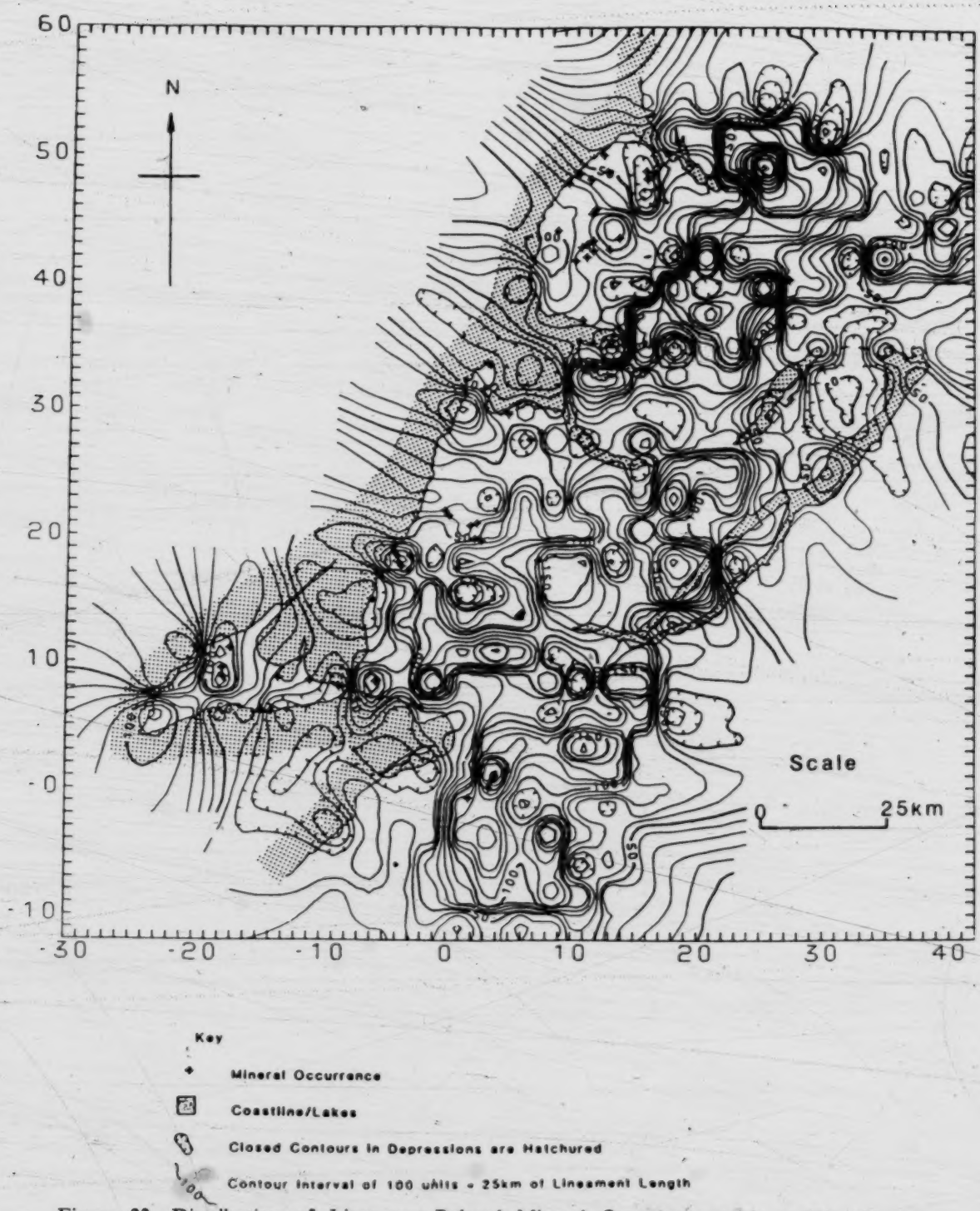

Figure 22. Distribution of Lineament-Related Mineral Occurrences with respect to Lineament Density.

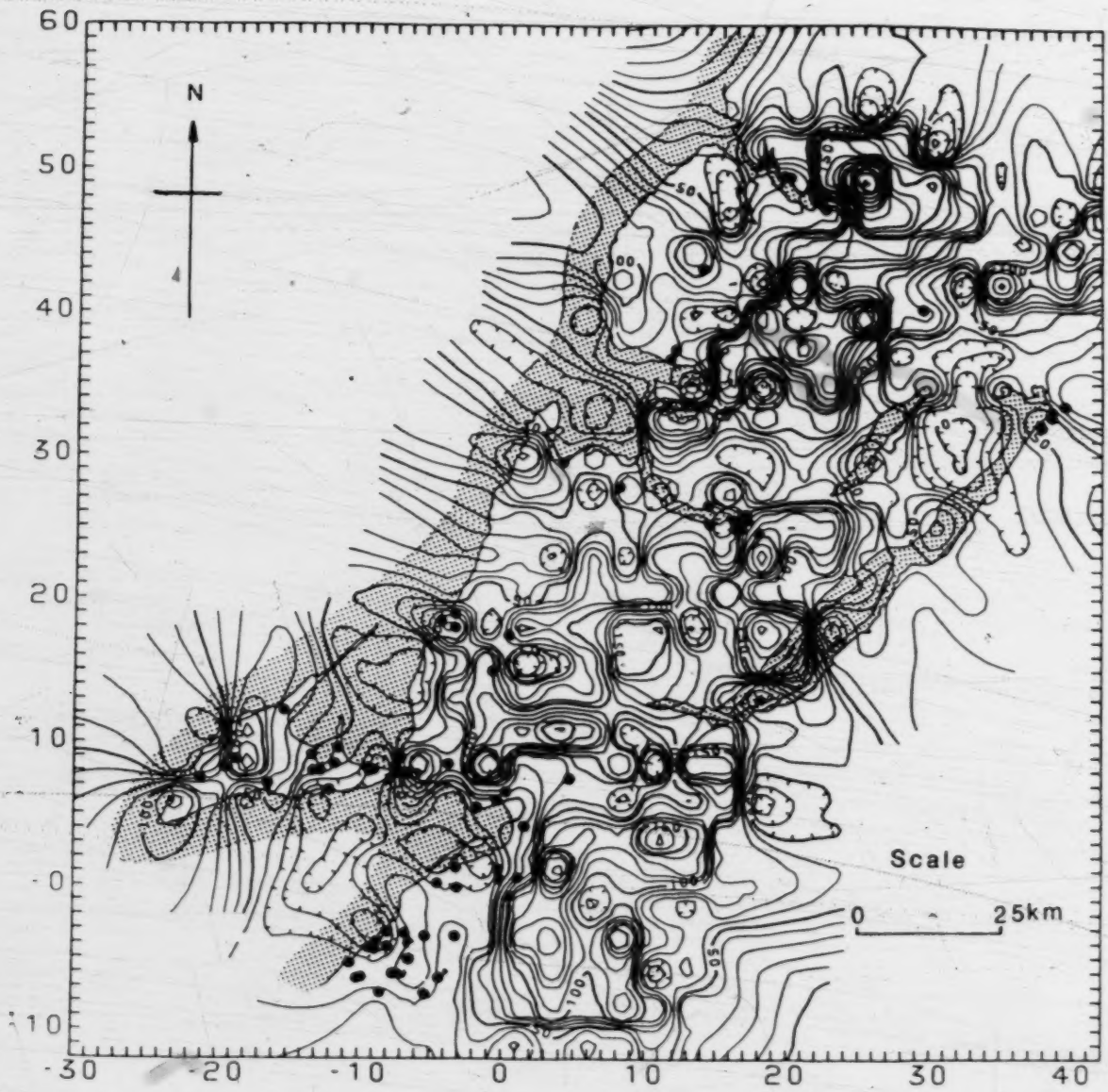

Figure 23. Distribution of Non Lineament-Related Mineral Occurrences with respect to Lineament Density.

Interpretation

Examination of the distribution of non-metalliferous and metalliferous mineral occurrences with respect lineament density in the region illustrates two points (Figures 20 and 21):

1. Most of the metalliferous mineral occurrences are related to high lineament density.
2. The majority of the non-metalliferous mineral occurrences are related to low lineament density.

However, this relationship is not consistent, as many metalliferous deposits are not related to lineaments (e.g., chromite cumulates) and many non-metalliferous deposits are related to lineaments (e.g., asbestos veins). Therefore, the mineral occurrences were divided into non lineament-related and lineament-related types (Figures 22 and 23). Most of the lineament-related types are associated with high lineament density values and certain clusters are associated with distinct highs (Figure 22). Some lineament-related types are not associated with high lineament densities, possibly because they are too small. The majority of non lineament-related types are associated with low lineament density values (Figure 23). Non lineament-related types not associated with low lineament density values are caused by their being too small or associated with much larger lineament-related types. An example of the latter are small chromite cumulate deposits associated with larger sheared, re-mobilized chromite deposits. This qualitative visual relationship of mineral occurrence distribution to lineament density highs was tested numerically. This was achieved by determining the percentage of the total number of mineral occurrences at set distances from the nearest density high. Results were compared for metalliferous versus non-metalliferous and lineament-related versus non lineament-related mineral occurrences (Figures 24 and 25). It is apparent that more of the metalliferous mineral occurrences are present than non-metalliferous mineral occurrences nearer the density highs. For example, at 10km away from the high 80% of the total metalliferous mineral occurrences are present compared to 42% of the non-metalliferous mineral occurrences. This suggests that the majority of metalliferous mineral occurrences are lineament-related as indicated in the geological literature.

A similar relationship exists with the lineament-related mineral occurrences and the non lineament-related mineral occurrences. For example, at 10km away from the high 77% of the lineament -related types are present compared with 45% of the non lineament-related types.

Certain metalliferous and non-metalliferous mineral occurrences were not separated into lineament and non-lineament related types, since there was insufficient geological information. If the excluded metalliferous mineral occurrences were lineament-related, this would account for the marginally greater number of metalliferous mineral occurrences compared to lineament-related types close to the highs. The greater number of non-metalliferous types compared to non lineament-related types close to the highs is explained if the excluded occurrences were lineament-related. An inherrant bias in this quantitative technique is that the analyst chooses the nearest high to the occurrence. Ideally circles whose radii represent the distance from the high should be drawn from all the highs. The area contained within these should be determined as a percentage of the total area and this area compared to the percentage of the mineral occurrences contained therein. If the distance from the high as a percentage of the total area is equivalent to the percentage of the total mineral occurrences, a spatial relationship does not exist. To test this, circles were drawn from each high in the ophiolite suite. Their area was determined as a percentage of the total area and compared to the percentage of lineament-related mineral occurrences discovered (Figure 26). This indicates that at a distance of 7.5km from the density high, which represents 18% of the total area, 68% of the total mineral occurrences were discovered. This substantiates the earlier conclusion that a spatial relationship does exist between linement-related mineral occurrence and lineament density highs.

The overall density patterns highlight the NE-SW fracture trend.

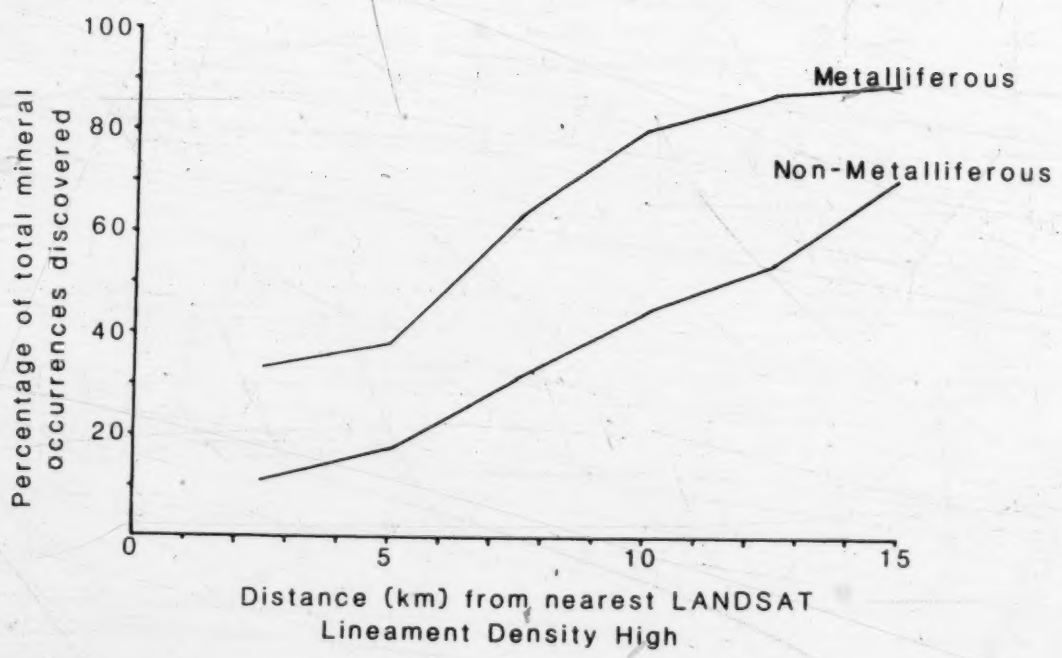

Figure 24. Number of Metalliferous compared to Non Metalliferous Mineral Occurrences discovered with distance from the nearest Landsat Lineament Density High.

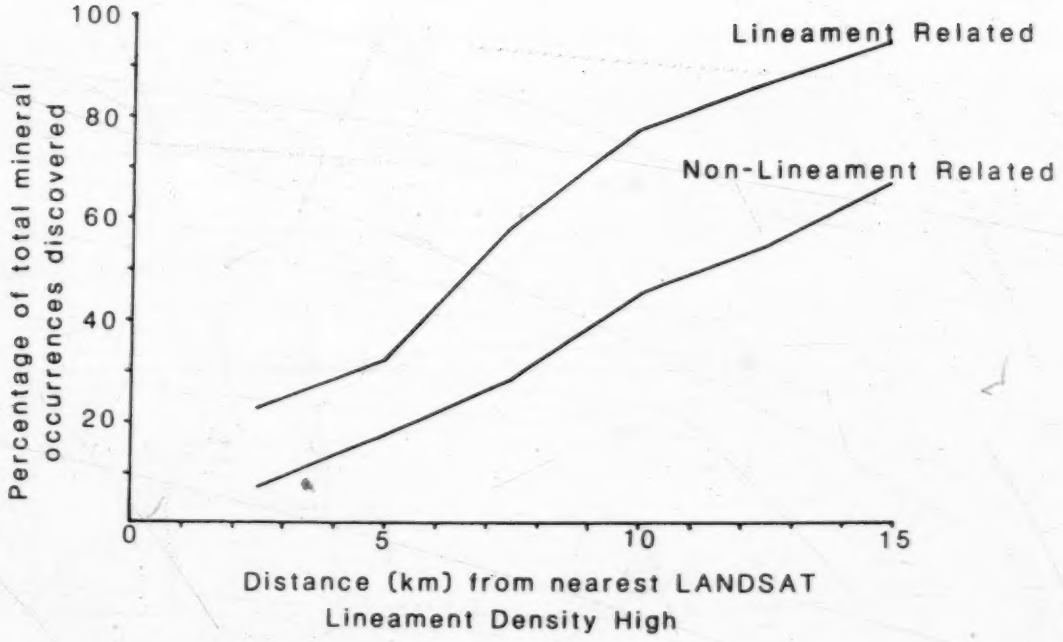

Figure 25. Number of Lineament-Related compared to Non Lineament-Related mineral Occurrences discovered with distance from the nearest Landsat Lineament Density High.

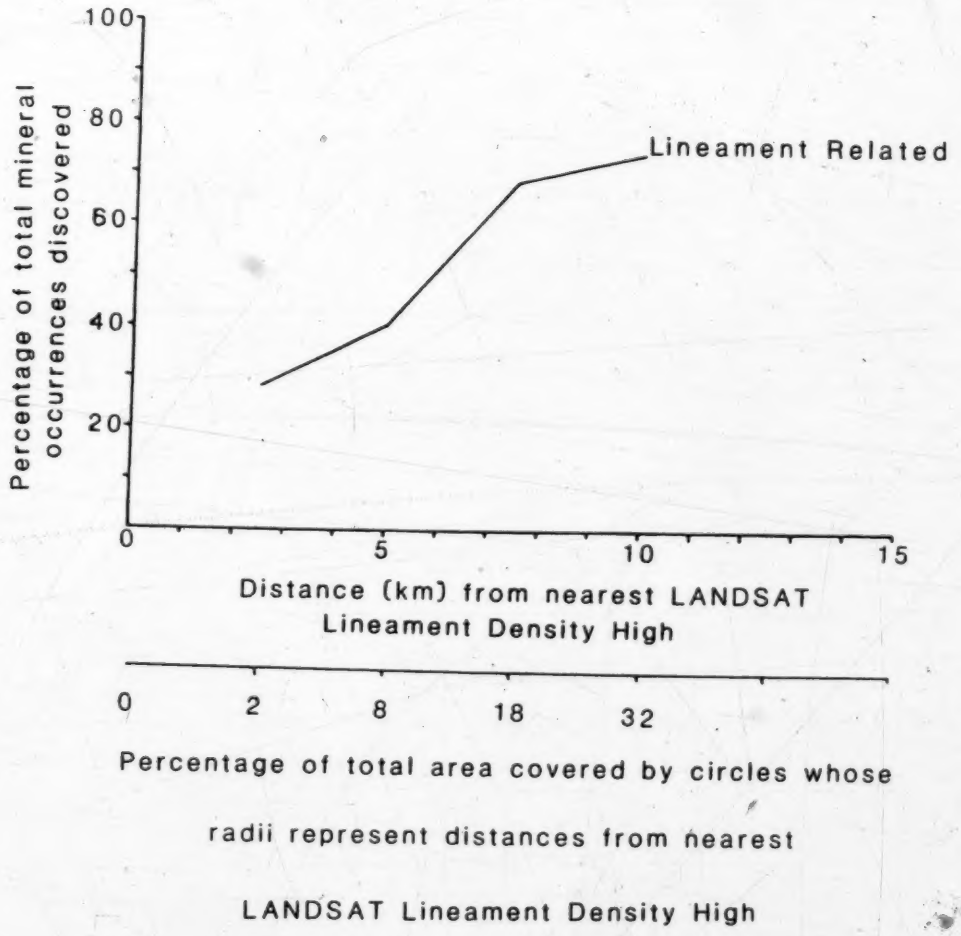

Figure 26. Percentage of total Lineament-Related mineral occurrences discovered from the nearest lineament density high within the Ophiolte Suite, and its relation to the percentage of the total area of the Ophiolite Suite.

The fluvio-structural density map was constructed on the basis that many streams follow fracture lines and were mapped in this study as lineaments on the Landsat image. Also, many of the major fractures on the lineament map are proven geological structures. Therefore, a combination of these should be similar to the lineament map and should show a similar relationship of fracture density to mineral occurrences. The distribution of metalliferous and non-metalliferous mineral occurrences with respect to fluvio-structural density is not as distinct as on the Landsat lineament denstiy map (Figures 27, 28). However there are some highs on the Fluvio-Structural density map which appear spatially related to mineral occurrences. Separation of the mineral occurrences into lineament-related and non lineament-related types does not improve this relationship (Figures 29 and 30). This spatial relationship of fluvio-structural density to mineral occurrence distribution was tested numerically using the method outlined for the Landsat lineament density map (Figure 31). The curves for the metalliferous and non-metalliferous mineral occurrences are almost identical. They show a linear relationship between area covered and pecentage of mineral occurrences discovered. These curves closely follow those for the non lineament-related and non-metalliferous mineral occurrences obtained from the Landsat lineament density map. This proves there is not a spatial relationship between fluvio-structural density and mineral occurrence distribution. The increase in the number of mineral occurrences with distance from the high is caused by an increase in the ground covered.

In a general sense the fluvio-structural density map highlights broad lithological changes. The Ordovican carbonate terrane is characterised by consistently low values. This would suggest the disappearance of surface drainage due to a low water table in the carbonates. The Carboniferous clastics are characterized by high values, possibly because they are impervious, and form the coastal lowlands carrying the runoff from the adjacent highlands.

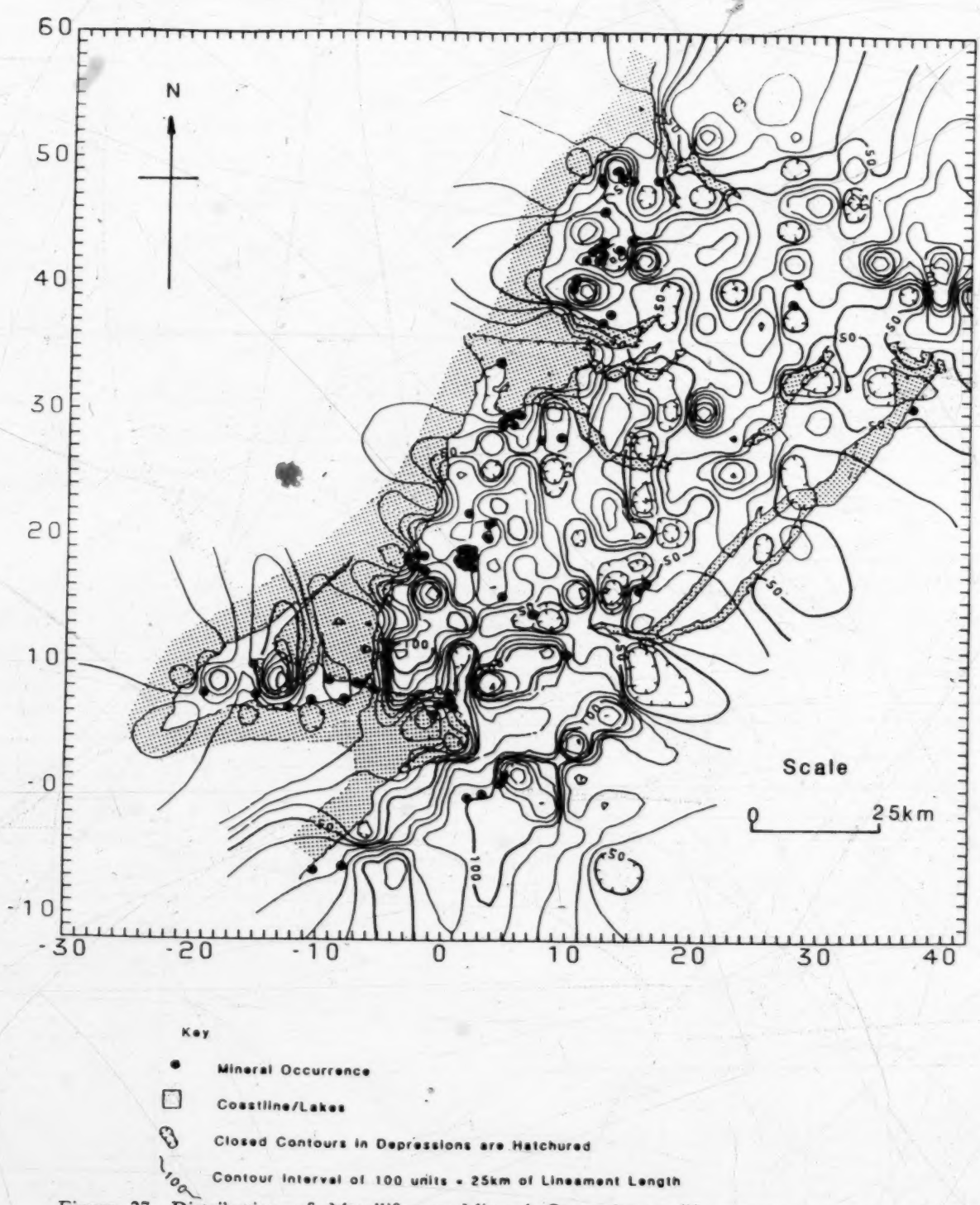

Figure 27. Distribution of Metalliferous Mineral Occurrences with respect to Fluvio-Structural Density.

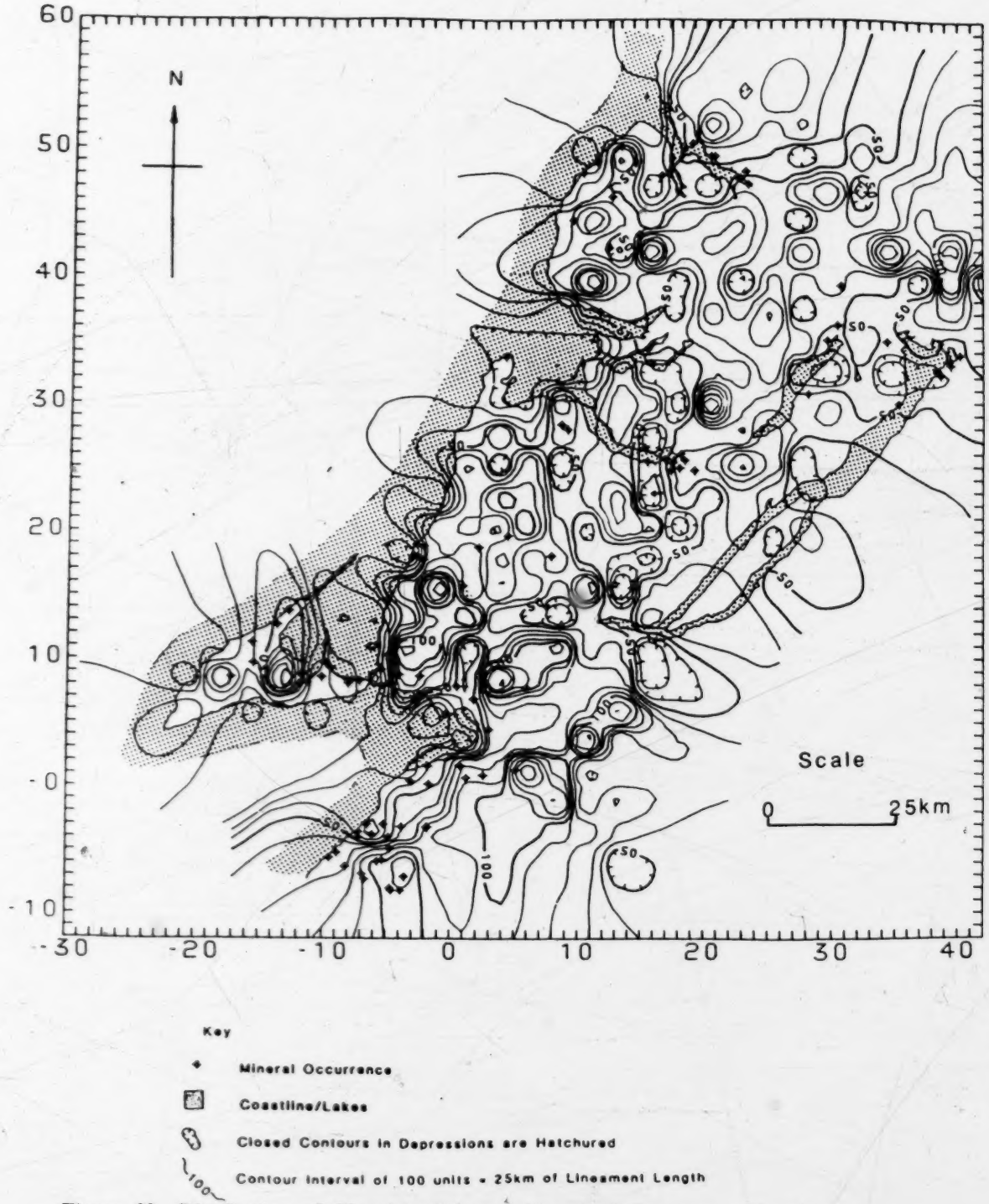

Figure 28. Distribution of Non-Metalliferous Mineral Occurrences with respect to Fluvio-Structural Density.

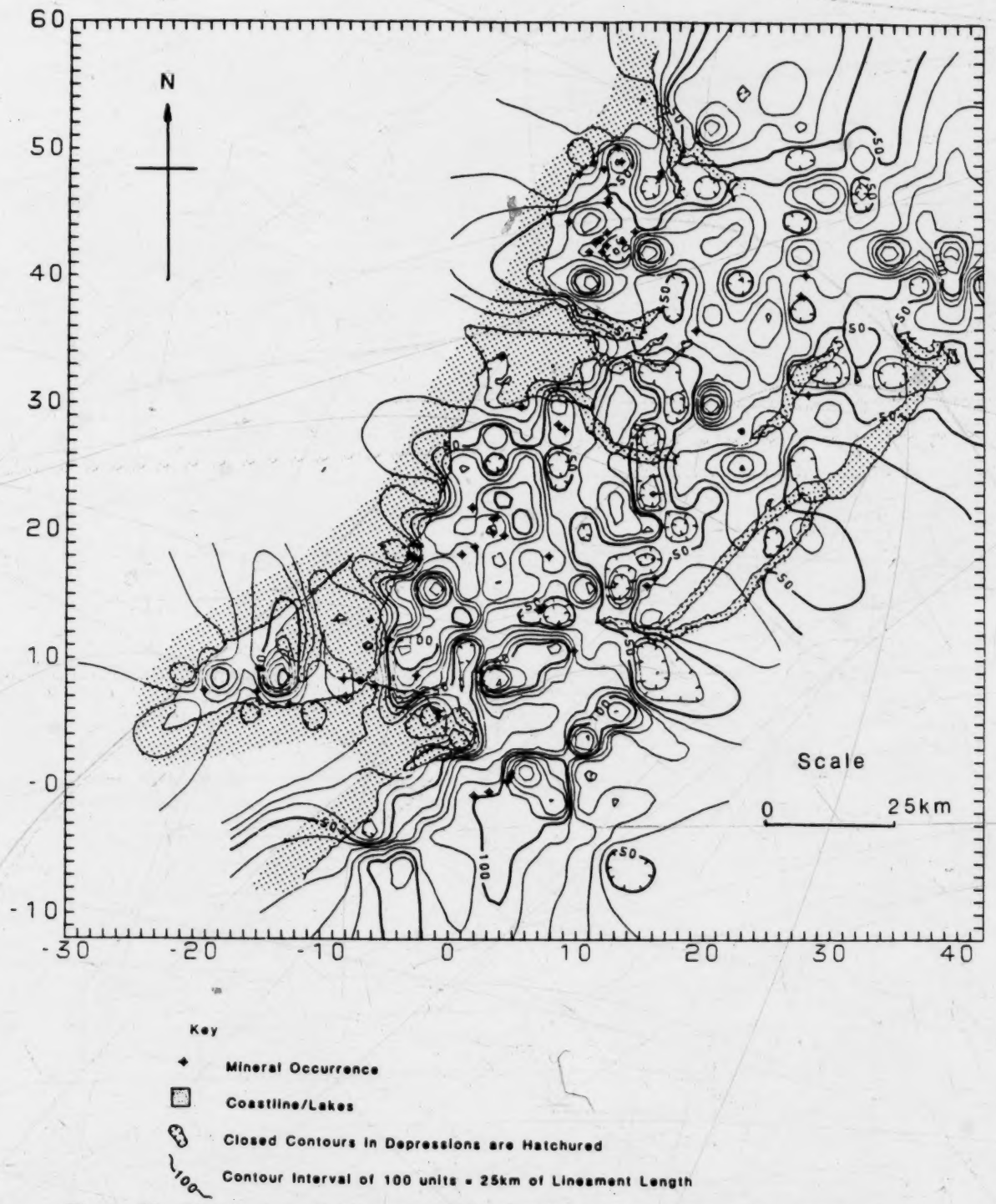

Figure 29. Distribution of Lineament-Related Mineral Occurrences with respect to Fluvio-Structural Density.

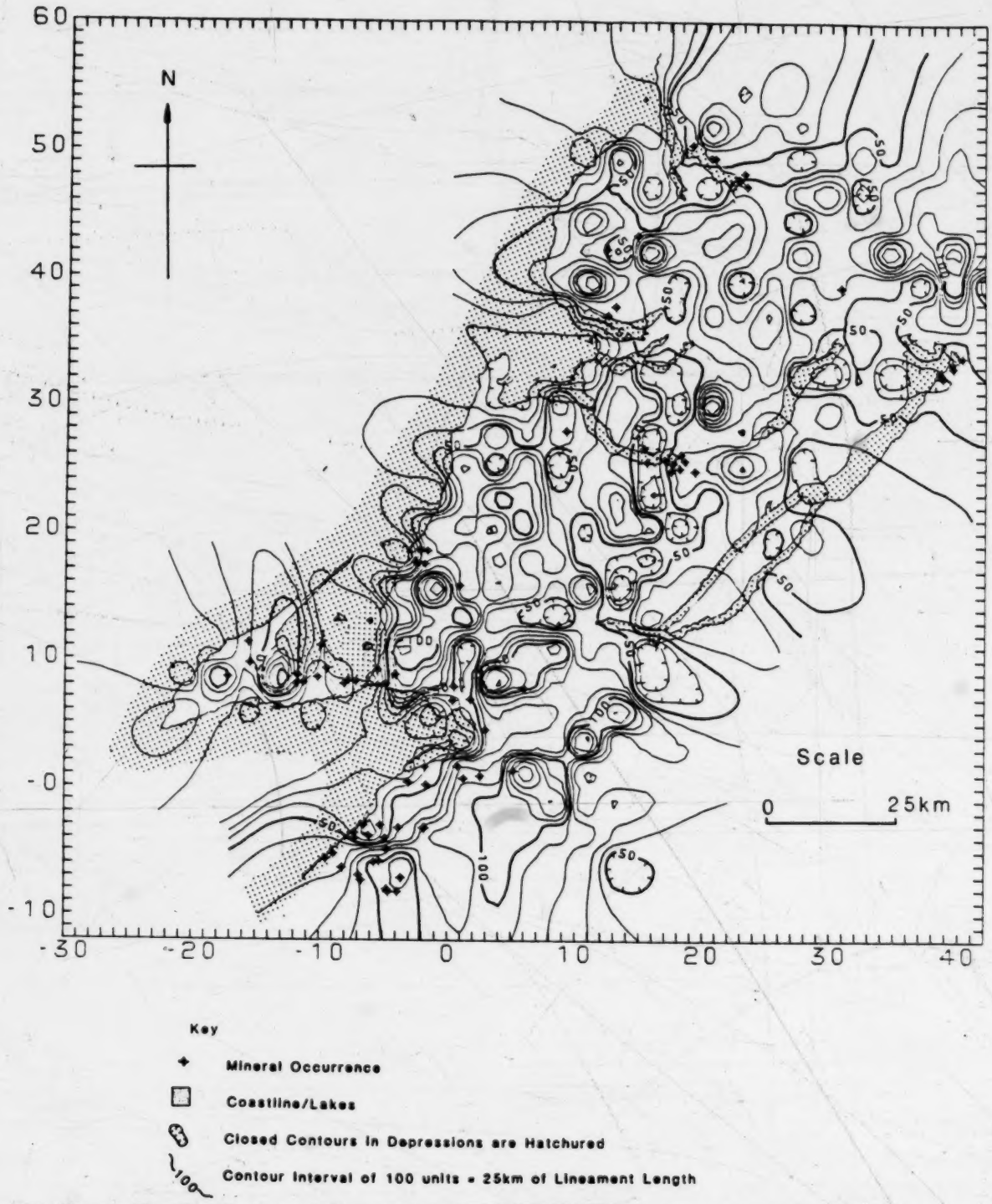

Figure 30. Distribution of Non Lineament-Related Mineral Occurrences with respect to Fluvio-Structural Lineament Density.

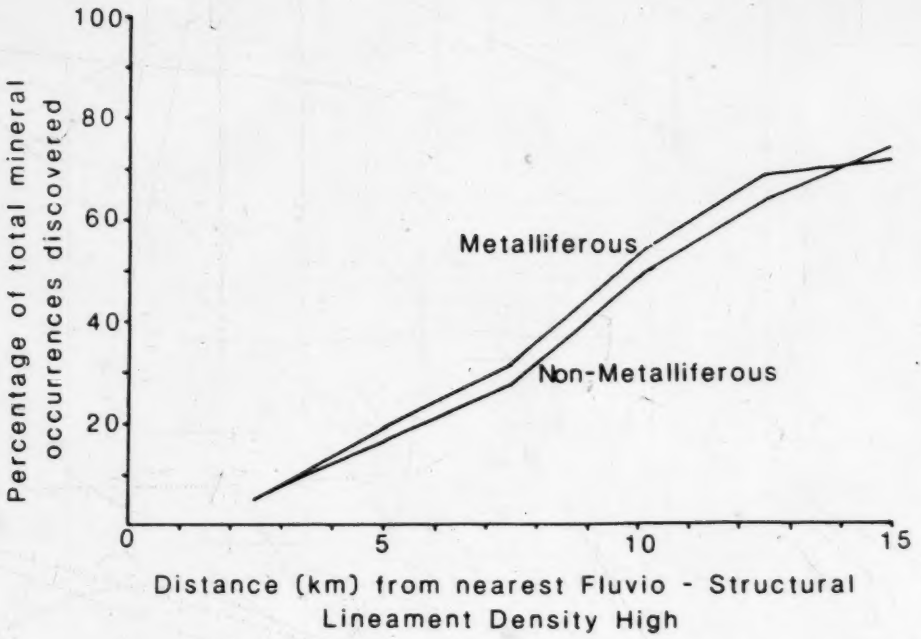

Figure 31. Number of Metalliferous compared to Non-Metalliferous mineral occurrences discovered with distance from the nearest Fluvio-Structural density high.

D. Conclusions

Landsat lineament density contouring highlights the NE-SW structural trends and indicates a close numerical and visual spatial relationship of landsat lineament density highs and lineament-related mineral occurrences distribution. This relationship is not apparent using existing fluvial and structural data. This demonstrates the use of Landsat imagery for discerning lineaments which were not indicated on existing geological maps.

IV. Spectral Analysis

Introduction

Landsat imagery was evaluated as a tool for lithological and alteration zone mapping and mineral exploration in a northern maritime enviroment. Initial interpretations were 'ground truthed'[3] during the summer of 1984 and ground truth spectra and samples collected. Spectral curves were obtained from the samples and together with the field spectra, used to refine and explain the intial interpretations. Lithological mapping concentrated on distinguishing the igneous rock types of the area, predominantly those of the ophiolite suites of the Hare Bay and Humber Arm Allochthons. Spectral interpretations are given for the Basement and units of the Ophiolite Suite. These lend themselves to identification by satellite due to their relatively sparse vegetation cover. Therefore, an understanding of their ground spectral behaviour should establish if they can be identified by satellite imagery, and if so, the cause of this particular spectral signature.

The spectral data are presented for the wavelengths between 500nm and 3500nm, except for two regions, namely: 1300nm to 1500nm and 1800nm to 2000nm. These regions are occupied by strong atmospheric absorption bands, excluding data collection. The Landsat data were obtained using two types of scanner, a Multispectral Scanner (MSS) and a Thematic Mapper (TM). The MSS gathers spectral data in four bands, the TM in seven bands. The positions and widths of these bands within the electromagnetic spectrum are given in Table 2. It should be noted that the four MSS bands on Landsats 1, 2 and 3 were numbered band 4, band 5, band 6 and band 7. The corresponding MSS bands on Landsats 4 and 5 were numbered band 1, band 2, band 3 and band 4 (Table 2). The numbering system used for the MSS band on Landsats 1,2 and 3 has been used here even though the data were gathered by Landsat 4. This allows the numbering in the literature, which is largely limited to data from Landsats 1, 2 and 3, to match these data. The MSS has a spatial resolution[4] of 80m x 80m compared with a 30m x 30m spatial resolution for the TM. The MSS and TM data were compared to establish which aspects of lithological and alteration discrimination most suited each system.

---

[3]Ground truthing is the remote sensing term for field checking

[4]Spatial resolution refers to the size of the ground cell from which the scanner obtains a reflectance value.

Table 2. Multispectral Scanner (MSS) and Thematic Mapper (TM) Wavelength Ranges.

Multispectral Scanner (MSS)			Thematic Mappper (TM)		
Landsat 1, 2, 3	Landsat 4, 5				
Band	Band	Wavelength	Band	Wavelength	Centre
4	1	500-600 nm	1	450-520 nm	480 um
5	2	600-700	2	520-600	560
6	3	700-800	3	630-690	660
7	4	800-1100	4	760-900	830
			5	1550-1750	1650
			7	2080-2360	2200
			6	1060-1250	1160

A. Laboratory Spectra

Introduction

Previous work on the spectral reflectance of ultramafic, mafic and granitic rocks in the visible and near infrared (350 to 2500nm) involved laboratory analyses of powdered specimens, (Hunt and Salisbury, (1970, 1978); Hunt *et al.*, (1971, 1973a, 1973b, 1974); Hunt, (1977, 1979) and Hunt and Ashley, (1979)). Few previous studies concentrated on the spectral behaviour of the naturally-occurring weathered surfaces of these rocks (Hunt and Wynn, 1979; Blom *et al.*, 1980; Botherel *et al.*, 1984; Rothery, 1984). This study was concerned with interpreting the reflectance spectra from the naturally-occurring weathered surfaces and establishing whether these data could be used to discriminate lithologies using Landsat MSS and TM data.

Spectral Features

It was not the aim of this study to determine the cause of the spectral features observed. However a brief review of the causes of absorption phenomena features is pertinent. This has been based on papers by Hunt and Salisbury (1970), Hunt *et al.* (1971, 1973a and

1974), Hunt (1977), and Blom *et al.* (1980). The major components of rocks, Si-O tetrahedra, do not display intrinsic spectral features in the energy range under investigation. Elements present in minor quantities are the cause of the spectral features observed. The absorption features present result from electronic or vibrational processes.

Absorption bands resulting from electronic processes are usually broader than those arising from vibrational processes and are of two types in these spectra. Firstly, **Crystal Field Effects**; these result from the fact that isolated atoms and ions can only exist in discrete energy states. Absorption or emission of specific wavelengths of electromagnetic radiation results from changes from one energy state to another. Secondly, **Charge Transfer**; this refers to the process whereby absorped energy causes an electron to migrate between neighbouring ions and ligands.

Crystal field and charge transfer effects observed in these spectra result from iron in either the ferric (Fe^{3+}) or ferrous (Fe^{2+}) valence state. Charge transfer in Fe-O accounts for the decrease in reflectivity wavelengths shorter than 600nm. Crystal field effects resulting from ferrous iron produce broad bands at approximately 650nm, 1000-1100nm and 1800-1900nm or 2200-2300nm depending upon crystal structure. Crystal field effects resulting from ferric iron produce absorption bands at 650nm and 870nm.

Vibrational processes occur at longer wavelengths and produce narrow absorption bands. They result from the fact that any vibrating system is made of a restricted number of simple motions termed "normal modes" or "fundamentals". The number and form of these modes are determined by the energy values of, and number and type of constituent atoms, their binding forces and spatial geometry. If two quanta of energy are involved, an overtone occurs, producing a band at twice the frequency. Combinations of fundamentals and/or overtones result in combination tone features near the sum of the frequencies involved. The energy required to excite the fundamental modes of geological materials lies outside the energy range under investigation. Consequently, the features observed result from overtones and or combination tone features. The features present in these spectra result from vibrational processes associated with the hydroxyl (OH) group, specifically caused by Al-OH or Mg-OH associated with clays, micas and or amphiboles. The location of the more intense feature depends upon whether aluminium or magnesium is present. If the element is aluminium, the more intense feature occurs at 2200nm if magesium, the more intense feature occurs at 2300nm (Hunt *et. al.* 1977).

Spectral Data Collection and Analysis

Spectral data were collected in the laboratory using a Barringer-Magenta Hand Held Ratioing Radiometer (HHRR), with narrow band filters (30- to 45-nm) under fixed lighting conditions (P. Lawrence Pers. Comm. 1984). A HHRR was also used to gather the ground truth spectra. The design and operation of the HHRR is given in Appendix I. The spectral data were gathered from the weathered surfaces of samples collected during the 1984 field season. Spectral interpretations are given for data from the Basement, and Ophiolite Suite (Ultramafics and Serpentinites, Gabbros, Sheeted Dykes and Pillow Basalts).

Basement Granitic Rocks

Two absorption bands are observed in both spectra at 2250nm and 2350nm, and also a sharp decrease from 630nm to shorter wavelengths (Figure 32). This sharp decrease is typical of Ferric Oxide and results from Fe-O charge transfer (Hunt *et al.*, 1973).

The sharp absorption bands at 2250nm and 2350nm indicate the presense of hydroxyl combination groups of Mg-OH or Al-OH. Since the 2250nm band is more intense than the 2350 band Al-OH is present (Hunt *et al.*, 1977). The Al-OH molecule results from clays (probably kaolinite) formed by weathering of feldspars.

Ultramafics and Serpentinites

The samples of ultramafic rocks consist of olivine, orthopyroxene and chromium spinel, the olivines and pyroxenes have been strongly serpentinized. The ultramafic rocks are harzburgites and their spectra have absorption bands at 950nm, 2150nm and 2350nm (Figure 33). The fall off in reflectance from 680nm is typical of charge transfer in ferric oxide in ultramafic rocks (Hunt *et al.*, 1974; Longshaw, 1975; Hunt and Wynn, 1979; Blom *et al.*, 1980). It is caused by the strong ferric oxide stain on the surface of the rock. There may have been some contribution to the marked fall-off in this region by ferrous and chromium ions. Ferrous ion present in olivine produces a weak absorption feature at 510nm (Hunt *et al.*, 1973). The Chromium (Cr^{3+}) ion produces an absorption band at 550nm (Hunt and Wynn, 1979). The band at 900nm is characteristic of ferric oxide (Hunt and Salisbury, 1971a). This results from the strong ferric oxide stain present from weathering of the pyroxenes and olivines and giving the weathered surfaces an orange/brown appearance. The bands at 2150nm and 2350nm are

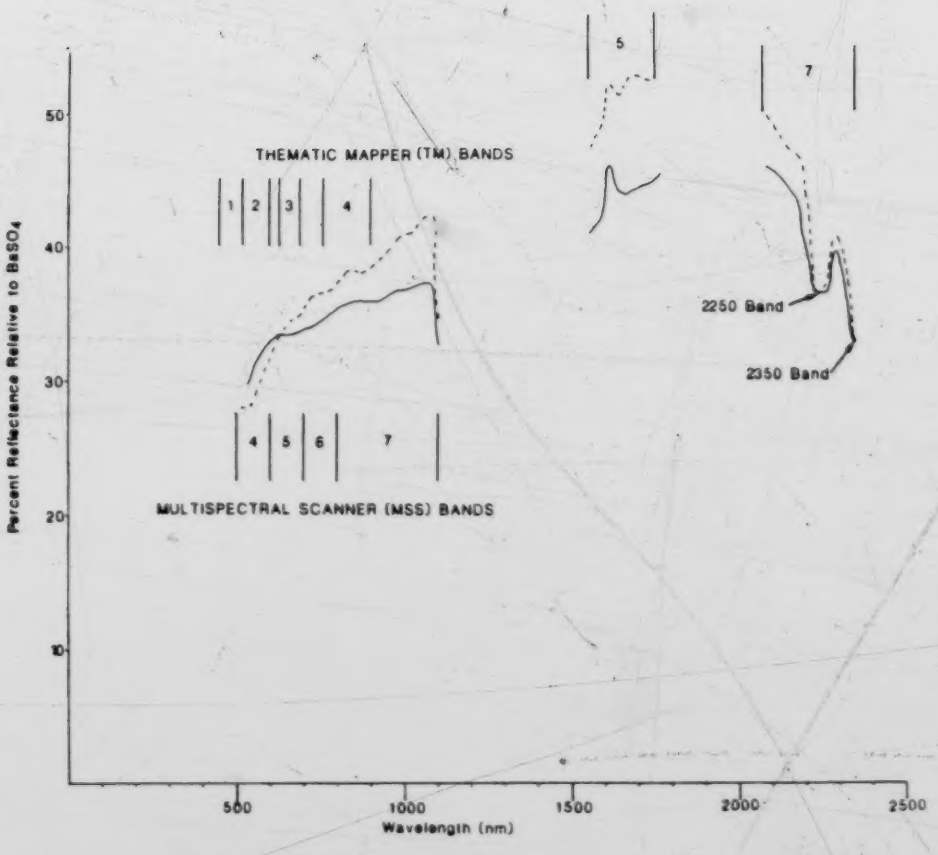

— Sample 6a(1) Granitic
--- Sample44(1) Granitic

Figure 32. Spectral Relectance Curves for Samples from the Basement

combination tone bands. The 2350nm feature is more intense than the 2150nm feature, indicating the presence of Mg-OH bonding (Hunt, 1977). Such Mg-OH bonds occur in serpentine, the presence of which was confirmed petrographically.

The serpentine spectra are characterised by absorption bands at 750nm, 900nm, 2150nm and 2350nm, and a reflectance high at 580nm (Figure 33). Botherel *et al.* (1984), note the reflectance high accounts for the green colour of serpentine and recognise absorption bands at 740nm and 930nm which they ascribe to ferrous ion in the octahedral site after work by Cervelle and Maquet (1982). Hunt *et al.* (1970), observed a band at 700nm in their spectra collected from serpentine which they acribed to ferric ion. This band at 710nm probably results

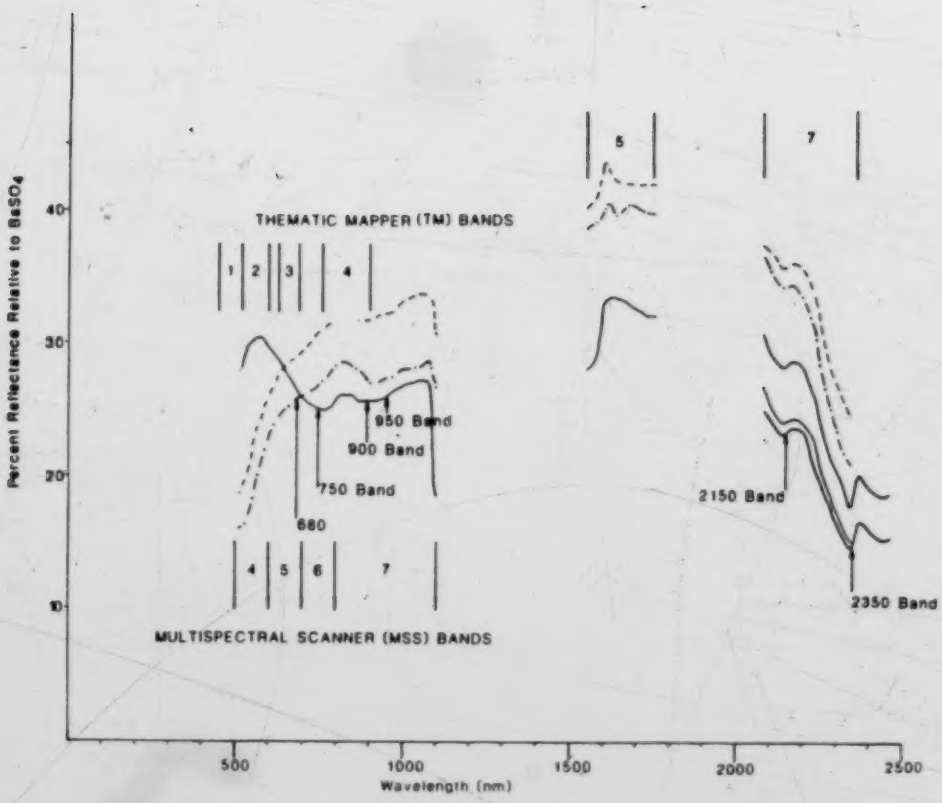

--- Sample (15)(a) Harzburgite (Serpentinised)
--- Sample (15)(b) Harzburgite (Serpentinised)
— Sample 7(15) Serpentine / Talc
Extended Scan -(1)
Extended Scan -(2)

Figure 33. Spectral Reflectance Curves For Samples of Ultramafics and Serpentintes.

from a mixture of both ferric and ferrous ions. The absorption feature at 900nm is ascribed to ferrous ion (Botherel *et al.*, 1984). The bands at 2150nm and 2350nm indicate Mg-OH bonding present in serpentine. (Hunt *et al.*, 1970). Curves 7(15)a and 7(15)b are extended scans on sample 7(15) in the region associated with hydroxyl absorption. They are essentially the same except for a difference in the reflectance intensity. This intensity difference results from sample

b being rotated 180° with respect to sample a. This illustrates that although the intensity of the spectra will vary with the illumination direction, the shape of the spectral curve will remain constant.

The Gabbros

Petrographic examination of these samples indicate they are dominated by plagioclase and augite and have larger quantities of opaques than the ultramafic rocks. The feldspars have been sericitized, the augites are partially chloritised, and there is evidence of serpentinization. The sample from locality 38(16)a has a marked fall-off in reflectance from 600nm, and absorption bands at 900nm, 1050nm, 2130nm and 2350nm (Figure 34). The short wavelength fall-off is attributed to Fe-O charge transfer, resulting from ferric ion present as a stain on the surface of the sample. The bands at 900nm and 1050nm are attributed to crystal field transitions in ferric and ferrous ions respectively (Hunt *et al.*, 1970). The features at 510nm and 900nm were not observed in spectral analyses of gabbros by Hunt *et al.* (1974), and by Blom *et al.* (1980). They result from a strong iron stain on the surface of the gabbro. The ferrous iron feature at 1050nm has been recognised in augite and hornblende (Hunt *et al.*, 1970). Both these minerals are present in this sample. The more intense feature at 2350nm relative to 2150nm indicates Mg-OH bonding is present (see previous discussion). Mg-OH bonding occurs in hornblende and in serpentine Hunt *et al.* (1970), both of which were confirmed petrographically.

Sample 38(16)b has a fall-off in reflectance from 570nm and absorption bands at 650, 750nm and 1000nm (Figure 34). The fall-off in the blue results from Fe-O charge transfer in ferric ion present as a surficial stain on the sample surface. The bands at 650nm, 750nm and 1000nm are typical of the ferric and ferrous ions present in pyroxenes and in amphiboles (Hunt *et al.*, 1970). However, the absense of any bands in the 2100nm to 2450nm region typical of amphibole, suggests pyroxene (augite) is the cause.

Sample 63(16) has a fall-off from 630nm and absorption bands at 600nm and 780nm (Figure 34). The short wavelength fall-off is caused by ferric oxide (see previous sample). The bands at 650nm and 780nm are caused by ferrous and ferric ions respectively and are typical of augite (Hunt *et al.*, 1970).

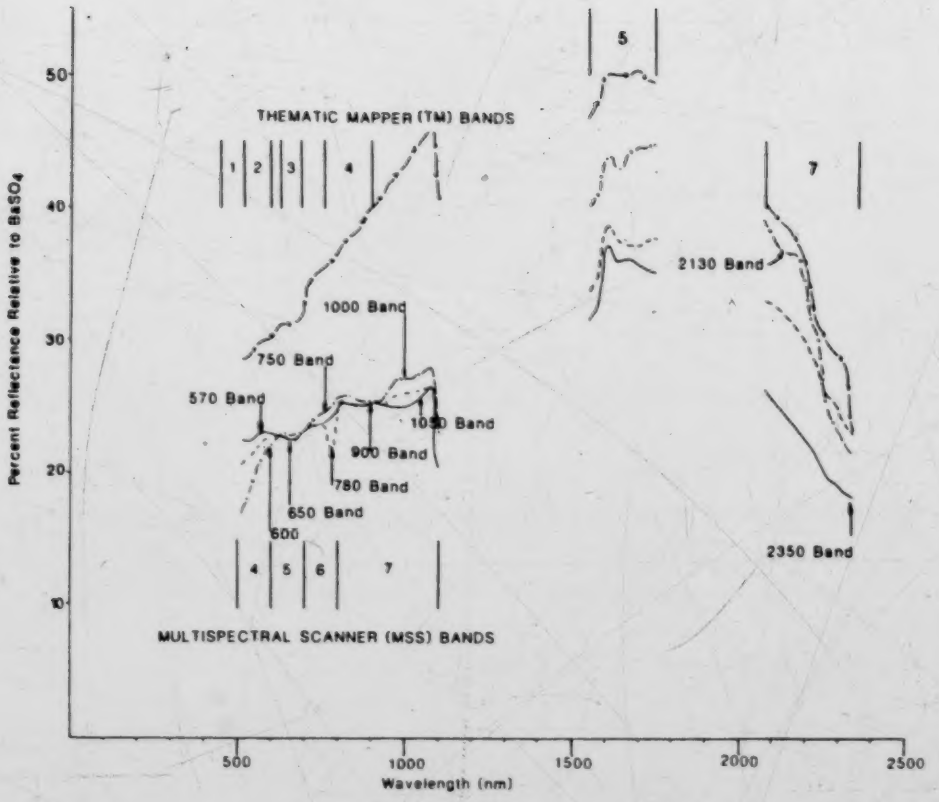

— Sample 38(16)(b) Gabbro
-·-·- Sample 72(16) Gabbro
--- Sample 63(16) Gabbro
····· Sample 38(16)(a) Gabbro

Figure 34. Spectral Reflectance Curves for Gabbros.

Sample 72(16) shows a marked increase in the near infrared portion of the spectrum (Figure 34). This is typical of vegetation (Goetz *et al.* 1983), and suggests vegetal contamination, probably due to lichen. It exemplifies the degree to which vegetation can suppress spectral features related to mineralogy.

Sheeted Dykes

Both spectra obtained from members of the sheeted dyke swarm have broad absorption bands at 650nm and 950nm, compared to the absorption bands observed in previous spectra, and a slight fall-off towards the blue part of the spectrum. The cause of the fall-off is the same as that for the gabbros, although the feature is much weaker. The sample from locality 55(17)(a) also has absorption bands at 2150nm and 2350nm. The sample from locality 55(17)(b) also has absorption bands at 2260 nm and 2250nm (Figure 35). Petrographic examination of these samples reveals abundant hornblende which accounts for their green colour in the field. Hornblende typically has broad absorption bands at 700nm and 1000nm due

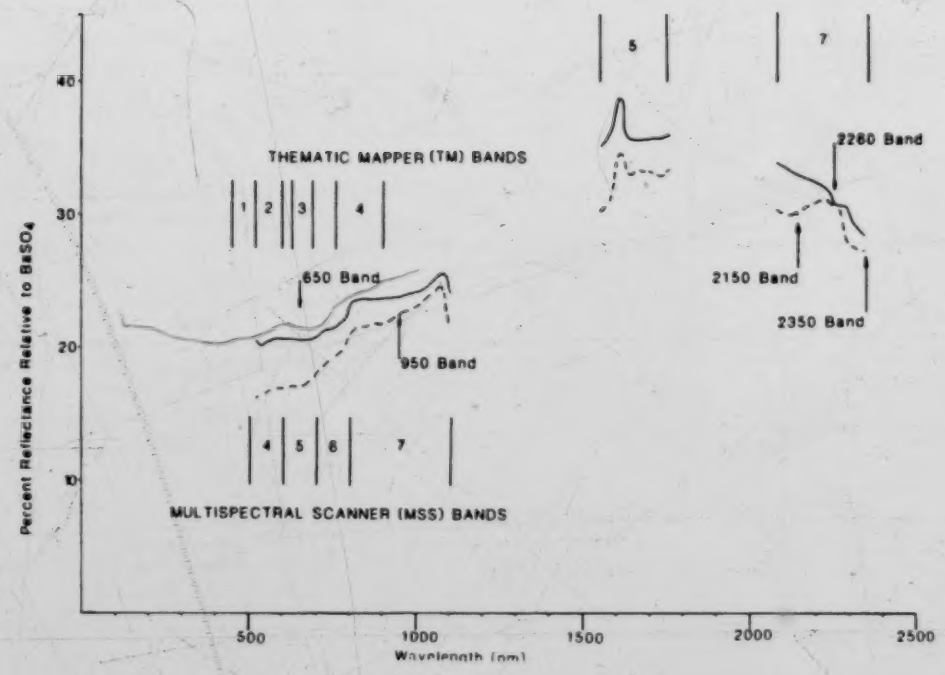

— Sample 55(17)(a) Sheeted Dyke (Diabase)
--- Sample 55(17)(b) Sheeted Dyke (Diabase)

Figure 35. Spectral Reflectance Curves for the Sheeted Dykes.

to ferrous and ferric ion (Hunt *et al.*, 1973a). The bands at 2150nm, 2260nm and 2350nm indicate Mg-OH bonding present in hornblende (Hunt *et al.*, 1973a; Hunt, 1977).

Pillow Basalts

Both spectra obtained from pillow basalt samples have a fall-off from 600nm, and three broad weak absorption bands at 700nm, 900nm and 1000nm (Figure 36). The cause of the fall-off is the same as for the gabbros. The band at 900nm can also attributed to ferric ion (Hunt *et al.*, 1970). The bands at 700nm and 1000nm can be ascribed to augite (Hunt *et al.*, 1970). Augite was confirmed petrographically.

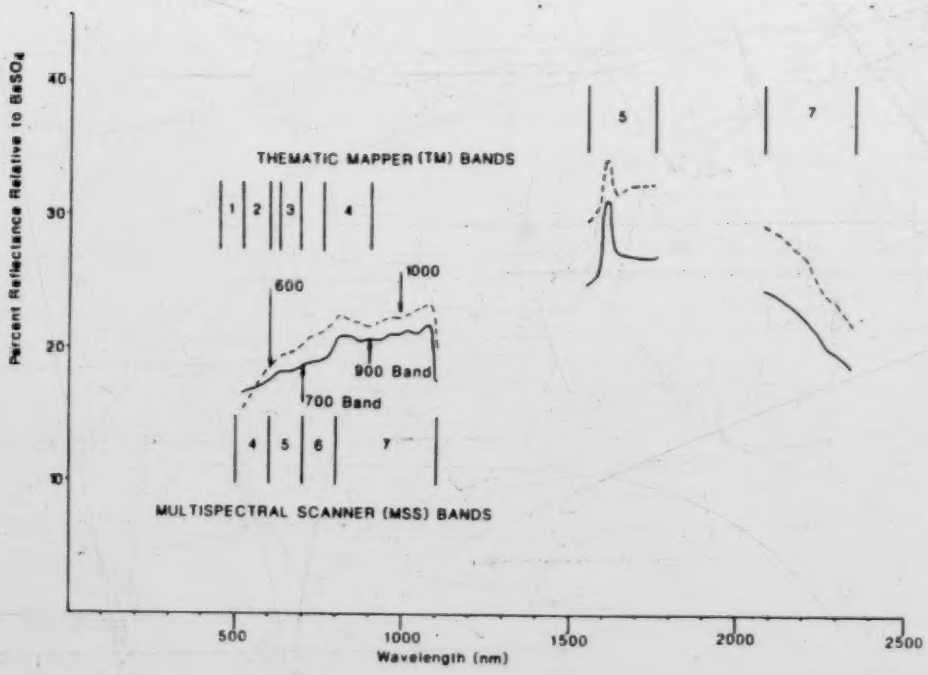

— Sample (47)(18)(a) Pillow Basalt
--- Sample (47)(18)(b) Pillow Basalt

Figure 36. Spectral Reflectance Curves for the Samples of Pillow Basalts.

B. General Features

The spectral features from the weathered surfaces of the principle rock types are similar to those observed on powdered samples (Hunt *et al.*, (1970, 1973a, 1973b, 1977,). However, the absorption phenomena are extremely muted and in some cases absent or replaced by features characteristic of the surficial weathering. Most of the spectra are characterised by a maximum reflectance at 160nm and absorption features in the 500 to 1000nm and 2100 to 2210nm regions. Maximum reflectance occurs at 1600nm since, this position is midway between the absorption features attributed to iron and to hydroxyl bonding. Most iron absorption features occur below 1600nm and most hydroxyl features occur above 1600nm. All these absorption features reflect surficial alteration of samples. The acidic rocks have the highest overall reflectance. The ultramafic rocks have a lower reflectance and greater reflectance than the basic rocks. This is in keeping with observations on powdered samples (Hunt *et al.*, 1973). It is also in keeping with field observations on the weathered surfaces (Longshaw, (1975); Hunt and Wynn, (1979); (Blom *et al.*, 1980).

Hunt *et al.* (1973), attribute the low reflectivity of the basic rocks to the abundance of opaques, which quench any spectral features and reduce the overall reflectivity of the samples. The presence of larger numbers of opaques in the basic rocks was confirmed petrographically.

C. Ground Truth Spectra

Introduction

The HHRR measures the ratio of one portion of the spectrum to another, not the absolute reflectance. The portions of the spectrum used in this study correspond to the MSS and TM bands. The position of these bands in the electromagnetic spectrum are given in Table 2. Ratioing suppresses topographic (albedo) effects, thus one type of material will have the same ratio value regardless of local variations in slope (Rowan *et al.*, 1974). This is because the ratio measures variations in the spectral reflectivity curves for any sample and not the absolute reflectance (Rowan *et al.*, 1974). However, two materials with similar spectral curves which can be distinguished by differences in brightness will appear identical on a ratioed image. Prior to discussion of the data there are salient points which should be made concerning ratio data. A ratio of 1.0 indicates equal energy in each of the two ratioed bands. Less energy in the

numerator band produces a ratio less than 1.0. Less energy in the denominator band produces a ratio greater than 1.0. A set of ratio values less than 1.0 indicates increasing spectral reflectance with increasing wavlength. A set of ratio values greater than 1.0 indicates decreasing spectral reflectance with increasing wavelength.

Basement - MSS Ratio Data

All analyses from the Basement are characterised by very similar 5/6 and 6/7 ratio values and slightly lower 4/5 values (Figure 37). Examination of the full spectra reveals absorption in Band 4 due to surficial ferric oxide stain accounting for the slightly lower 4/5 ratio (Figure 32).

The similar 5/6 and 6/7 values are of slightly less than 1.0 suggest a constant increase in the reflectance value throughout the MSS range.

Ultramafic - MSS Ratio Data

Band ratio data have been collected from powdered unaltered samples of ultramafic rocks and serpentinites (Hunt and Salisbury, 1977). They have also been collected from the weathered surfaces of ultramafic rocks in the Oman Ophiolite (Rothery and Milton, 1981; Rothery, 1984).

Hunt and Salisbury (1977), report 4/5 and 5/6 ratios slightly less than 1.0 and 6/7 ratios much greater than 1.0. These data show similar results, except that the 4/5 ratio is much lower than 1.0, and the 6/7 ratio is only slightly greater than 1.0 (Figure 38). This reduction in the 4/5 and 6/7 ratios was also observed in field ratio data obtained from the Oman Ophiolite (Rothery, 1984). The lower ratio is caused by a fall-off in reflectance in the MSS Band 4 position, due to a ferric oxide stain (Figure 33). The lower 6/7 ratio in the field samples is also caused by the strong surficial stain of the ultramafic rocks. This stain produces less absorption in the Band 7 position than either olivine or pyroxene (the characteristic ultramafic minerals in the analyses on the powdered unaltered samples). The relationship of lower 4/5 and 6/7 ratios in iron oxide relative to ultramafic rocks was observed in MSS data from S. Central Nevada. MSS ratios equivalent to those measured in the field show iron oxide has lower 4/5 and 6/7 ratios than unaltered peridotite (Rowan *et al.*, 1974). Hunt and Salisbury (1977), state from their analyses on unaltered powdered samples, that the ultramafic rocks should be easily

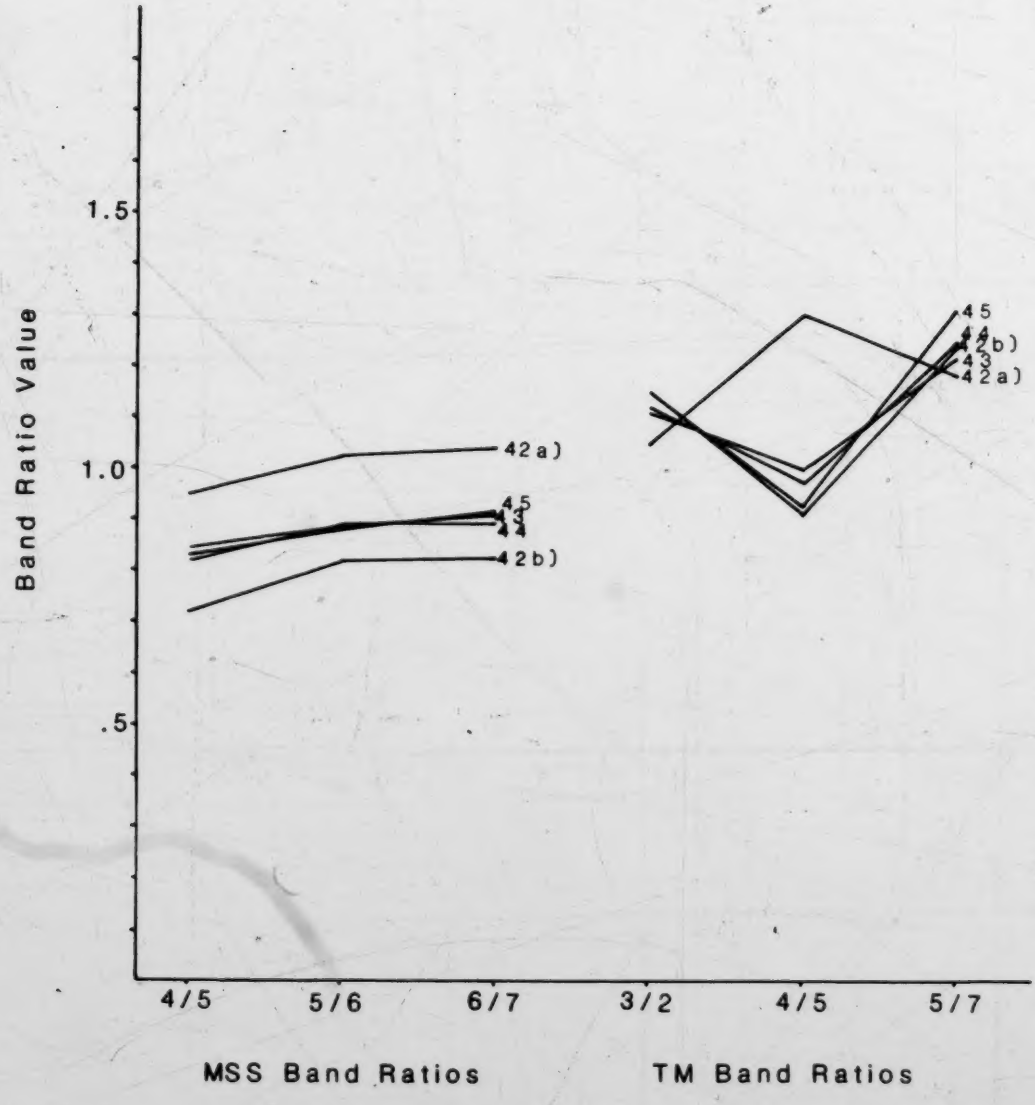

Figure 37. MSS and TM Band Ratio Field Data for the Basement.

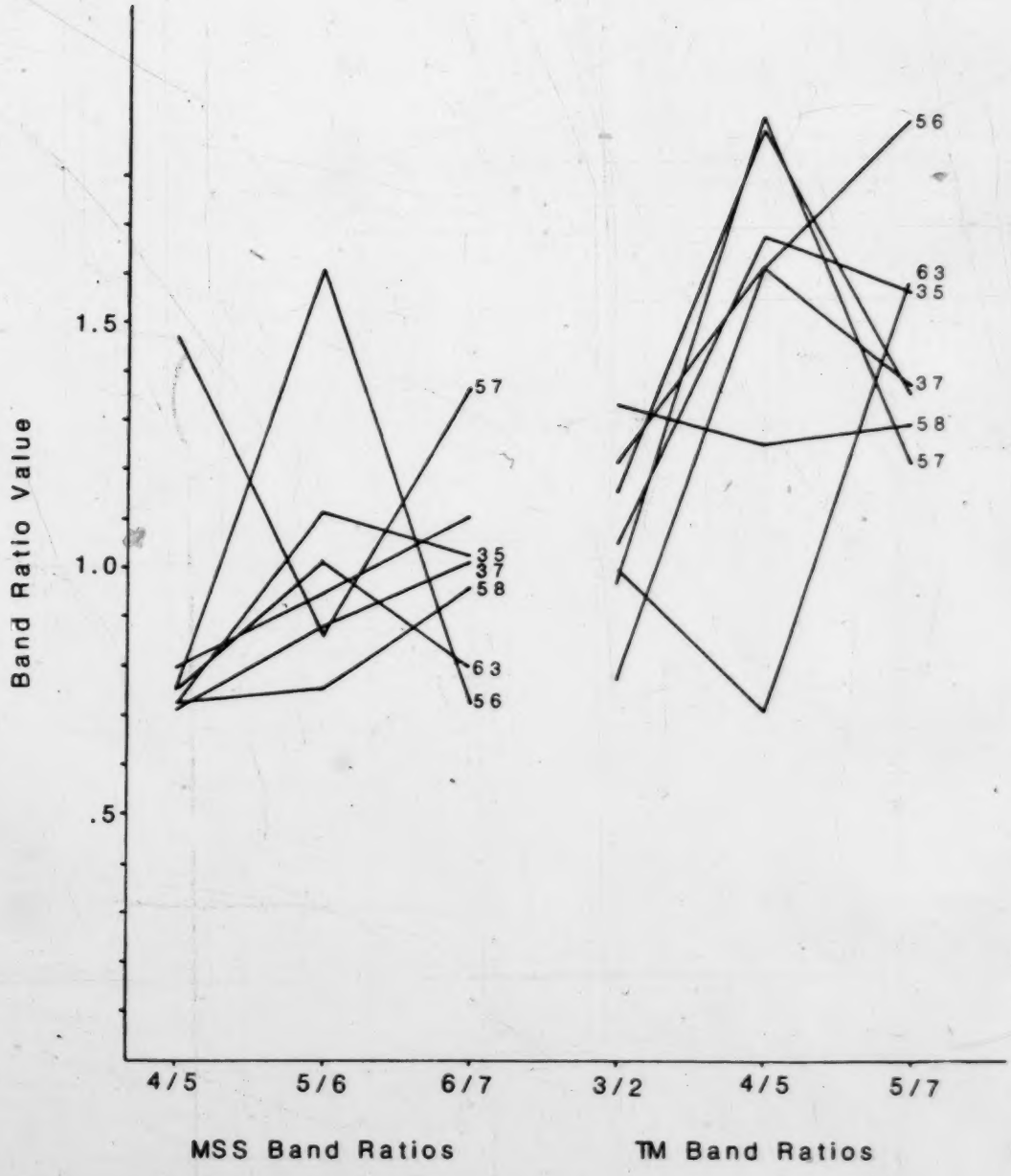

Figure 38. MSS and TM Band Ratio Field Data for the Ultramafics and Serpentinites.

distinguishable from other rocks on the basis of their very high 6/7 ratio. However, these data show the 6/7 ratio is not as diagnostic if the ultramafic rocks are altered. This was also observed in the data from the Oman Ophiolite (Rothery *et al.*, 1984).

The ratio values obtained from the serpentinites vary considerably (Figure 38). Analysis 57 has a very high 4/5 ratio, low 5/6 ratio and very high 6/7 ratio. Analyses 56 and 63 have low 4/5 ratios and high and moderately high 5/6 and 6/7 ratios respectively. Each of these analyses was obtained from serpentinite mixed with ultramafic scree, and it appears each shows features related to both the serpentites and the ultramafic rocks (or more precisely their iron stained surfaces.

Serpentinite spectra from laboratory analyses on weathered surfaces show a reflectance high at 580nm (in the Band 4 positon). This maximum was also observed in field spectra obtained on serpentinites (Botherel *et al.*, (1984). Therefore, a high 4/5 ratio is expected, as was the case with the analysis 57. The other samples have a low 4/5 ratio, which would suggest the weathered ultramafic was distributed over more of the analysed surface than the serpentinite. High 4/5 ratios were also obtained from Landsat MSS band ratio data of serpentinites in S. Central Nevada (Rowan *et al.*, 1974). Spectra from analyses of powdered weathered samples of serpentinite also have high 4/5 ratios (Hunt and Wynn, 1977). However, band ratio data from serpentinites in the Oman Ophiolite suite have low 4/5 ratios (Rothery, 1984).

Botherel *et al.* (1984), report absorption maxima at 740nm, 930nm, and 1130nm. If the absorption maxima at 740nm was more intense than the absorption maxima at 930nm the 5/6 ratio would be greater than the 6/7 ratio (eg. analyses 63 and 56). Alternatively, if the 930nm absorption maxima was more intense than the 740nm absorption maxima the 5/6 ratio would be lower than the 6/7 ratio (eg. analysis 57).

Gabbros - MSS Ratio Data

The gabbros show a large range of values in each ratio, this was also observed in analyses of powdered gabbros (Hunt and Salisbury, 1978). Except for analysis 61, all the 4/5 ratios are below 1.0 (Figure 39). The low 4/5 ratio is caused by absorption in the Band 4 position (see Figure 34). Fe-O charge transfer due to a surficial iron stain produces this absorption. All analyses have 5/6 and 6/7 ratios less than 1.0. Analyses 38 and 52 have 5/6

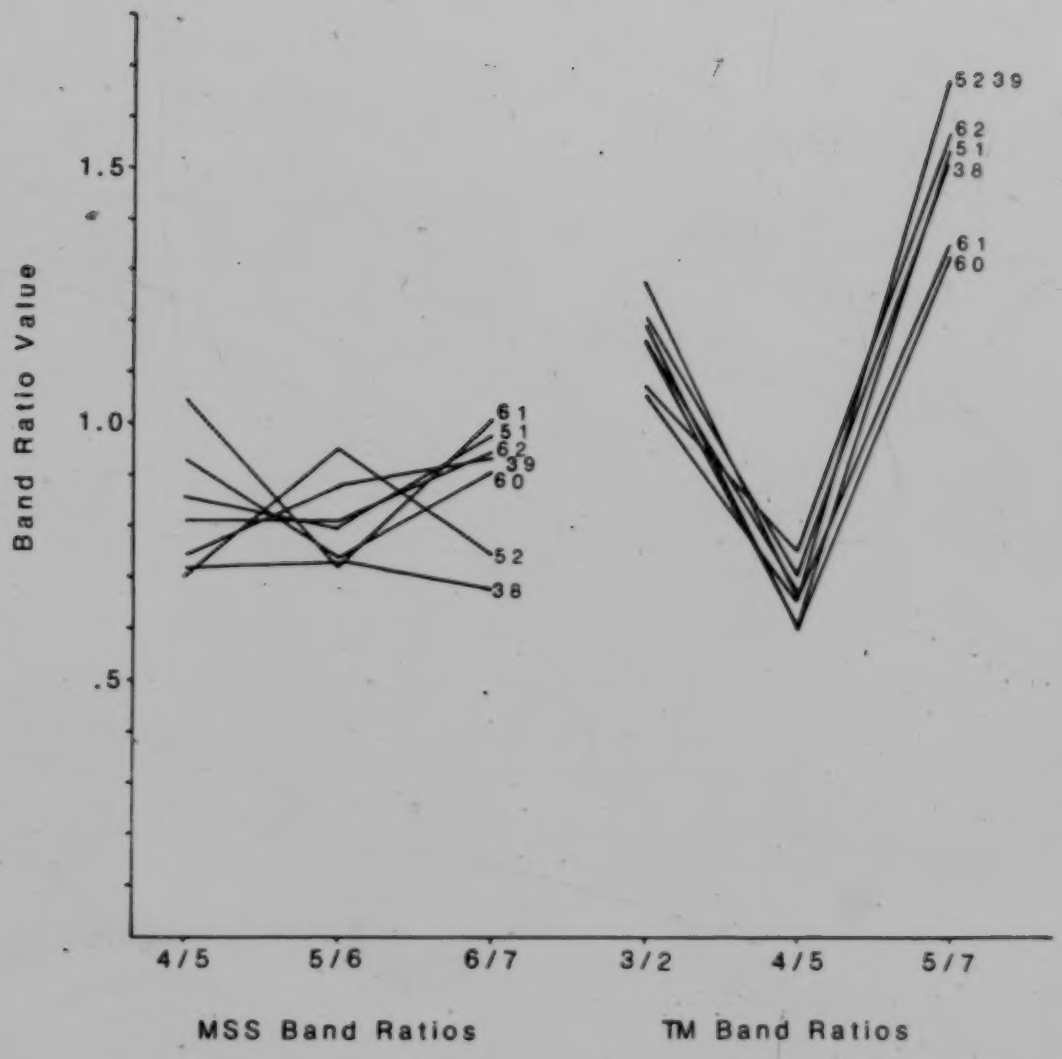

Figure 39. MSS and TM Band Ratio Field Data from the Gabbros.

ratios greater than 6/7 ratios. All other analyses have 5/6 ratios less than 6/7 ratios. Petrographic examination of a sample collected at the same time as analysis 38 reveals abundant augite which characteristically has absorption bands at 770nm and 1100nm (Hunt and Salisbury, 1978). However, the 770nm absorption, (in the band 6 position) is more intense than the 1100nm absorption (in the Band 7 position) (Figure 34). This causes the 5/6 ratio to be relatively higher than the 6/7 ratio, as was the case with analyses from locality 38 and 52. The reverse would occur if surficial iron oxides, or greater quantities of olivine and pyroxene over augite were present, for the maximum absorption would occur in the Band 7 position. Either of these reversal causes can be used to explain the analyses with low 5/6 ratios relative to 6/7 ratios. Hunt and Salisbury (1978) and Rothery (1984), also observed lower 5/6 ratios than 6/7 ratios. One further cause of a lower 5/6 ratios relative to 6/7 ratio, would be vegetal contamination, for the cellular structure of vegetation causes a rapid increase in reflectance in the band 6 position, which flattens off in the Band 7 position (Goetz *et al.*, 1983). This would result in a low 5/6 ratio and high 6/7 ratio, although an extreme difference would be expected if vegetation was indeed the cause.

Sheeted Dykes - MSS Ratio Data

All analyses have 4/5 ratios slightly less than 1.0, and except for analyses 71 and 53, 5/6 ratios less than 6/7 ratios (Figure 40). The low 4/5 ratio probably results from a minor ferric oxide stain causing absorption in the Band 4 position due to Fe-O charge transfer.

Petrographic examination of samples collected at the same time as the analyses reveals abundant hornblende, which accounts for their green appearance in the field. Hornblende has twin absorption bands in the 600nm to 1000nm region (Hunt and Salisbury, 1970). The shorter wavelength absorption (in the band 6 position) is stronger than the longer wavelength absorption (in the band 7 position). This produces the high 5/6 ratio relative to the 6/7 ratio, seen in these data. Analyses 53 and 71 show the reverse. Possible causes for this are forwarded in the discussion of the data for the gabbros. In contrast, a low 5/6 ratio relative to the 6/7 ratio was observed in analyses from other diabases and sheeted dykes (Hunt and Salisbury, 1978; Rothery, 1984). However, the reverse was observed in samples which were very altered (Hunt and Salisbury, 1978). Hornblende appears to be an alteration mineral in these rocks.

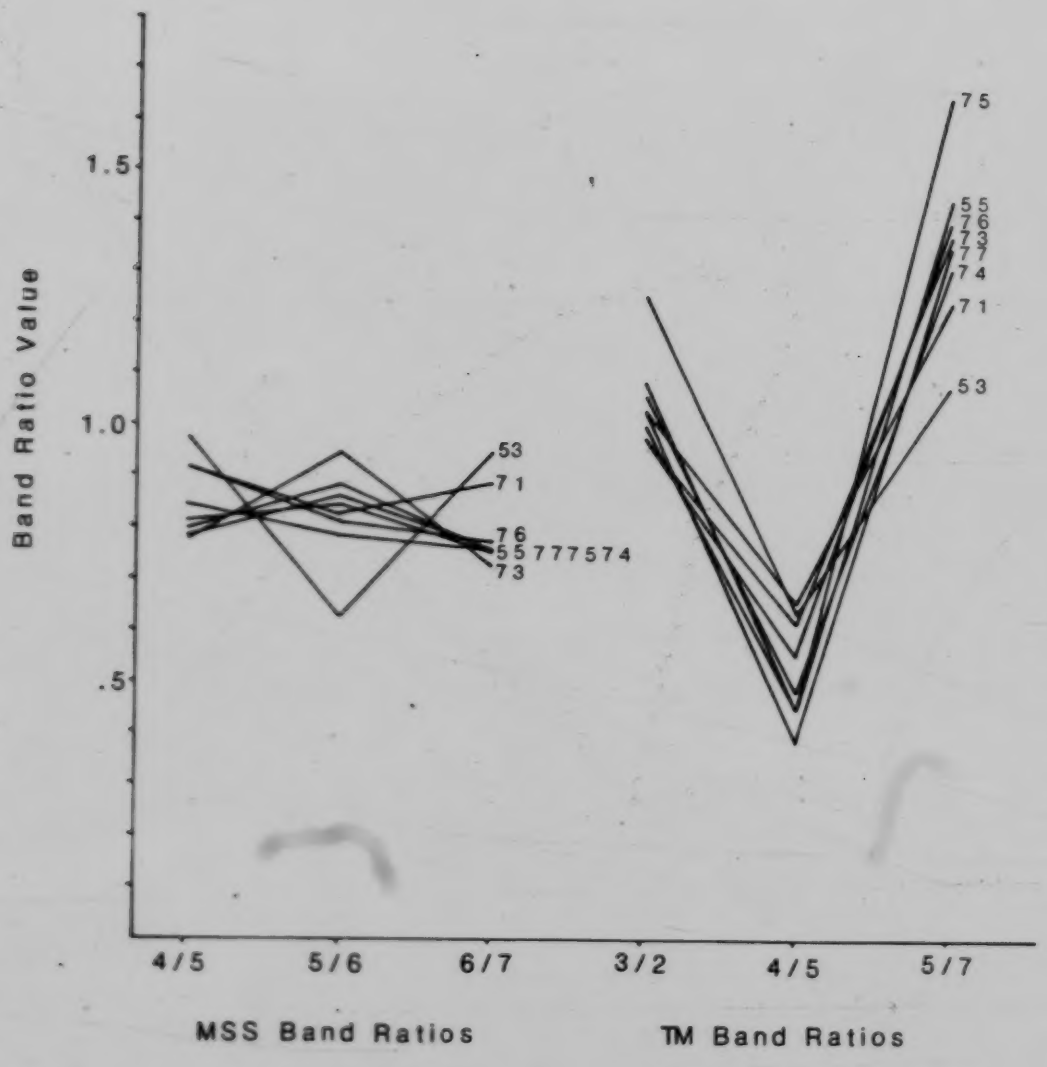

Figure 40. MSS and TM Field Ratio Data from the Sheeted Dykes.

Pillow Basalts - MSS Ratio Data

All analyses show 4/5 ratios less than 1.0 (Figure 41). However, there is considerable variation which probably reflects different distributions of ferric oxide over the analysed area. Except for the analysis 47a the 5/6 ratios are lower than the 6/7 ratios. This probably results from absorption in the Band 7 position due iron oxide or possibly to olivine and pyroxene. The high 5/6 relative to 6/7 of analysis 47a may result from abundant augite (see previous discussion). Augite was confirmed petrographically in a sample obtained at the same time as analysis 47a.

Summary of MSS Ratio Data from Analyses of the Ophiolite and Basement.

It is clear from the summary graphs of the MSS field ratio data that considerable overlaps exist between the same ratio in different units (Figure 42). However, discrimination of the ultramafic rocks should be possible from all other rock types except the limonite samples by their 4/5 and 6/7 ratios. These have the same spectral response to the ultramafic rocks, since the weathered surfaces of the ultramafic rocks are characterised by iron oxide. Discrimination of serpentinization should also be possible, especially in the ultramafic rocks, using the higher 4/5 and lower 6/7 ratios of the serpentinite.

Basement - TM Ratio Data

Except for analysis 42a, all the analyses have 3/2 ratios between 1.1 and 1.5, 4/5 ratios between 0.9 and 1.0 and 5/7 ratios between 1.2 and 1.3 (Figure 37).

The high 3/2 ratio results from absorption in Band 2 due to Fe-O charge transfer from ferric oxide staining (Figure 32). The low 4/5 results from maximum reflectance occurring in the Band 5 position (Figure 32). The high 5/7 ratio is caused by absorption in the Band 7 position (Figure 32). The absorption is caused by clays replacing weathered feldspar. The high 4/5 ratios of analysis 42a probably reflects vegetation contamination, increasing the reflectance in Band 4 and decreasing the reflectance in Band 5.

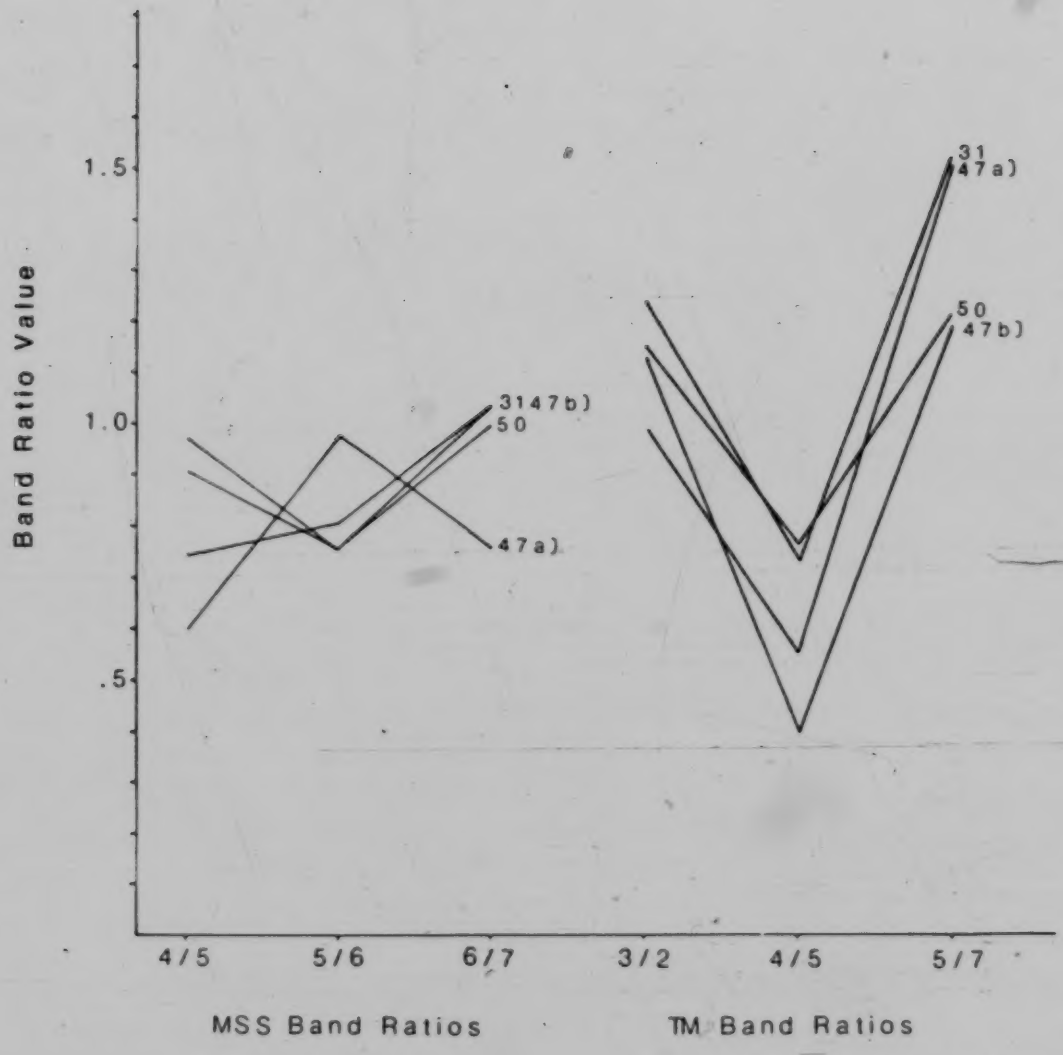

Figure 41. MSS and TM Ratio Field Data from the Pillow Basalts.

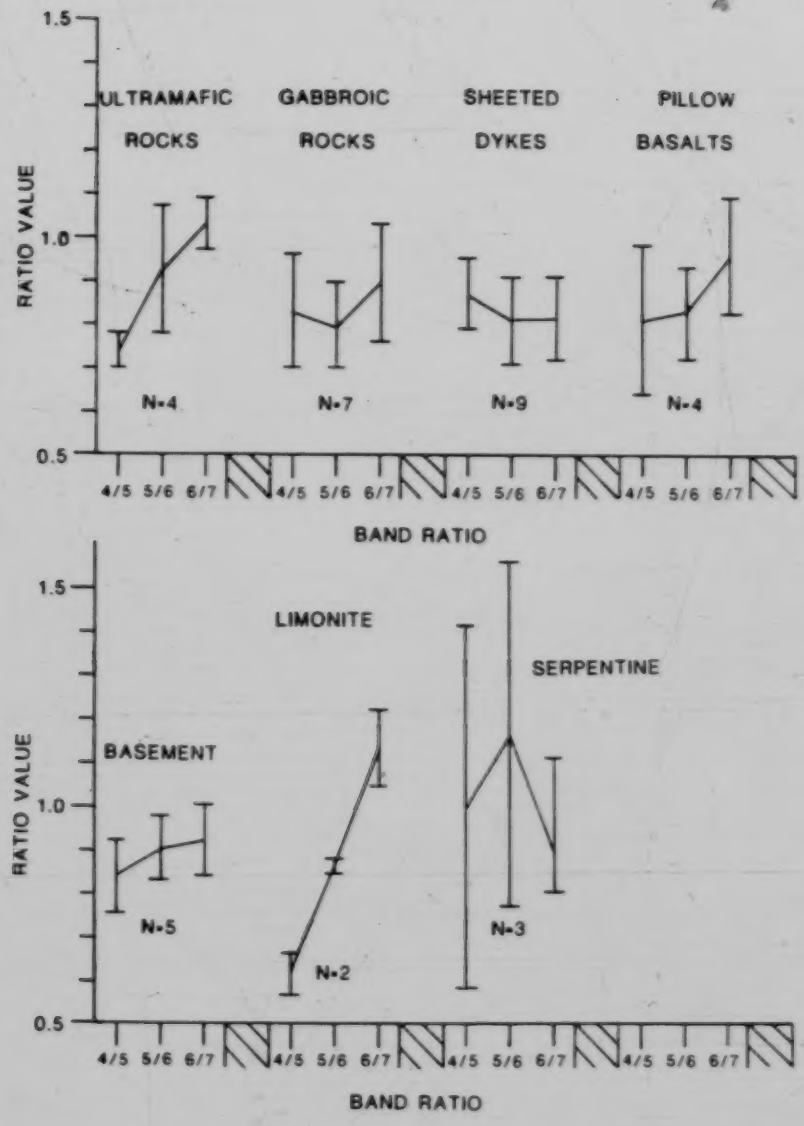

Figure 42. Mean and Mean Values ± 1 standard deviation for the MSS Field Ratio Data.

Ultramafics and Serpentinites - TM Ratio Data

All the analyses of ultramafic rocks have high values in the three band ratios (greater than 1.0) (Figure 37). Therefore, the denominator band is always less than the numerator band. The 3/2 ratio is the lowest of the three ratios, the 4/5 ratio the highest and the 5/7 intermediary between these.

The 3/2 greater than 1.0 results from a low value in Band 2 caused by Fe-O charge transfer at 500nm to shorter wavelengths (Figure 33). This attests to the strong ferric-oxide stain on the surface of the samples.

The very high 4/5 ratio is restricted to ultramafic rocks, in fact these are the only rocks with a ratio greater than 1.0. Examination of the spectra obtained from the ultramafic rocks would indicate that this ratio would be higher than that obtained from the other units, but still be less than 1.0. This is because the maximum reflectance occurs in the Band 5 position (Figure 33). This is further supported by the spectra presented from powdered unaltered specimens of ultramafic rocks (Hunt *et al.*, 1974), and from the weathered surfaces of the serpentinized harzburgites (Blom *et al.*, 1980). However, spectra from the natural surfaces of serpentinized harzburgites may have their maximum reflectance at 700nm (Band 3) if the 1000nm absorption band is well defined (Hunt and Wynn, 1979). This would result in a high 4/5 ratio. The 1000nm band was not particularly well developed here and it is not inconcievable that a shift in the position of the maximum reflectance could occur with stronger development of this band. Hunt and Wynn (1979), also present spectra from the natural surfaces of serpentinized dunites, in which the reflectance in Band 5 is much greater than Band 4, therefore, these should have lower 4/5 ratio values than the serpentinized harzburgites.

The relatively high 5/7 ratio in both the ultramafic rocks and the gabbros results from a low value in Band 7 caused by absorption due to Mg-OH bonding (Figures 37 and 38). The Mg-OH bonds are present in serpentine from serpentinization of these rocks. Three sets of ratios were obtained from serpentinized scree, consisting of a mixture of serpentine and weathered ultramafic rock. Examination of the full spectra for serpentinite indicates it should have a low 3/2 ratio, low 4/5 ratio, and high 5/7 ratio. This was observed in analysis 63, but not analyses 56 and 5/7. Analyses 56 and 57 show the characteristics of both serpentinite and ultramafic rocks. Clearly, more analyses are required from serpentinite in order to determine its 'typical' spectral signature, especially since serpentinite can be economically significant. The

low 3/2 ratio of serpentinite results from a reflectance high in the band 2 position. The low 4/5 ratio is caused by maximum reflectance occurring in the band 5 position, and the high 5/7 ratio results from absorption in the band 7 position due to Mg-OH bonding. The relatively higher 5/7 ratio of analysis 56 may reflect a greater distribution of serpentine over the analysed area than in the other serpentine samples and ultramafic rocks. If the serpentinization was distributed evenly in all the analyses of serpentinite variations in the the 5/7 ratio may reflect the relative degree of serpentinization. In which case the 5/7 ratio might be used to establish relative degrees of serpentinization.

Gabbros - TM Ratio Data

The gabbros analysed during this study have 3/2 and 5/7 ratios greater than 1.0 and 4/5 ratios less than 1.0 (Figure 39). The high 3/2 is attributed to absorption in Band 2 (Figure 34). This is caused by Fe-O charge transfer, due to a surficial iron oxide stain. Fe-O charge transfer due to a surficial iron oxide stain was observed in other analyses of the weathered surfaces of gabbros (Longshaw, 1975; Blom *et al.*, 1980). The 3/2 ratio is very similar to that observed for the ultramafic rocks, even though the gabbros have very minor surficial iron oxide alteration compared to the ultramafic rocks. This confirms that provided the distribution of iron oxide is uniform over the area. The absorption is not related to the relative amounts of iron oxide present (Hunt and Salisbury, 1978). The 4/5 ratio is very low, this results from maximum reflectance occurring in the Band 5 position (Figure 34). The maximum reflectance occurs in Band 5, for this lies midway between the absorption bands resulting from iron oxide at shorter wavelengths and the hydroxyl molecule at longer wavelengths (Figure 34). The very high 5/7 ratio indicates Mg-OH bonding present in serpentine.

Sheeted Dykes - TM Ratio Data

The ratios for the sheeted dykes are very similar to those observed for the gabbros. However, there is a greater spread of the data (Figure 40). The 3/2 ratio is slightly greater than 1.0, possibly due to absorption in the Band 2 band position by Fe-O charge transfer in surficial iron oxide staining . Weak absorption in the Band 2 postion was observed in the spectra obtained from these rocks (Figure 35). The 4/5 ratio is very low, as there is absorption in the Band 4 due to iron oxide. Maximum reflectance occurs in the Band 5 position. The high 5/7

ratio of the sheeted dykes and pillow basalts again results from Mg-OH bonding. However, the Mg-OH bond is present in amphibole (hornblende) as to opposed to serpentine or augite as was the case in the ultramafic rocks and gabbros.

Pillow Basalts - TM Ratio Data

The ratios observed for the pillow basalts are very similar to those of the gabbros and sheeted dykes (Figures 39, 40 and 41). The causes of the high 3/2 and low 4/5 ratios are the same as those used to explain similar values in the gabbros. The high 5/7 ratio must result from absorption due to Mg-OH bonding, probably in hornblende. However, no absorption was observed in this position in the full spectra from these rocks.

Summary of TM Ratio Data from Analyses of Ophiolite and Basement

Examination of the mean 4/5 ratio ± 1 standard deviation from the previous localities reveals that the ultramafic rocks can be easily distinguished by their high positive value (Figure 43). The mean 3/2 ratio from the ultramafic rocks is also higher than that obtained from the other units and probably reflects a more even distribution of ferric oxide over the analysed area (Figure 42). The mean ratio values ± 1 standard deviation from the gabbros, sheeted dykes, and pillow basalts are very similar. However the gabbros have slightly higher 3/2, 4/5 and 5/7 ratios than the sheeted dykes and pillow basalts, which should allow their discrimination. The ratio values from the sheeted dykes and pillow basalts are very similar and complete discrimination does not appear possible using these ratios. Only three analyses of serpentinites were obtained and there is substantial difference between these. Nontheless, they should be easily distinguished from the other members by their much lower 3/2 ratio and much higher 5/7 ratio. The low 3/2 ratio is caused by a reflectance high in the band 2 position as opposed to an absorption band due to surficial iron-oxide in the other rock types. The low 3/2 is caused by the absence of iron oxide absorption in the Band 2 position and the high 5/7 is caused by strong Mg-OH absorption in the Band 7 position.

The Basement can be discriminated by its 4/5 ratio and 5/7 ratio relative to its surroundings.

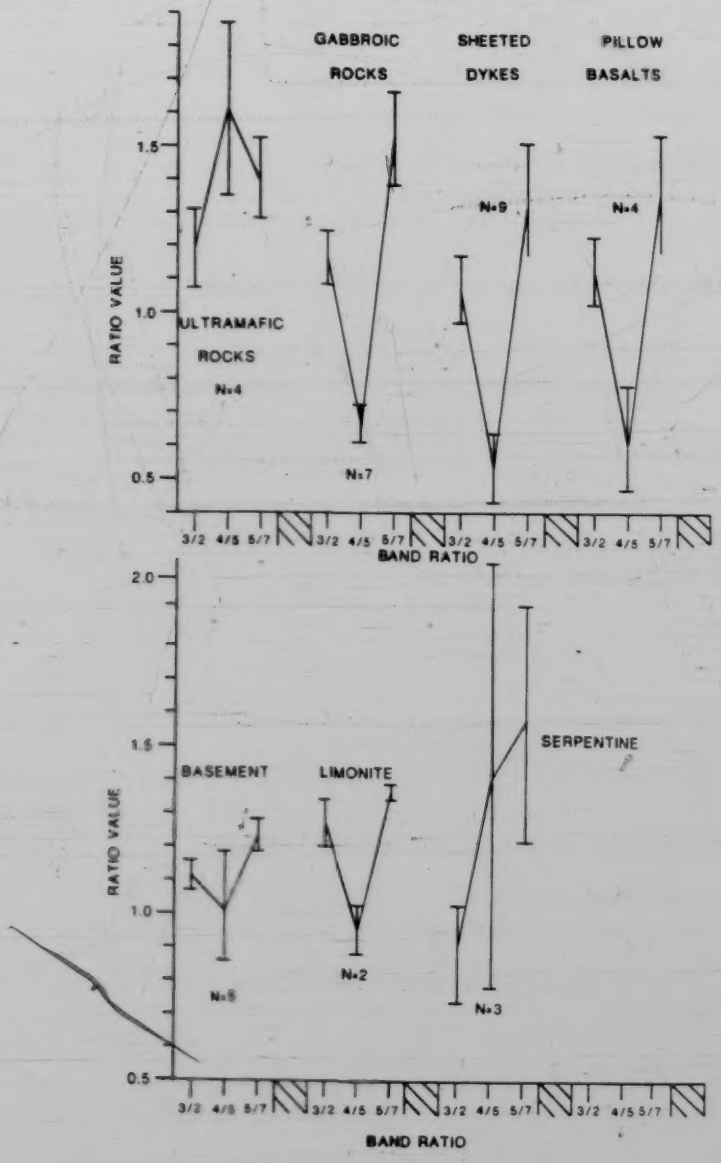

Figure 43. Mean and Mean Value ± 1 standard deviation for the TM Field Ratio Data.

V. Image Analysis

A. Introduction

Most previous geological studies were carried out in arid or semi-arid environments. These represent ideal conditions for geological interpretation of remote sensing data because of the lack of vegetation, high sun angle, and maximum rock exposure. In contrast, this study was undertaken in a northern maritime environment which is less suitable for geological interpretation but more realistic if these data are to be used in Canada.

Image analysis involves comparison of geological maps with Landsat MSS and TM data to ascertain which spectral bands, in conjunction with various image enhancement techniques, are most useful for rock type discrimination.

The MSS scene (ID= 4008714092) was collected by Landsat 4 on the 12th of October 1982. The cente of the scene is located on orbit path 005, image row 026 - World Reference System (WRS) Landsat 4 Index Map. The scene covers the Bay of Islands area Western Newfoundland, (Study Area A, Figure 1). The geology of the Bay of Islands study area is given in Figures 3a, b and c.

The TM scene was collected by Landsat 4 on the 25th of September 1982. Its centre is located on orbit path 005 image row 024 - WRS Landsat 4 Index Map. The image covers the Hare Bay Area N. Western Nfld., (Study Area B, Figure 1) The geology of the Hare Bay study area is given in Figure 4.

A regional interpretation of the Bay of Islands study area was made from a composite of bands 4, 5 and 7 displayed as blue, green and red respectively, to determine the most suitable areas for detailed analysis with MSS digital data. Bands 4, 5 and 7 record information from the visible green, visible red and reflected near infrared parts of the spectrum respectively. When these bands are assigned in the above manner the image is similar to a colour infrared photograph and is therefore referred to as a "colour infrared composite". The four massifs of the Bay of Islands Complex were chosen for detailed analysis due to of their relatively sparse vegetation cover and varied lithologies (Figure 3).

The TM data were used for a detailed interpretation of the White Hills Peridotite in the Hare Bay study area (Figure 4). The White Hills Peridotite is lithologically similar to the ultramafic part of the Bay of Islands Complex.

Image analysis was performed on a DIPIX ARIES II Image Analysis System. Prior to to the visual or manual comparison of imagery with geological maps, the following image analysis techniques were used:

1. Geometric Correction
2. Compositing and Contrast Stretching
3. Band Ratioing
4. Atmospheric Correction
5. Supervised Classification

B. Image Analysis Techniques

Geometric Correction

The MSS scans perpendicular to the northeast to southwest orbital path of the satellite. This orbital path combined with the eastward rotation of the earth beneath the satellite during imaging, causes each sweep of the scanner to view an area slightly west of the previous sweep. To compensate for this skewness each scan line is shifted horizontally with respect to the previous scan line and the resultant image is in the form of a parallelogram. Correction of this geometric distortion to the UTM coordinate system is made using ground control points (GCP's) which can be accurately located on both the Landsat image and corresponding NTS map. The UTM coordinates of the GCP's are used to calculate a first order affine transformation, the coefficients of which are applied to each spectral band (Moik, 1980). The image was then resampled by cubic convolution to a pixel size of 50m x 50m (Bernstein and Ferneyhough, 1975; Moik, 1980).

Compositing and Contrast Stretching

Compositing (colour additive viewing) is a technique for combining the information in three spectral bands. Each band is displayed as either red, green or blue. The brightness of each colour corresponds to the level of reflectance in a band. Therefore, an area with a high reflectance in the bands displayed as red and green and a low reflectance in the band displayed as blue would appear yellow on the resultant composite image.

Contrast stretching involves stretching the data such that they cover the full range of the system. The MSS system is designed to respond to a large range in scene brightness caused by changing illumination as the satellite orbits the globe. Often, any one image will tend to cover a very small portion of the full dynamic range of the system, resulting in a relatively low contrast image. Therefore, it is desirable to "stretch" the data so that they cover the full range of the system to produce a maximum contrast image. This involves plotting a histogram of the digital number (DN) values in a particular band and determining the minimum and maximum values of the data. These values are assigned 0 and 255 respectively and a linear stretch applied to the remaining data between these two values. A non-linear stretch may be applied in order to enhance one portion of the data with respect to another. All the data presented here have been linearly stretched.

Ratioing

Ratioing involves division of one spectral band by another, pixel by pixel, to produce a ratio image. Bands used for ratioing were not stretched prior to ratioing. However, the resultant ratio data were stretched to enhance the portion of interest. A ratio image displays differences in the spectral reflectivity curves of the underlying materials, thereby reducing brightness variations caused by different slope orientations (Rowan *et al.*, 1974; Rowan *et al.*, 1977) For example, a steep slope facing the sun should appear brighter than a slope facing away from the sun on a single or multiband image, provided the slopes are composed of the same material. However, if both slopes consist of the same material, their spectral curves should be similar and they should have similar values on a ratio image. Unfortunately, two rock types with similar spectral curves which can be distinguished by different brightness levels will be indistinguishable on a band ratio image.

Atmospheric Correction

The importance of atmospheric effects varies with both wavelength and with the image enhancement techniques used. Maximum atmospheric effects (backscattering) occur in the shorter wavelength bands, (bands 4 and 5). These effects are often negligible in single band or multiband composite imagery, and no atmospheric correction was applied to such imagery.

However, these bands were corrected when used for ratioing since:

$$\frac{A+e_1}{B+e_2} \neq \frac{A}{B}$$

where e_1 and e_2 are the additive, atmospheric scattering components in bands A and B (Rowan *et. al.*,1974).

The correction involved finding the minimum value in each band and subtracting this value from each pixel. The minimum value occurred over water in these data. Bands 6 and 7 were not corrected for the minimum value was zero, indicating that a correction was not necessary.

Classification

The classification adopted was a semi-automated technique which classified features with distinct spectral ranges. The minimum and maximum values of the feature of interest were assigned to a theme, each pixel was then classified, by means of a parallelepiped classifier (Moik, 1980), as to whether or not it belonged to that theme. In this study, the classification was used for semi-automated mapping of distinct rock types over large areas.

C. MSS Data Interpretation

Regional Study

Plates 1 is a colour-infrared (CIR) composite for most of the MSS scene. A CIR composite consists of bands 4, 5 and 7 displayed as blue, green and red respectively. White areas on the CIR composite were interpreted to be snow covered.

Plate 1, extends from Bakers Brook in the north to St. Davids in the south. The Precambrian Basement, which forms the Long Range Mountains in the north and the Southern Long Range Mountains in the south is distinguished by its light pink colour and strongly dissected nature (Plate 1, Figure 2).

The contact between the transported clastic sediments of the Humber Arm Allochthon, coloured green/brown, and the autochthonous Ordovician carbonates, coloured red, is also apparent (Plate 1, Figure 2). This colour difference is caused by a change in vegetation from an open woody marsh to dense forest. The forest has a strong response in band 7, displayed as

red compared to the woody marsh. The vegetation change results from a drainage change between the poorly drained clastic sediments and the well drained carbonate sediments.

Table Mountain, North Arm Mountain, Blow Me Down Mountain and the Lewis Hills of the Bay of Islands Ophiolte Complex are also discernible in the western part of the image by their less dissected nature and cyan rim (Plate 1, Figures 2, 3, 3a, b, c). Areas devoid of vegetation appear cyan on the image as they have a relatively strong response in the green and red displayed as blue and green respectively, and a relatively weak response in the near-infrared displayed as red. Within the massifs of the Bay of Islands Ophiolite Complex, the cyan area correspond mainly to outcrops of ultramafic rocks (Figures 3a, b and c). Highways, built up areas and bare soil areas are also cyan due to their lack of vegetation cover.

Detailed Interpretation of the Four Massifs of the Bay of Islands Assemblage

The four massifs of the Bay of Islands Assemblage are from north to south : Table Mountain, North Arm Mountain, Blow Me Down Mountain and the Lewis Hills (Figure 3). They consist of four main rock types: ultramafic rocks, gabbroic rocks, sheeted dykes and pillow basalts (Figures 3a, 3b and 3c).

The mean and standard deviation were calculated for a set of pixels in each band from each of the rock types (Table 3). These data show that there is a partial overlap of the ultramafic rocks and other rock types, in bands 4, 5 and 7 and complete overlap in band 6. This suggests that partial discrimination of the ultramafic rocks from the other rock types should be possible using bands 4, 5 and 7 but not band 6. Band 5 should allow maximum separation. However, because of problems associated with illumination angle discussed earlier, band ratios should provide the best separation.

Previous investigators found that a combination of the band ratios 4/5, 5/6 and 6/7 was most suited to lithlogical discrimination and recognition of limonite alteration zones (Rowan *et al.*, 1974; Rowan *et al.*, 1977). These workers noted limonite had a lower 4/5 ratio and higher 6/7 ratio than other lithologies. Field examination of the ultramafic rocks in this area revealed they had a strong limonite coat which should allow their separation. Laboratory spectra and ground truth spectra indicated the ultramafics should have low 4/5 ratios and high 6/7 ratios (Figures 33 and 38). These figures also indicated substantial overlap between the band ratios of the other units, suggesting that discrimination of these units would be extremely

difficult. However, the field data did indicate that discrimination of serpentinite shear zones within the ultramafic rocks should be possible, due to of the high 4/5 and low 6/7 ratios of the serpentinites compared to the low 4/5 and high 6/7 ratio of the ultramafic rocks.

Five atmospherically uncorrected ratios were calculated, namely : 4/5, 4/6, 5/6, 5/7 and 6/7. When the ratio of two bands is determined, the resultant values tend to cover a very small range. Furthermore, if these numbers are to be stored on the DIPIX system they have to be converted to integers, which decreases variation within the range. This was avoided by scaling the ratios to give a mean ratio value of 128 and a standard deviation of three. The mean and standard deviation for a set of pixels from each rock type for each ratio was calculated (Table 3). These data indicate there is minimum overlap of mean ratio values, at the one sigma level, of the ultramafic pixels with pixels from the other rock types in the 4/5, 5/6 and 6/7 ratios. This suggests that these three ratios should be most suitable for visual separation of the

Table 3. Mean values ± one standard deviation for a set of pixels from various rock types in the MSS bands and several band ratios.

Band	Ultramafic Rocks N=62	Gabbroic Rocks N=63	Sheeted Dykes N=39	Pillow Basalts N=63
4	38.94±5.36	27.78±5.18	25.12±2.54	24.95±2.92
5	39.42±5.90	22.41±5.50	18.77±3.74	16.89±3.91
6	52.00±8.27	51.43±9.04	52.72±11.77	46.54±12.54
7	19.23±3.77	22.98±4.06	24.41±5.64	20.95±6.07
Band Ratio				
4/5	104.52±6.84	116.92±12.88	126.28±21.47	128.11±15.60
4/6	118.37±3.61	116.29±3.03	117.31±3.44	116.35±3.16
5/6	124.10±3.88	116.78±3.57	116.31±2.46	115.00±2.68
5/7	149.97±9.34	114.00±17.83	101.51±15.77	105.49±11.64
6/7	139.65±10.86	123.57±8.53	120.23±6.89	123.65±8.59

ultramafic rocks from the other rock types. These data also confirm the low 4/5 and high 6/7 ratios of the limonitic coat of the ultramafic rocks observed in the field. Plate 2 is a 4/5, 5/6, 6/7 band ratio composite of North Arm Mountain with each ratio displayed as blue, green and red respectively. The band ratios have been stretched in order to expand the DN range containing the rock types of interest over the full range of the system (Table 4)

Comparison of the geological maps with the imagery confirms that the ultramafic rocks, coloured yellow on the imagery, can be distinguished using the the 4/5, 5/6, 6/7 band ratio composite (Plate 4, Figure 3a). The yellow appearance of the ultramafic rocks is caused by their high values in the 5/6 and 6/7 ratios, displayed as green and red, which combine to give yellow. However, careful comparison of the CIR composite with the ratio imagery reveals some of the yellow area was interpreted as snow on the CIR composite. This illustrates how two materials, which can be separated by different brightness levels on a CIR composite, are inseparable on an atmospherically uncorrected band ratio composite due to the similarity of their spectral curves. This indicates the need to refer to a CIR composite when interpreting band ratio data. Furthermore, careful scrutinization of the CIR and band ratio composites shows all the blue areas on the CIR composite appear yellow on the band ratio composite. However, not all the blue areas are ultramafic rock. By analogy, not all the yellow areas are ultramafic rock, indicating there is some overlap in the band ratio values of ultramafic rock outcrops and other rock outcrops. Lack of separation of non-ultramafic rock outcrops and snow, from the ultramafic rock outcrops is caused by the high 5/6 and 6/7 ratio values which overwhelm any differences in the 4/5 ratio. This is especially important in the atmospherically uncorrected 4/5 ratio as the spectral information of interest is at the low end of the DN range.

Plate 3 is a 4/5, 5/6, 6/7 stretched band ratio composite of North Arm Mountain in which bands 4 and 5 were atmospherically corrected prior to ratioing. The atmospherically corrected ratios were stretched to expand the DN range of interest over the full range of the system (Table 4). Comparison of atmospherically corrected band ratio composite with the CIR composite indicates areas covered with snow and non-ultramafic rock outcrops can be distinguished from the ultramafic rocks (Plate 1 and 5, Figure 3a). Recent workers had concluded that an atmospheric correction did not improve the data for it decreased the signal to noise ratio (Rowan and Lanthram, 1980; Conradsen and Harpøth, 1984). However, an atmospheric correction improved discrimination on these band ratio composites.

Table 4. Operator stretches applied to band ratio imagery.

Band Ratio	North Arm Mountain No Atm. Corr. Stretch	North Arm Mountain Atm. Corr. Stretch	Blow Me Down Mountain Atm. Corr. Stretch	Lewis Hills Atm. Corr Stretch
4/5	87-150	100-130	100-140	105-140
5/6	110-135	100-130	100-160	105-140
6/7	110-160	110-155	100-185	110-160

Plates 4 and 5 are atmospherically corrected, operator stretched , band ratio composites for Blow Me Down Mountain and the Lewis Hills. Again the ratios were stretched to expand the DN range of interest over the full range of the system (Table 4). Comparison with the geological maps and CIR composites substantiates that with an atmospheric correction areas interpreted as ultramafic rocks can be separated from areas interpreted as snow and other rock outcrops (Plates 1, 4 and 5, Figures 3b and 3c). The atmospherically corrected, band ratio composite of Blow Me Down Mountain suggests more of the mountain could be interpreted as partially snow covered than interpretation of the CIR composite indicated (Plates 1 and 4, Figure 3b). The increased interpretation of snow on the band ratio composite compared to the CIR composite may result from ratioing enhancing partially snow covered pixels (Plates 1 and 4). However, there are several other possible reasons why the ultramafic rocks did not appear yellow and these are given at the end of the classification section.

In all three atmospherically corrected, band ratio composites, yellow areas outside the known areas of ultramafic rock may represent unmapped ultramafic rocks or limonite.

The field ratio data suggested discrimination of serpentinite within the ultramafic rocks should be possible due to its high 4/5 and low 6/7 ratio compared with the low 4/5 and high 6/7 ratio of the ultramafic rocks. Field inspection revealed serpentinite was concentrated along

shears in the ultramafic rocks. These shears form gulleys in Table Mountain owing to their lower resistance to erosion. Plate 6 is an atmospherically uncorrected 4/5 image for Table Mountain which shows these gulleys do have high ratios. However, comparison with the CIR composite (Plate 1) shows these gulleys are strongly shadowed. Shadowed areas have similar values in both bands and will have higher 4/5 ratios than the ultramafic rocks, which have a high band 5 value and low band 4 value. Serpentinite, therefore, is not the cause of the high 4/5 ratio in this situation. Nonetheless, the field spectra do suggest recognition of serpentinite in a 4/5 ratio image should be possible provided there is sufficent serpentinite and the area is not shadowed by excessive relief.

Classification

The aim of the classification was to determine whether the DN ranges in the 4/5 and 6/7 ratios from a set of test pixels on North Arm Mountain could be used for an automated classification of all the ultramafic rocks in the four massifs of the Bay of Islands Complex (Figures 3a, b and c). The DN ranges used were the mean plus and minus one standard deviation of the test pixels in the 4/5 and 6/7 ratios. Any pixels within these ranges were classified in the ultramafic rocks/limonite theme and displayed as orange on the imagery. Pixels dominated by either snow or shadow were excluded from this classification by incorporating band 6 and band 7 in the classification. Snow pixels had values greater than 100 in band 6 and shadow pixels had values less than 12 in band 7. Therefore, pixels with values less than 12 in band 7 or greater than 100 in band 6 were excluded from the classification. If snow or shadow pixels had been included they would have been misclassified with the ultramafic/limonite theme due to the similarity of their band ratios. A separate classification of the snow pixels was made and they are displayed as a blue theme on the imagery. The two themes have been displayed on a CIR composite background. Plates 7 to 9 show the areas classified as ultramafic rocks/limonite (orange theme), and snow (blue theme) on North Arm Mountain, Blow Me Down Mountain and the Lewis Hills, respectively. After classification the ultramafic iron/oxide theme was passed through a post classification filter. The post classification filter "cleans" thematic maps by replacing small areas with larger surrounding areas. The minimum area was set to 15 pixels. Therefore, any group of less than 15 pixels was replaced at an equal rate from all sides. Classified pixels were considered part of a group if they were connected horizontally,

vertically or diagonally. Post classification filtering is a subjective technique which may improve the aesthetic quality of the imagery. Areas classified as snow are in agreement with the areas interpreted as snow on the CIR composite.

The areas classified as ultramafic rocks/limonite on North Arm Mountain and the Lewis Hills correlate well with the areas mapped as ultramafic rocks (Plate 7 and 9, Figures 3a and c).

Plate 8 shows the results of a classification of Blow Me Down Mountain using the pixel ranges established on North Arm Mountain. The areas classified as ultramafic rocks on Blow Me Down Mountain do correlate with areas mapped as ultramafic rocks, but much of the area mapped as ultramafic rocks remains unclassified (Plate 8, Figure 3b). This result occurs because not all the ultramafic/limonite pixels on Blow Me Down Mountain fall within the ranges of ultramafic/limonite pixels on North Arm Mountain. There are three possible causes for this difference in the classification ranges of the pixels Blow Me Down Mountain and North Arm Mountain:

1. Many of the ultramafic pixels on Blow Me Down Mountain could include snow.
2. Blow Me Down Mountain has a greater vegetation cover than North Arm Mountain.
3. The stretch applied to the data from Blow Me Down Mountain was different to the stretch applied to the data from North Arm Mountain.

D. TM Data Interpretation

Plate 10, is a computer stretched colour composite of the Hare Bay area with TM bands 1, 2, and 3 displayed as blue, green and red respectively. The ultramafic rocks which form the White Hills Peridotite are evident (coloured brown) (Plate 12, Figure 4). The peridotite appears to consist of both light and dark brown areas. The mean and standard deviation was calculated for a set of pixels from each of these areas (Table 5). These data show a statistical difference between these two areas in TM bands 2, 3 and 7. The DN range in each band, which includes these areas can be stretched over the full range of the system to allow maximum discrimination.

Williams and Smyth (1983), note that the dunites in these ultramafic rocks weather a yellow/brown compared to the surrounding ultramafic rocks which weather dark brown. Dunites outcrop on Mer Mountain in the S. W. corner of the image (Williams, pers. comm.

Table 5. Mean reflectance values ± one standard deviation for a set of pixels from the dunites (light brown) and pyroxene-bearing ultramafic rocks (dark brown) in the TM bands and selected band ratios.

Band	Dunite	Pyroxene-bearing Ultramafics
1	55.18 ± 2.06	60.58 ± 2.52
2	20.05 ± 0.98	24.68 ± 1.36
3	21.55 ± 1.37	27.66 ± 2.46
4	39.32 ± 7.71	32.71 ± 4.09
5	46.18 ± 4.81	50.00 ± 6.04
7	17.55 ± 2.33	24.21 ± 3.37

1984)(Plate 10). Talkington (1979), mapped several occurrences of these dunites including those of Mer Mountain. All the known locations of dunites correspond to the light brown areas on the imagery (Plate 10). This suggests that a spectral difference exists between the dunites and the surrounding pyroxene-bearing ultramafic rocks, and that the dunites have a distinct spectral signature. Several new areas with this signature were recognised on the imagery. If this signature can be confirmed in the future, using ground truthing techniques, it would provide a valuable tool for distinguishing dunite domains from other pyroxene-bearing ultramafic domains, a separation which is both difficult and time consuming in the field.

Band Ratio Imagery

Early workers concluded that in arid environments limonite could be detected using MSS band ratio imagery (Rowan *et al.*, 1974). Limonite is frequently associated with hydrothermal alteration and therefore its remote detection provides a valuable exploration tool. However, limonite areas not associated with alteration, (eg. red beds), cannot be distinguished from hydrothermally associated limonite. Therefore, recent workers have concentrated on separating other hydrothermal minerals (eg. clays) which would be present with limonite of hydrothermal origin but not with limonite of sedimentary origin (Abrams *et al.*, 1982; Rowan

and Kahle, 1982; Rowan *et al.*, 1983). These later workers concluded using simulated TM data that TM band 5 and TM band 7 could be utilized to map clays due to their strong absorption in the TM band 7 position, due to bonding of the OH with metals.

Spectral data obtained in this study indicate that serpentinite, also frequently associated with mineralization, has the same spectral behaviour as clays and should therefore be detectable. The serpentinite is concentrated along shears in the ultramafic rocks which also contain re-mobilised chromite deposits. Any limonite which may have resulted from mineralization cannot be distinguished in this area due to the strong limonite coating on the ultramafic rocks resulting from weathering of olivine and pyroxene. Therefore, detection of serpentinite and hence mineralization would provide a tool for exploration in ultramafic rocks whose limonite coating of non-hydrothermal origin excludes the discrimination of limonite of hydrothermal origin.

Abrams *et al.* (1983), concluded ratios of TM bands 1/5, 4/5 and 5/7 should be most useful for discrimination of iron oxide and clay alteration areas. Band ratios were used to reduce topographic effects (see earlier discussion).

Examination of the spectra obtained from serpentinite indicate serpentinized areas should have a reflectance high in the band 2 position (Figure 33). Therefore, they should have a high 2/3 ratio within areas of ultramafic rocks which will have a low 2/3 ratio. Several linear areas within the ultramafic rocks were observed on a 2/3 ratio image suggesting serpentinization along shear zones. The field ratio data and full spectra suggest both ultramafic rocks and serpentinite should have high 5/7 ratio values. However, the 5/7 ratio of the serpentinite should be higher than that of the ultramafic rocks. Limited laboratory spectra suggest the greater the serpentinization the lower the band 7 value. Provided the band 5 value is not affected by serpentinization, the higher the 5/7 ratio the greater the degree of serpentinisation. A 5/7 ratio image indicated the core of the eastern White Hills peridotite had distinctly higher values than the surrounding peridotite. This could indicate greater serpentinization of the core of the eastern White Hills peridotite than the surrounding peridotite. However, this is extremely speculative and requires ground truthing together with an investigation into possible other causes.

E. Conclusions

1. Compositing and contrast stretching of MSS imagery can be used to distinguish major lithological contacts characterised by changes in the vegetation cover.
2. Atmospherically corrected, operator stretched, MSS band ratio composites can be used to distinguish areas of limonite (including ultramafic rocks) which agree with published data. Since limonite frequently accompanies mineralization, any areas interpreted as limonite using these data and not interpreted on published data might represent potential mineral exploration targets.
3. The band ratio values from a known limonite test site can be used for an automated classification of limonite-rich areas over an entire scene, which agrees with published data.
4. These image analysis techniques may be used in conjunction with the higher spectral and spatial resolution of Thematic Mapper data for detailed mapping of ultramafic rocks. This includes the possible separation of dunites from pyroxene-bearing ultramafic rocks and also the recognition of areas serpentinization. Serpentinization frequently occurs with mineralization along shear zones. Therefore, any serpentinized linear features represent potential mineral exploration targets.
5. Many of the techniques used for geological interpretation of remote sensing data covering arid and semi-arid environments can be applied to data covering a northern maritime environment, and reasonable results obtained.

Plate 1. Colour Infrared Composite of the Bay of Islands Study Area

Plate 2. Band Ratio Composite of North Arm Mtn. 4/5-B, 5/6-G, 6/7-R.

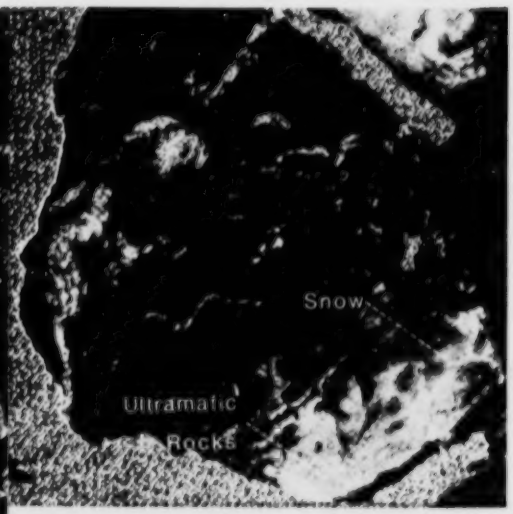

Plate 3. Atmospherically Corrected Band Ratio Composite of North Arm Mtn. 4/5-B, 5/6-G, 6/7-R.

Plate 4. Atmospherically Corrected Band Ratio Composite of Blow Me Down Mtn. 4/5-B, 5/6-G, 6/7-R.

Plate 7. Supervised Classification of Limonite and Snow on North Arm Mtn.

Plate 6. 4/5 Band Ratio Image of Table Mountain.

Plate 5. Atmospherically Corrected Band Ratio Composite of the Lewis Hills. 4/5-B, 5/6-G, 6/7-R.

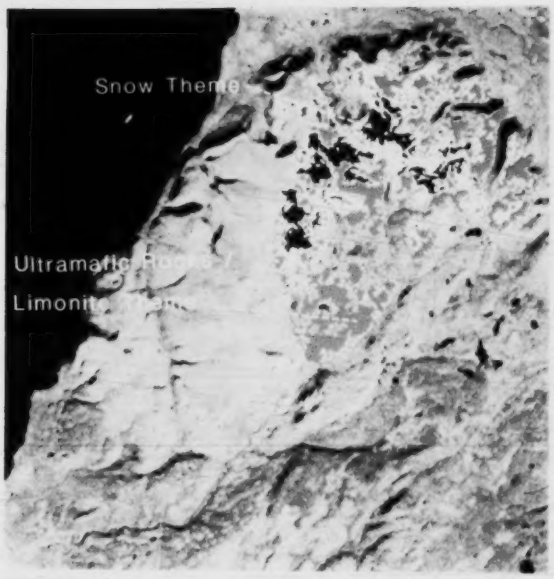

Plate 9. Supervised Classification of Limonite and Snow on the Lewis Hills.

Plate 8. Supervised Classification of Limonite and Snow on Blow Me Down Mtn.

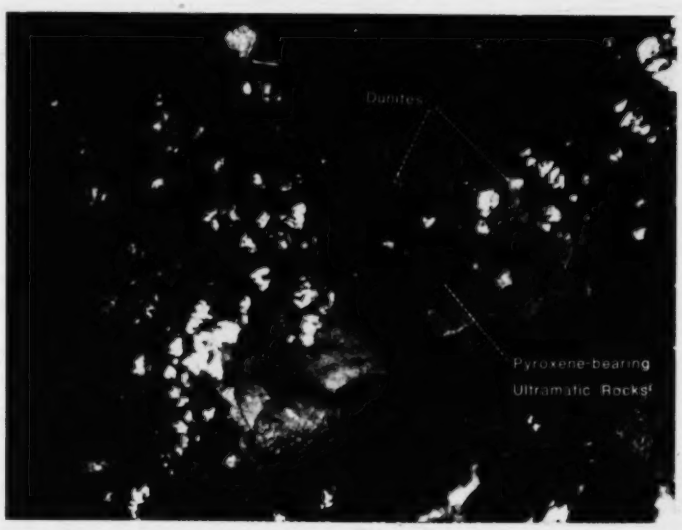

Plate 10. TM Colour Composite of the Hare Bay area
1-B 2-G 3-R

VI. Geophysical Data Integration

A. Introduction

The aim of this part of the project is to use upward and downward continuation and Fourier transforms to determine the location of the aeromagnetic lineaments and anomalies. The locations of these lineaments and anomalies are then compared to the locations of the geological contacts, faults, Landsat lineaments and mineral occurrences to determine if they are interrelated.

Processing and interpretation of the aeromagnetic data was carried out in close cooperation with Dr. J. C. Samson of the Physics Department at the University of Alberta. Detailed discussion of the techniques and programs used for manipulation of the geophysical data is considered beyond the scope of this project. Where relevant, the reader is referred to more detailed sources.

B. Methodology

Digital aeromagnetic data covering NTS 1:250,000 sheets:

12G 9, 8 and 1

12B 15, 16, 11, 10, 9, 8 and 7

12H 12, 5, 6, 4 and 3

12A 13 and 12

were obtained from the Geological Survey of Canada. These data were interpolated onto a grid, the regional trend removed and contoured. Several areas from the contoured data were chosen for a more detailed examination of their aeromagnetic signatures (Table 6).

The aeromagnetic data in these areas were re-gridded, the regional trend removed and a fast fourier transformation applied and a fourier amplitude diagram produced. The fourier transform can be used for characterising linear systems and for identifying the frequency components making up a continuous waveform (Bergland, 1979). The fourier transform is discussed in more detail in the interpretation section. The data were then continued upward and downward. Continuation projects the magnetic intensity from the surface of the earth upward to higher levels or downward to lower levels approaching or coincident with the rocks producing the field (Peters, 1949). After weighting the transform to compute the continued transform, an

inverse fourier transform was applied in order to compute the magnetic fields.

C. Interpretation

Lineation mapping on the contoured areomagnetic data was performed using the method described by Affleck (1963). This involved drawing lines along closed highs and lows and along the open noses and flexures in the contour lines. Figure 44 shows the detrended aeromagnetic data for the Lewis Hills. The corresponding Landsat lineament map and geological map are given in Figures 45 and 3c respectively. Comparison of the interpreted aeromagnetic and Landsat lineament maps indicates:

1. Several of the aeromagnetic lineaments are also Landsat lineaments.
2. Several of the geological faults are aeromagnetic lineaments.
3. Several aeromagnetic lineaments follow dykes.
4. The main aeromagnetic lineaments which connect highs and lows follow the major axes of the elongate lithological domains.
5. The main mineral occurrence clusters are located on aeromagnetic highs and aeromagnetic lineaments.

An example of the fourth point are the peridotite crystal mush intrusions. These trend N-S and

Table 6. Sub areas chosen for detailed analysis of their aeromagnetic signatures.

Longitude	Latitude	General Area
58.34 - 57.93	49.17 - 49.59	Table Mountain and North Arm Mountain, Bay of Islands Complex, W. Nfld.
58.43 - 58.13	48.89 - 49.07	Blow Me Down Mountain, Bay of Islands Complex, W. Nfld.
58.63 - 58.33	48.73 - 48.93	Lewis Hills, Bay of Islands Complex, W. Nfld.

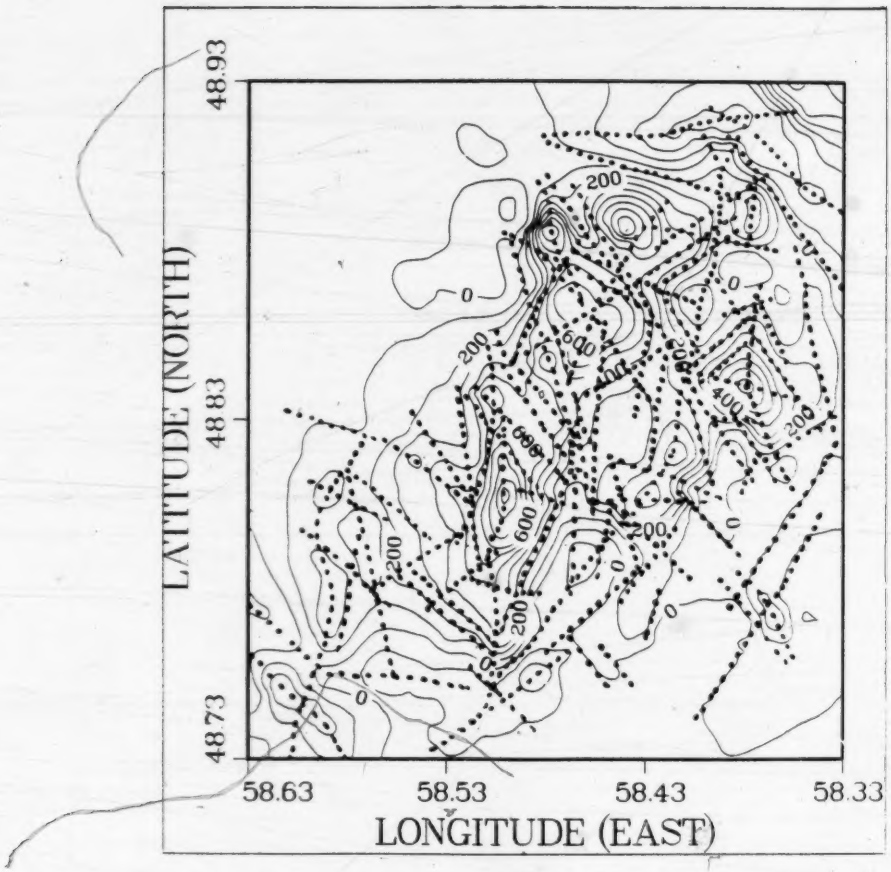

Figure 44. Lewis Hills detrended aeromagnetic data and interpreted lineaments.

are offset dextrally (Figures 44 and 3c). A distinct aeromagnetic lineament is located along the axis of the intrusions and is also offset dextrally in the same position. This suggests the geological units have distinct aeromagnetic signatures as opposed to faults. The faults will only be apparent if they offset two distinct geological units.

An example of the fifth point is the cluster of mineral occurrences on the eastern side of the Lewis Hills (Figures 44 and 45).

Levandowski *et al.* (1974), also noted a marked coincidence of mineral occurrences with aeromagnetic anomalies, and also high Landsat lineament densities, in North-Central Nevada.

Figure 47 is a plot of the fourier amplitudes of the aeromagnetic data in Figure 44. A detailed description of the fourier transformation is beyond the scope of this project. The interested reader is referred to Bergland (1979), for a detailed description. The following is a

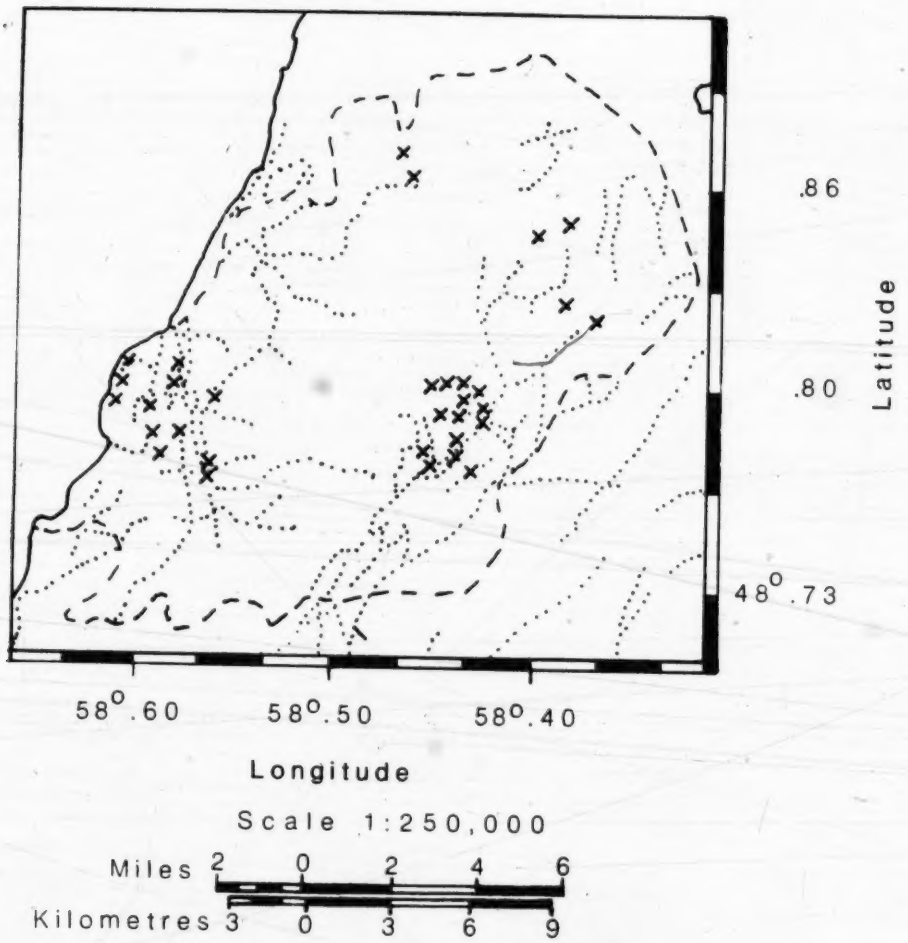

Figure 45. Lewis Hills Landsat lineament map. (X - Mineral Occurrence.)

brief outline of how the fourier transform works and how the resultant fourier amplitude plot is interpreted.

A series of aligned lineaments can be considered as a waveform in which the frequency or wavenumber is inversely proportional to the spacing of the lineaments (Figure 46). The frequency and direction of the waveform are combined by means of the fast fourier transform to give the fourier amplitude plot (Figure 46). In Figure 46 there are two N-S trending lineaments. This results in two points along an E-W axis on the fourier amplitude plot centered at the second wavenumber position. The wavenumber corresponds to the number of lineaments. The two points are located along the E-W axis since the wave fitted to the lineaments is at right

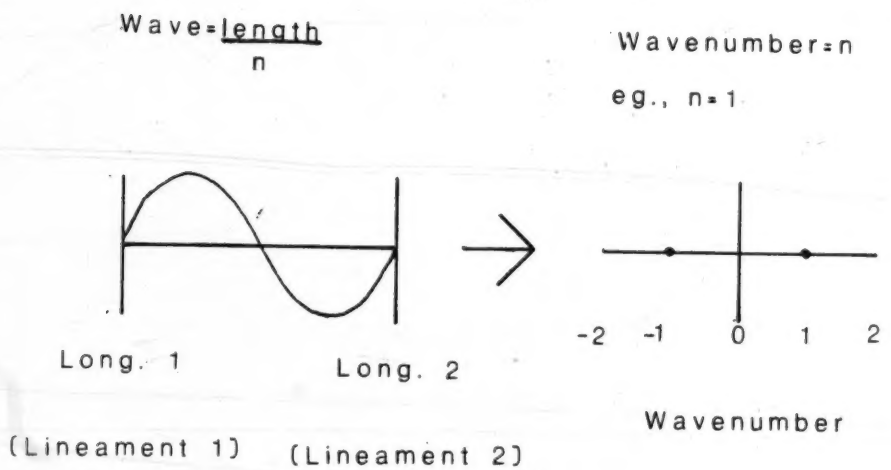

Figure 46. Waveform and Fast Fourier Amplitude Plot for a 2 N-S trending lineaments.

angles to the lineament direction. Therefore, the direction at 90° to the axis of the centers on the fourier amplitude plot is the lineament trend direction.

In the fourier amplitude plot for the detrended Lewis Hills data four distinct trends are apparent labelled T1, T2 , T3 and T4 (Figure 47). T1 indicates several ENE-WSW lineaments such be present and several were interpreted. T2 indicates several NE-SW lineaments should be present and aeveral were interpreted. T3 indicates there should be three N-S trending lineaments and three N-S trending lineaments were mapped on the aeromagnetic map. T4 indicates there should be some NE-SW trending lineaments and several lineaments with this trend were mapped. The coastline and western and eastern edges of the Lewis Hills Massif are orientated NE-SW and will also contribute to this trend. Therefore, the fourier amplitude plot provides an aid to interpreting which lineament trends should be present in the data.

Figure 48 shows the detrended aeromagnetic data for the Lewis Hills after they have been continued up 1.5 grid units and the interpreted lineaments. Upward continuation enhances the major lineament directions. Most of the lineaments interpreted on the upward continued

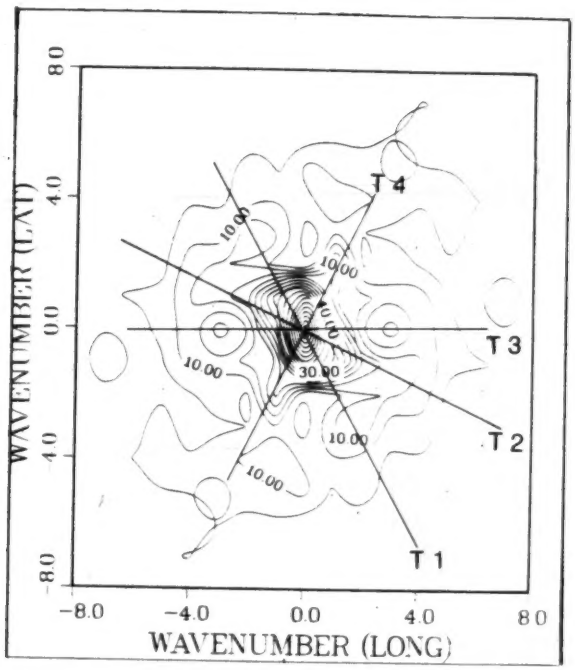

Figure 47. Fourier Amplitude plot of the Lewis Hills detrended aeromagnetic data

data correspond to lineaments interpreted on the detrended data. However, several of the minor lineaments on the detrended data were not observed on the upward continued data. Some of the faults on the geological map correspond to aeromagnetic lineaments. However, the main aeromagnetic lineaments follow the axes elongate geological units, as was the case with the aeromagnetic lineaments interpreted on the detrended data. Both the clusters of mineral occurrences are centered on distinct highs and on aeromagnetic lineaments. Figure 49 shows the fourier amplitude plot of the upward continued data. Three of the four trends observed in the fourier amplitude plot of the detrended data were also observed in this plot. and are interpreted in the same manner. The T1 trend in the detrended data corresponding to the ENE-WSW lineaments was not observed in the upward continued data. Most of the lineaments with this trend were minor and lost in the upward continuation.

Figure 50 shows the detrended data for the Lewis Hills after they have been continued down 1.5 grid units. Downward continuation enhances the minor lineaments and as a result more lineaments were interpreted with these data. Again the major lineaments follow the axes

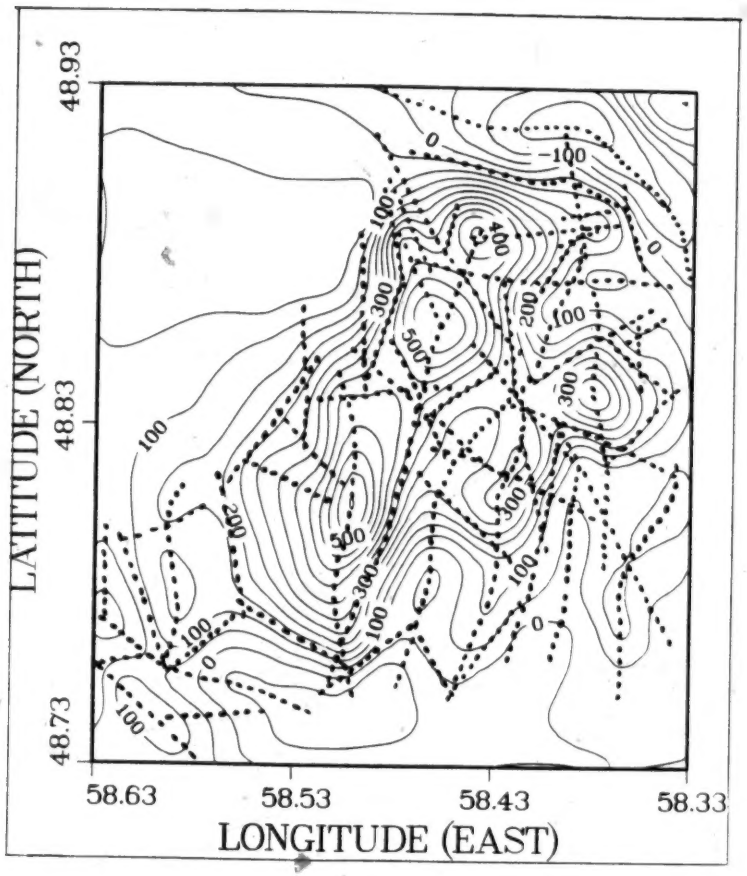

Figure 48. Lewis Hills detrended aeromagnetic data continued up 1.5 grid units and interpreted lineaments.

of the elongate geological units, and several of the minor lineaments follow the fault lines. Several more N-S lineaments were interpreted than were interpreted in the detrended data. This N-S trend follows the deformational trend in the mafic gneisses and amphibolites of the Lewis Hills. The fourier amplitude plot of the downward continued data shows the same principle trends as the fourier amplitude plot of the detrended data from this area and is explained in the same manner (Figures 47 and 51). Both the upward and downward continuation suggest the major aeromagnetic lineaments follow the axes of the elongate geological units and the minor aeromagnetic lineaments follow the fault lines and deformational trends. Figure 52 shows the detrended aeromagnetic data and interpreted aeromagnetic lineaments for Blow Me Down Mountain. Comparison with the interpreted Landsat lineaments indicates some of the aeromagnetic lineaments correspond to Landsat lineaments (Figures 52 and 53). The

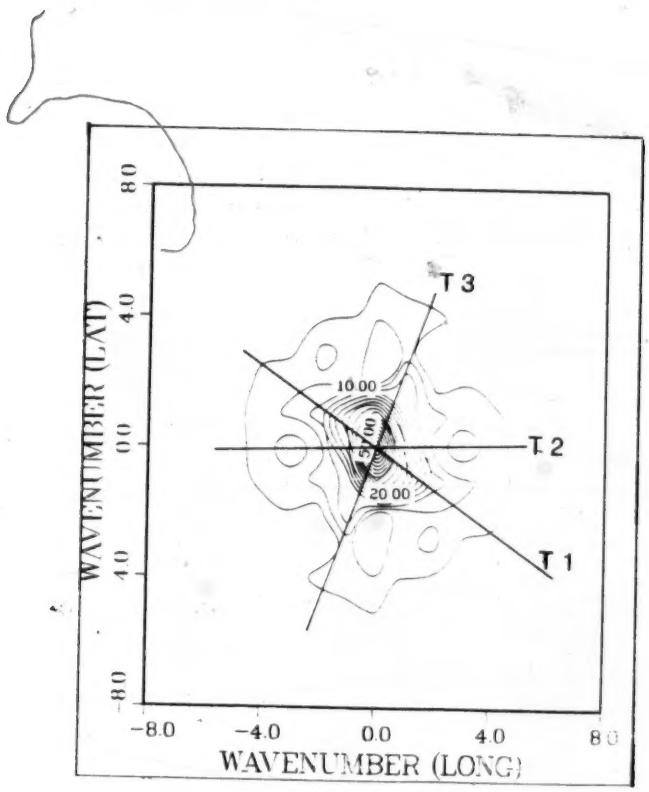

Figure 49. Fourier amplitude plot of the Lewis Hills detrended aeromagnetic data continued up 1.5 grid units.

aeromagnetic lineaments located along the axes of the major aeromagnetic highs and lows follow the axes of the elongate geological units, as was the case with the Lewis Hills lineaments. For example, aeromagnetic lineaments follow the axes of the elongate pillow basalts outcrops and the elongate sheeted dykes outcrops (Figures 52 and 3b). Figure 54 shows the fourier amplitude plot of the detrended aeromagnetic data of Blow Me Down Mountain. Four lineament trends have been interpreted on this fourier amplitude plot (T1, T2, T3 and T4). T1 suggests there should be two N-S trending lineaments and two such lineaments were observed. T2 suggests there should be NE-SW trending lineaments and several such lineaments were interpreted. However, the edges of the massif also have this trend and will be included in the T2 trend. T3 suggests there should be some NW-SE lineaments and several such lineaments were interpreted. This trend corresponds to the strike direction of the layering in the mafic and ultramafic rocks. T4 suggests there should be some ENE-WSW lineaments and some were observed. The fourier amplitude plots from the Lewis Hills and Blow Me Down Mountain indicate both massifs have similar aeromagnetic trends. This is also apparent by comparing the

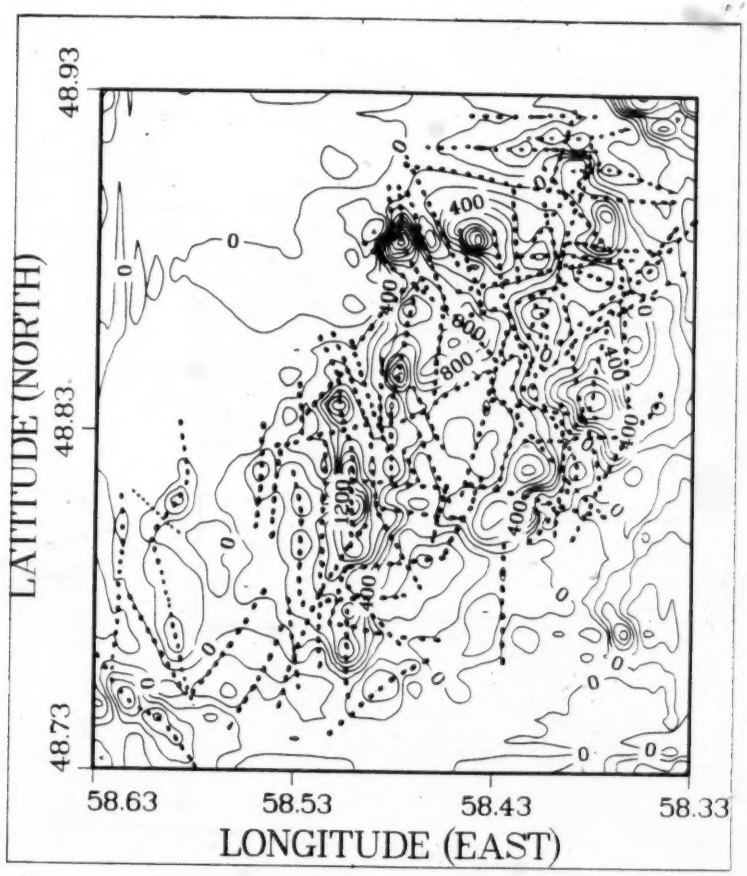

Figure 50. Lewis Hills detrended aeromagnetic data continued down 1.5 grid units and interpreted lineaments.

interpreted lineaments patterns on the aeromagnetic data from each area (Figures 44 and 54). The mineral occurrences in the Blow Me Down Mountain Massif are not centered on the aeromagnetic highs but are located on the interpreted aeromagnetic lineaments. Figure 55 shows the detrended aeromagnetic data for Blow Me Down Mountain continued up 1.5 grid units and the interpreted lineaments. Most of the interpreted lineaments on the upward continued data correspond to those lineaments interpreted in the detrended data. However, the upward continuation has enhanced the major lineaments and subdued the minor lineaments. This is apparent in the fourier amplitude plot for the upward continued data in which the major trends are now distinct and the minor trends have been removed (Figure 56). Figure 57 shows the detrended aeromagnetic data for Blow Me Down Mountain continued down 1.0 grid units and the interpreted lineaments. The lineaments interpeted in the detrended data are still apparent in

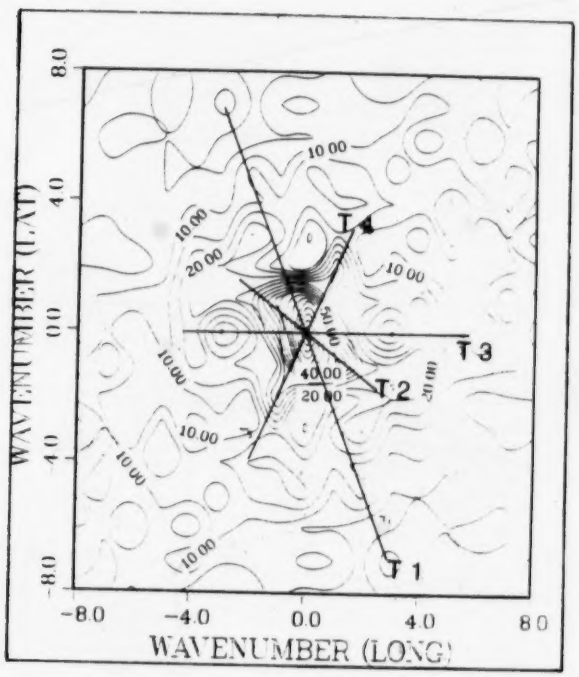

Figure 51. Fourier amplitude plot of the Lewis Hills detrended aeromagnetic data continued down 1.5 grid units.

the downward continued data and interpreted in the same manner. The fourier amplitude plot for the downward continued data is complex but shows the same trends as fourier amplitude plots of the detrended and upward continued data confirming the trends of the interpreted lineaments.(Figures 54, 56 and 58).

Figure 59 shows the detrended aeromagnetic data for North Arm Mountain and Table Mountain and the interpreted lineaments. Most of the interpreted lineaments trend N-S, NE-SW and E-W. The E-W trend is dominant over the other trends. The E-W trend was minor in the interpreted aeromagnetic lineaments from the Lewis Hills or Blow Me Down Mountain. Comparison with the Landsat lineament map for the area shows many of the aeromagnetic lineaments have matching Landsat lineaments (Figures 59 and 60). However, there is a distinct absence of E-W trending Landsat lineaments compared to E-W trending aeromagnetic lineaments (Figures 59 and 60). The abscence of these E-W lineaments in the Landsat data may result from the location of the sun in the east when the Landsat data were gathered. This causes shadowing and therefore enhancement of the N-S lineaments over the

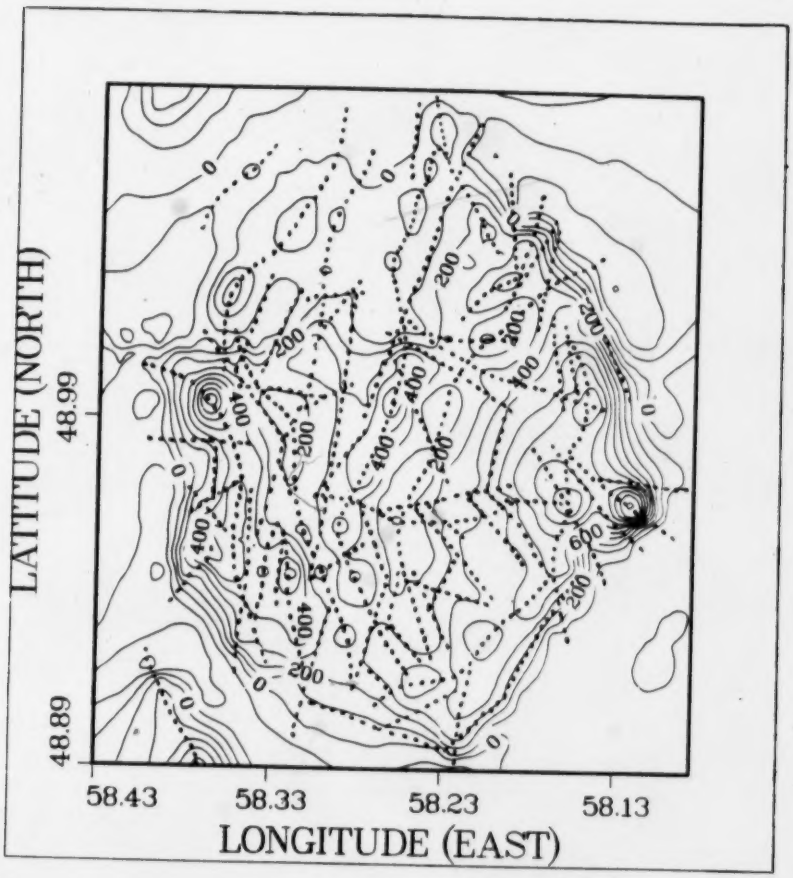

Figure 52. Blow Me Down Mountain detrended aeromagnetic data and interpreted lineaments.

E-W lineaments. This bias is not present in the aeromagnetic data. Comparison with the geological map for the area reveals that as in the case of the Lewis Hills or Blow Me Down Mountain data the interpreted aeromagnetic lineaments along the major closed aeromagnetic highs and lows follow the axes of the elongate geological units. Examination of more detailed geological data from the North Arm Mountain and Table Mountain areas indicate other aeromagnetic trends corresponding to the trend of the layering and foliation in the mafic and ultramafic rocks.

Most of the mineral occurrences in this area are located along interpreted aeromagnetic lineaments and on minor aeromagnetic highs (Figures 59 and 60). Figure 61 shows the fourier amplitude plot for the detrended aeromagnetic data from North Arm Mountain and Table Mountain. Four trends were interpreted on the fourier amplitude plot (T1, T2, T3 and T4) all

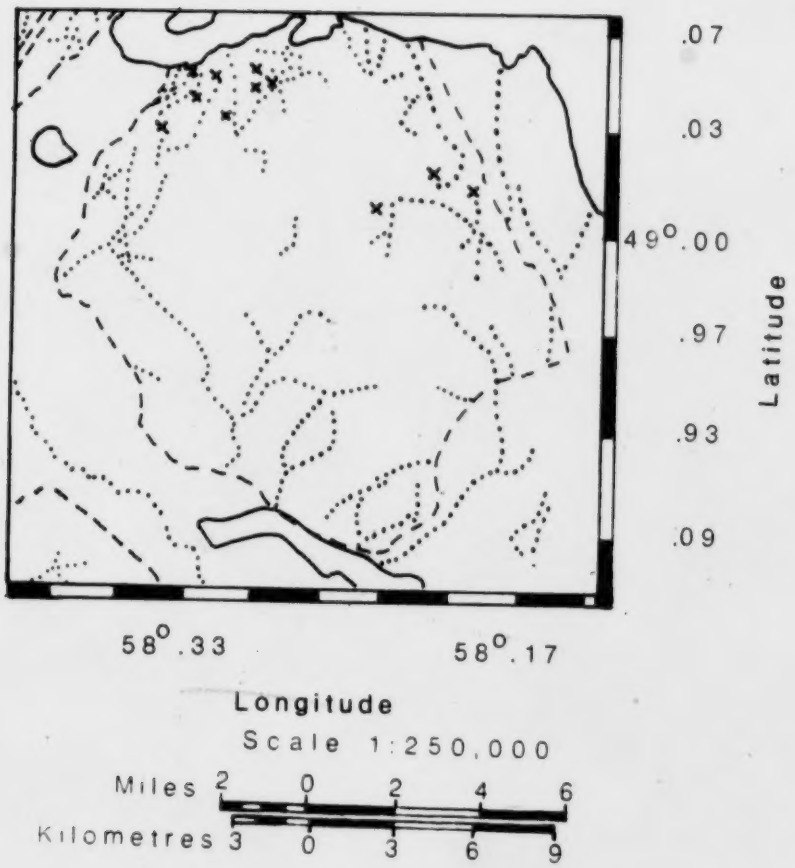

Figure 53. Blow Me Down Mountain Landsat lineament map. (X - Mineral Occurrence.)

of which correspond to lineament trends interpreted in the aeromagnetic data.

Figure 62 shows the detrended data for North Arm Mountain and Table Mountain continued up 1.5 grid units. Most of the lineaments interpreted on the detrended data were also interpreted on the upward continued data. However, several of the N-S trending lineaments were interpreted as trending NW-SE on the upward continued data. The trends interpreted on the fourier amplitude plot for the upward continued data agree with those interpreted in the upward continued aeromagnetic data (Figures 61 and 62).

Figure 63 shows the detrended data from North Arm Mountain and Table Mountain continued down 1.0 grid units and the interpreted lineaments. The majority of the lineaments

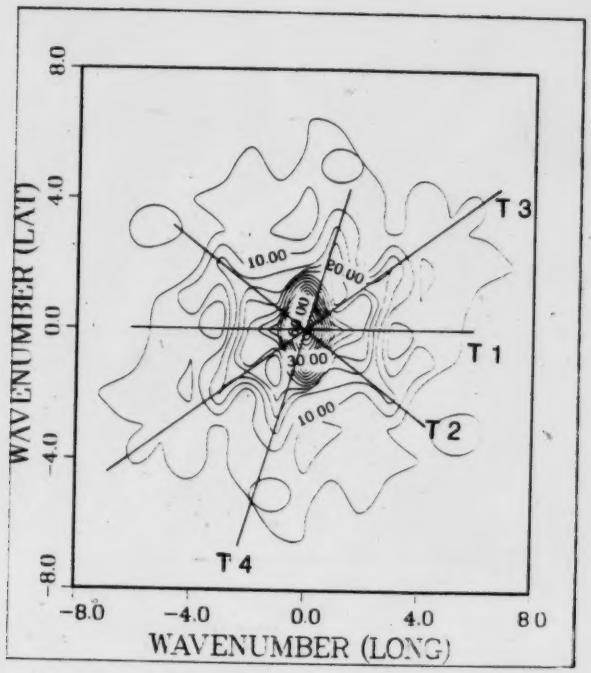

Figure 54. Fourier amplitude plot for the Blow Me Down Mountain detrended aeromagnetic data.

trend NW-SE or E-W. Again several of the NW-SE trending lineaments have replaced the N-S trending lineaments interpreted in the detrended data. Figure 64 is the fourier amplitude plot for the downward continued data. The only distinct trend apparent in this plot is the NE-SW trend which corresponds to the edges of the massif.

D. Conclusions

1. Several interpreted Landsat lineaments correspond to interpreted aeromagnetic lineaments.
2. Most of the major clusters of known mineral occurrences are located along aeromagnetic lineaments.
3. Some of the major clusters of known mineral occurrences are located on distinct aeromagnetic highs.
4. The major aeromagnetic lineaments which are located along closed highs and lows, follow the major axes of the elongate lithological domains.
5. The major aeromagnetic lineaments can be enhanced by upward continuation and the minor aeromagnetic lineaments can be enhanced by downward continuation.
6. The fourier amplitude plot provides information on the number and trends of the lineaments which should be present in the aeromagnetic data. The similarity of the aeromagnetic lineament patterns for each of the massifs suggest they had similar methods of emplacement and geological histories.

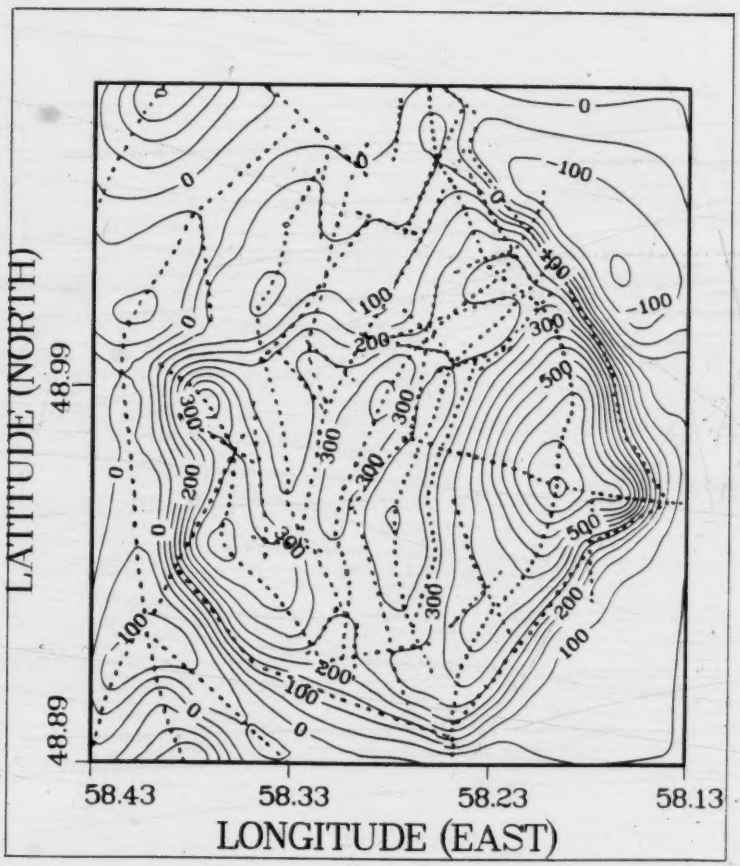

Figure 55. Blow Me Down Mountain detrended aeromagnetic data continued up 1.5 grid units and interpreted lineaments.

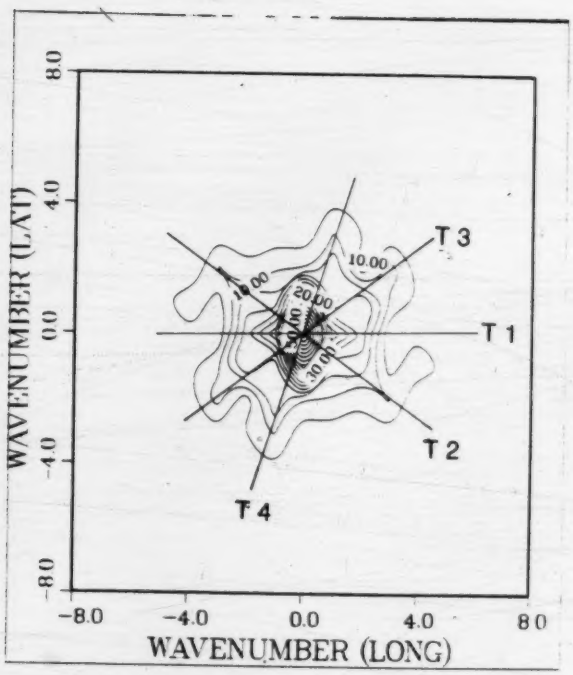

Figure 56. Fourier amplitude plot of the Blow Me Down Mountain detrended aeromagnetic data continued up 1.5 grid units.

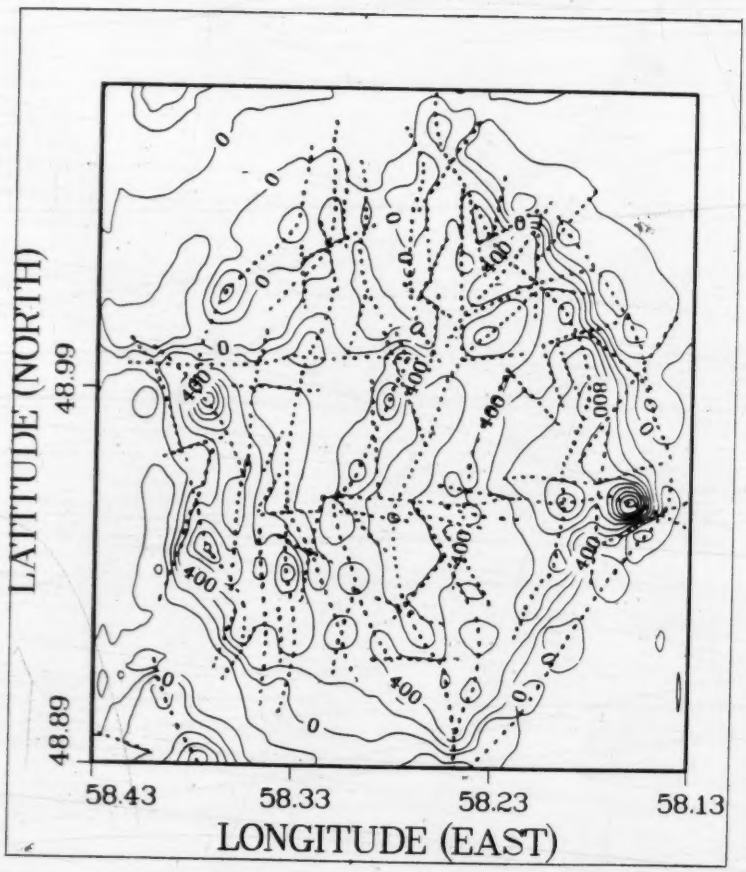

Figure 57. Blow Me Down Mountain detrended aeromagnetic data continued down 1.0 grid units and interpreted lineaments.

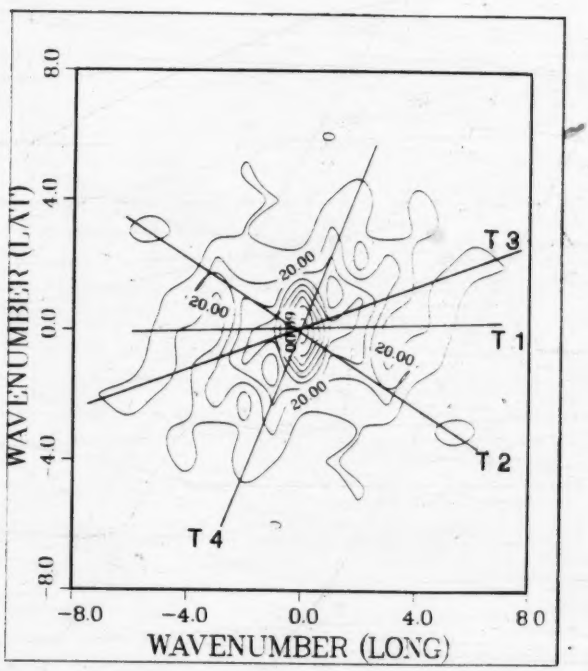

Figure 58. Fourier amplitude plot of the Blow Me Down Mountain detrended aeromagnetic data continued down 1.0 grid units.

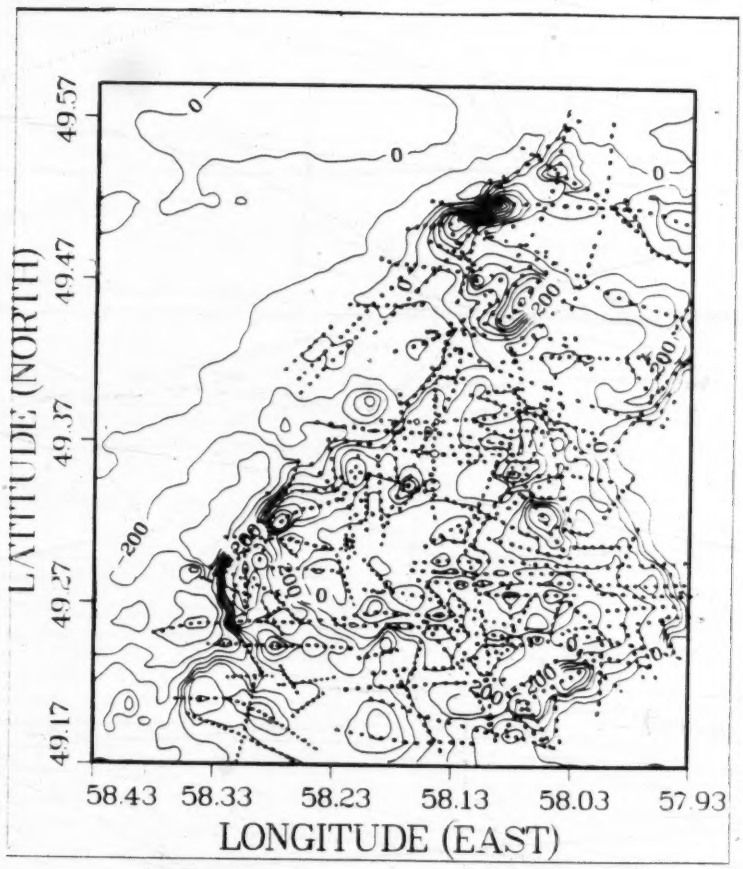

Figure 59. Table Mountain and North Arm Mountain detrended aeromagnetic data and interpreted lineaments.

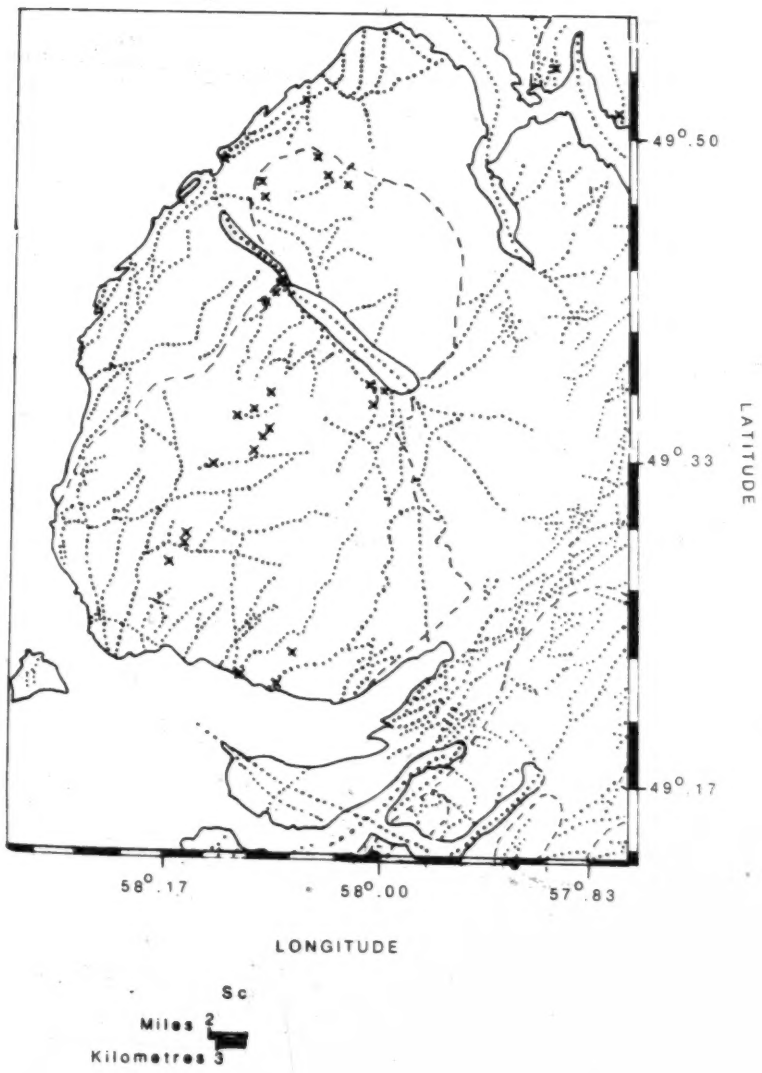

Figure 60. Table Mountain and North Arm Mountain Landsat lineament map. (X - Mineral Occurrence.)

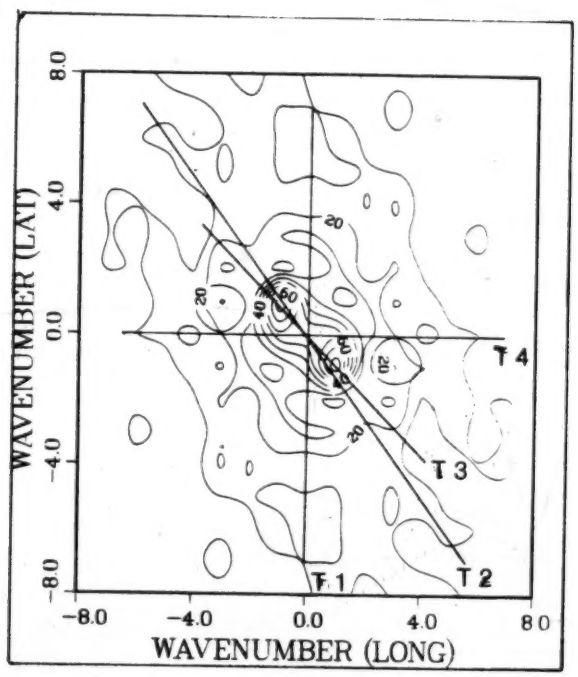

Figure 61. Fourier amplitude plot of the Table Mountain and North Arm Mountain detrended aeromagnetic data.

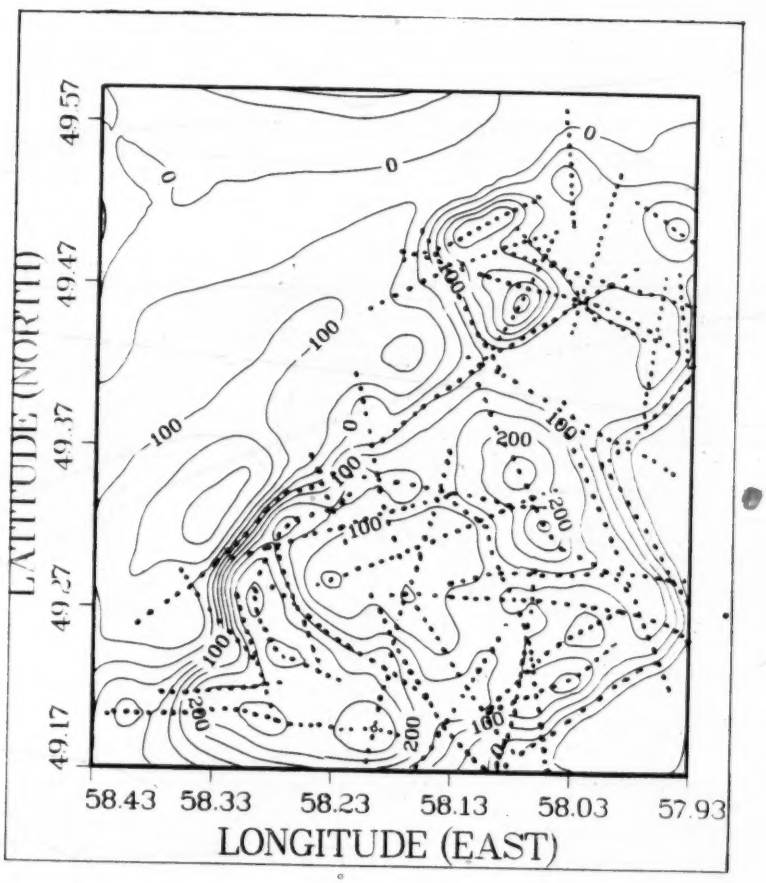

Figure 62. Table Mountain and North Arm Mountain detrended aeromagnetic data continued up 1.5 grid units and interpreted lineaments.

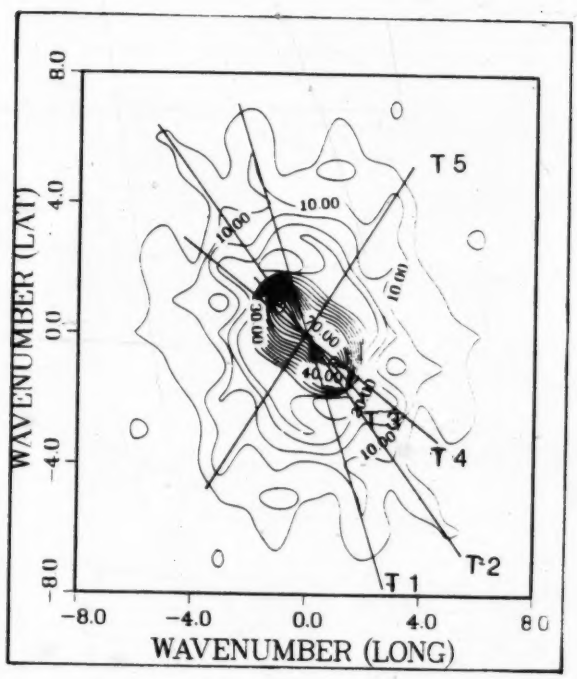

Figure 63. Fourier amplitude plot of Table Mountain and North Arm Mountain detrended aeromagnetic data continued up 1.5 grid units.

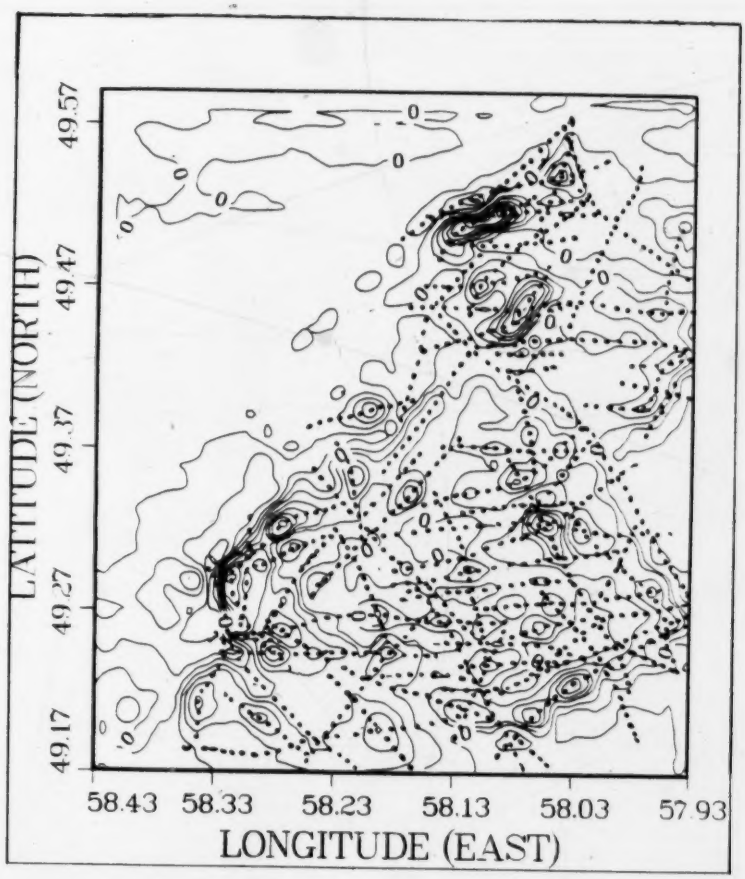

Figure 64. Table Mountain and North Arm Mountain detrended aeromagnetic data continued down 1.0 grid units and interpreted lineament.

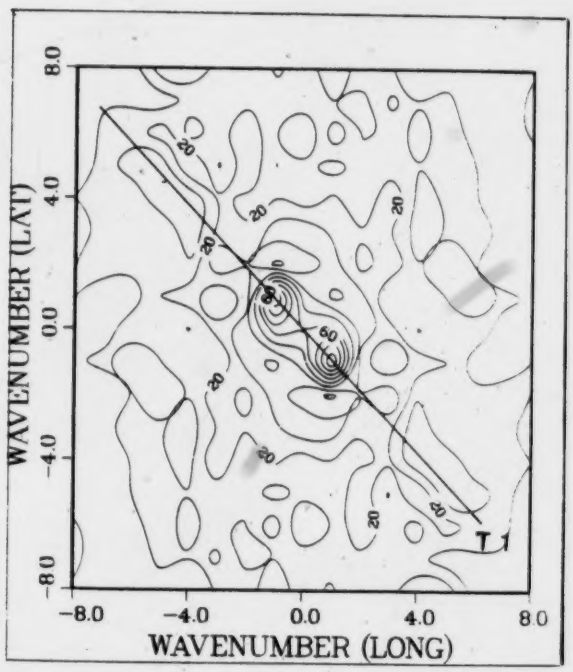
WAVENUMBER (LAT)
8.0
4.0
0.0
-4.0
-8.0
-8.0
-4.0
0.0
4.0
8.0
WAVENUMBER (LONG)
20
20
20

VII. Conclusions and Future Recommendations

The objective of this study was to evaluate the use of MSS and TM data integrated with geophysical data for mineral exploration and geological mapping in environments similar to Western Newfoundland.

Interpretation of Landsat and aeromagnetic data has established the principle clusters of mineral occurrences are located in areas of high Landsat lineament density and on aeromagnetic lineaments and anomalies. Furthermore, Landsat MSS and TM imagery has been used to delineate areas of limonite and serpentinite which frequently have a strong genetic relationship with mineralization. Therefore, areas which conform to any of the following criteria represent potential exploration targets:

1. High Landsat lineament density.
2. Located on an aeromagnetic lineament.
3. Located on an aeromagnetic anomaly.
4. Presence of limonite (excluding ultramafic rocks).
5. Presence of serpentinite.

As part of an exploration program interpretation of Landsat data integrated with aeromagnetic provides a major tool for delineating areas of high mineralization potential.

Comparison of the lineament patterns from the major geological units has established that the complexity of the lineament pattern increases with the age of the geological unit. Digital analysis of MSS and TM imagery has been used to delineate several major geological units, and identify certain rock types.

Therefore, combined interpretation of lineament patterns and digital data provide a technique for mapping geological units, establishing their relative ages and identifying certain rock types. This mapping technique could be used in remote areas to produce regional geological maps from which key areas could be selected for detailed study.

The costs of the various data bases used in this study are given in Appendix II. This provides an exploration company with an indication of the cost of the intial data, it excludes any costs for computing, image analysis facilities and interpretation.

The subsequent paragraphs deal with some of the pros. and cons. of using these data as opposed to other data eg., aerial photography. The limited spatial resolution of the Landsat MSS data is well suited to regional structural analysis as was observed in other studies (Abrams

et al., 1983). If air photos had been used for lineament analysis their increased spatial resolution would cause increased lineament recognition and therefore increased processing and interpretation time. Furthermore, certain major lineaments recognised through the synoptic view provided by the MSS data may not have been recognised as covering several air photographs. Therefore, although air photo interpretation would provide the most detailed analysis, the Landsat imagery provides a rapid and hence cheaper technique for regional analysis from which key areas can be selected for detailed air photo study.

Image analysis using the digital MSS and TM data provides a tool for lithological and alteration zone mapping. Presently, image analysis facilities are available free of charge for both research and industry at the Alberta Remote Sensing Center. This is unlikely to remain the case for industry in the future. In addition, an understanding of both how the image analysis software functions and how the resultant data can be interpreted requires a substantial amount of training. Therefore, if industry decides to use this very powerful tool, a financial comittment must be anticipated in terms of access to image analysis equipment and consultation with, or training of skilled interpreters.

Finally, most of the relationships suggested here will require a substantial amount of ground truthing and testing in other areas before their validity will be fully established. The author firmly believes that the potential of Landsat imagery as a mapping and exploration tool will never be fully exploited until these and other interpreted relationships are adequately ground truthed. With this in mind, studies similar to this should become part of any serious mapping or exploration program and should play an increasingly important role as the spectral and spatial resolution of airborne and satellite remote sensing systems improve.

VIII. References

Abrams, M. J., Brown, D., Lepley, L., and Sadowski, R., 1983, Remote Sensing for Porphyry Copper Deposits in Southern Arizona: Economic Geology, v. 78 p.591-605

Baird, D. M., 1959, Sandy Lake (West Half), Newfoundland: Geological Survey of Canada Map 47-1959.

Bernstein, R., and Ferneyhough, D. G. Jr., 1975, Digital Image Processing: Photogrammetric Engineering and Remote Sensing, V. 41, No. 12, p.1465-1476.

Bergland, G. D., 1969, A guided tour of the fast Fourier transform: IEEE Spectrum July 1969.

Blom, R. G., Abrams, M. J., and Adams, H. G., 1980, Spectral Reflectance and Discrimination of Plutonic Rocks in the 0.45- to 2.45-um Region: Journal of Geophysical Research, v. 85, No. B5, p.2638-2648.

Botherel, A., Cervelle, B., Chorowicz, J., and Tamain, J., 1984, Spectral signatures (visible/near infrared) of rocks and ores: Application to remote sensing of three types of orebodies from S. Morocco: Modern Geology, v. 8, p.277-294.

Bostock, H. H., 1983, Precambrian Rocks of the Strait of Belle Isle Area, *in* Geology of the Strait of Belle Isle Area, Northwestern Insular Newfoundland, Southern Labrador, and Adjacent Quebec: Geological Survey of Canada Memoir 400, p.1-73.

Casey, J. F., and Kidd, W. F. S., 1981, A parallochthonous group of sedimentary rocks unconformably overlying the Bay of Islands ophiolite complex, North Arm Mountain, Newfoundland: Canadian Journal of Earth Sciences, **18** p. 1035-1050.

Cervelle, B. D., and Maquet, M., 1982, Cristallochimie des lizardites substituees Mg-Fe-Ni par

spectrometrie visible et infrarouge proche: Clay Minerals *17* p.377-392.

Conradsen, K., and Harpøth, O., 1984, Use of Landsat Multispectral Scanner Data for Detection and Reconnaissance Mapping of Iron Oxide Staining in Mineral Exploration, Central East Greenland: Economic Geology, v. 79, p.1229-1224.

Erdmer, P., 1984, Summary of fieldwork in the northern Long Range Mountains, western Newfoundland: *in* Current Research, Part A, Geological Survey of Canada, Paper 84-1A, p. 521-530.

Elthon, D., Casey, J. F., and Komor, S., 1984, Cryptic mineral-chemistry variation in a detailed traverse through the cumulate ultramafic rocks of the North Arm Moutain massif of the Bay of Islands ophiolite, Newfoundland, *in* Gass, I. G., Lippard, S. J., and Snelton, A. W., ed., Ophiolites and the Oceanic Lithosphere: Geological Society Special Publication No. 13, p.85.

Gladwell, D. R., Lett, R. E., and Lawrence, P., 1983, Application of reflectance spectroscopy to mineral exploration using portable radiometers: Economic Geology, v. 78, p.699-710.

Goetz, A. F. H., Rock, B. N., Rowan, L. C., 1983, Remote Sensing for Exploration : An overview: Economic Geology, v. 78, p.573-590.

Favorskaya, M. A., and Volchanskaya, I. K., 1983, Detection of latent dislocation systems from space images as a basis for mineralization prognosis: Global Tectonics and Metallogeny, v. 2, Nos. 1 and 2.

Harris, J. R., and Slaney, V. R., 1982, A comparison of Landsat and SEASAT imagery for geological mapping in difficult terrain: International Symposium on Remote Sensing of the Environment, Second Thematic Conference, Remote Sensing for Exploration Geology, Fort Worth, Texas, Proc., 805-813, 1982.

Heyl, A. V., 1983, Some major lineaments reflecting deep-seated fracture zones in the central United States, and mineral districts related to the zones: Global Tectonics and Metallogeny, v. 2, Nos. 1 and 2.

Hunt, G. R., 1977, Spectral signatures of particulate minerals in the visible and near-infrared: Geophysics, v. 42, No. 3, p.501-503.

Hunt, G. R., 1979, Near-infrared (1.3-2.4um) spectra of alteration mineralsPotential use in remote sensing: Geophysics, v. 44, No. 12, p.1974-1986.

Hunt, G. R., and Salisbury, J. W., 1970, Visible and near-infrared spectra of minerals and rocks: I. Silicate minerals: Modern Geology, v. 1, p.283-300.

Hunt, G. R., Salisbury, J. W., and Lenhoff, C. J., 1971, Visible and near-infrared spectra of minerals and rocks: III. Oxides and Hydroxides: Modern Geology, v. 2, p195-205.

Hunt, G. R., Salisbury, J. W., and Lenhoff, C. J., 1973a, Visible and near-infrared spectra of minerals and rocks: VI. Additional silicates: Modern Geology, v. 4, p.85-106.

Hunt, G. R., Salisbury, J. W., and Lenhoff, C. J., 1973b, Visible and near-infrared spectra of minerals and rocks: VII. Acidic igneous rocks: Modern Geology, v. 4, p217-224.

Hunt, G. R., Salisbury, J. W., and Lenhoff, C. J., 1974, Visible and near-infrared spectra of minerals and rocks; IX. Basic and Ultrabasic rocks: Modern Geology, v. 5, p.15-22.

Hunt, G. R., and Salisbury, J. W., 1978, Assessment of Landsat filters for rock type discrimination, based on intrinsic information in Laboratory Spectra: Geophysics, v. 43, No. 4, p.738-747.

Hunt, G. R., and Wynn, J. C., 1979, Visible and near-infrared spectra of rocks from chromium-rich areas: Geophysics, v. 44, No. 4, p. 820-825.

Hunt, G. R., and Ashley, R. P., 1979, Spectra of Altered Rocks in the Visible and Near-Infrared: Economic Geology, v. 74, p.1613-1629.

Jamieson, R. A., 1977, A suite of alkali basalts and gabbros associated with the Hare Bay Allochthon of western Newfoundland: Canadian Journal of Earth Sciences, **14**, p346-356.

Karson, J., 1984, Variation in structure and petrology in the Coastal Complex Newfoundlands anatomy of an oceanic fracture zone. *in* Gass, I. G., Lippard, S. J., and Snelthon, A. W., ed., Ophiolites and the Oceanic Lithosphere: Geological Society Special Publication No. 13, p.135

Kennedy, D. P., 1980, Geology of the Corner Brook Lake Area, Western Newfoundland: *in* Current Reearch, Part A, Geological Survey of Canada, Paper 80-1A, p.235-240.

Lang, H. R., 1982, Finding the Lost River Gas Field: Lineament Density Analysis in Hydrocarbon Exploration: Proceedings, 1982 International Geoscience and Remote Sensing Symposium (IGARSS '82), Munich, Federal Republic of Germany, 1-4 June 1982:1.

Levandowski, D. W., Jennings, T. V., and Lehman, W. T., 1974, Relations between ERTS lineaments, aeromagnetic anomalies and geological structures in North-Central Nevada: Proceedings, 1st. International Conference on New Basement Tectonics, Utah Geological Association, Publication No. 5.

Longshaw, T. J., 1976, Application of an analytical approach to field spectroscopy in geological remote sensing: Modern Geology, v. 5, p.201-210.

Mark, D. M., 1973, Analysis of Axial Orientation Data Including Till Fabrics: Geological Society of America Bulletin, v. 84, p.1369-1374.

Mineral Occurrence Tables Newfoundland, 1976, Mineral Development Division Department of Mines and Energy, Open File: Nfld. 888.

Moik, J. G., 1980, Digital processing of remotely sensed images: NASA Special Publication 431.

Nyman, M., Quinn, L., Reusch, D. N., and Williams, H., 1984, Geology of the Lomond map area, Newfoundland: *in* Current Research, Part A, Geological Survey of Canada, Paper 84-1A, p.157-164

O'leary, D. W., Friedman, J. D., and Pohn, H. A., 1976, Lineament, linear, lineation: Some proposed new standards for old terms: Geological Society of America Bulletin, v. 87, p.1463-1469.

Peters, 1949, The direct approach to magnetic interpretation and its practical application: Geophysics, *14* p.290-320.

Riley, G. C., 1962, Stephenville Map-Area, Newfoundland: Geological Survey of Canada Memoir 323.

Rothery, D. A., 1982, Supervised maximum-likelihood classification and post-classification filtering using MSS imagery for lithological mapping in the Oman ophiolite: International Symposium on Remote Sensing of Environment, Second Thematic Conference, Remote Sensing for Exploration Geology, Fort Worth, Texas 1982.

Rothery, D. A., 1984, Reflectances of ophiolite rocks in the Landsat MSS bands: relevance to lithological mapping by remote sensing: Journal Geological Society London, v. 141 p.933-939.

Rothery, D. A., and Milton, D. J., 1981, Lithological discrimination in an ophiolite terrain: Landsat MSS imagery and reflectance measurements in Oman: *in* Allan, J. A., and

Bradshaw, M., eds., Remote sensing in geological terrain studies: Remote Sensing Society, London.

Rowan, L. C., Wetlaufer, P. H., Goetz, A. F. H., Billingsley, F. C., and Stewart, J. H., 1974, Discrimination of rock types and detection of hydrothermally altered areas in south-central Nevada by use of computerenhanced ERTS images: U. S. Geol. Survey Professional Paper 883, 35p.

Rowan, L. C., Goetz, A. F. H., and Ashley, R. P., 1977, Discrimination of hydrothermally altered and unaltered rocks in visible and near infrared multispectral images: Geophysics, v. 42, No. 3, p.522-535.

Rowan, L. C., and Lanthram, E. H., 1980, Mineral exploration, *in* Siegal, B. S., and Gillespie, A. R., eds., Remote sensing in geology: New York, Wiley, p.553-605.

Rowan L. C., and Kahle, 1982, Evaluation of 0.46- to 2.36-um Multispectral Scanner Images of the East Tintic Mining Distict, Utah, for Mapping Hydrothermally Altered Rocks: Economic Geology, V. 77, p.441-452.

Sawatzky, D. L., and Raines, G. L., 1982, Geologic use of linear-feature maps derived from small scale images: Basement Tectonics Symposium, 3rd, Salt Lake City, Utah, Proc., p.91-100.

Schilleref, S., and Williams, H., 1978, Geology of the Stephenville map area, Newfoundland: *in* Current Research, Part A, Geological Survey of Canada, Paper 79-1A, p.327-332.

Siegal, B. S., and Short, N. M., 1977, Significance of Operator Variation and the Angle of Illumination in Lineament Analysis on Synoptic Images: Modern Geology, v. 6, p.75-85.

Wells, R. E., Bouzane, J. P., and Roberts, B. A., 1972, Reconnaissance Land Classification of

the Corner Brook Area, Newfoundland: Newfoundland Forest Research Centre, St. John's, Newfoundland , Information Report N-X-83, 123p.

Williams, H., 1973, Bay of Islands map-area, Newfoundland: Geological Survey of Canada Paper 72-34.

Williams, H., 1975, Structural Succession, Nomenclature, and Interpretation of Transported Rocks in Western Newfoundland: Canadian Journal of Earth Sciences, 12, p. 1874-1894.

Williams H., and Smyth, W. R., 1973, Metamorphic aureoles beneath ophiolite suites and alpine peridotites; tectonic implications with west Newfoundland examples: American Journal of Science, 273, p.592-691.

Williams, H., Gillespie, R. T., and Napp, D. A., 1982, Geology of the Pasadena map area, Newfoundland: *in*Current Research, Part A, Geological Survey of Canada, Paper 82-1A, p. 281-288.

Williams, H., and Smyth, W. R., 1983, Geology of the Hare Bay Allochthon, *in*, Geology of the Strait of Belle Isle Area, Northwestern Insular Newfoundland, Southern Labrador, and Adjacent Quebec: Geological Survey of Canada Memoir 400, p.109-133.

IX. APPENDIX I

Radiometer Design

The following description of the Barringer-Magenta Hand Held Ratioing Radiometer (HHRR) is based upon an account by Gladwell *et. al.*(1983). The HHRR is designed to measure reflected light energy from a target in two passbands (channel 1 and channel 2) selectable in the range 400 to 2500nm. The reflected energy passes through two optical trains directed at the same target. A portion of the energy passes through a filter selected by the operator, after which the light is refocussed onto a thermoelectrically cooled PbS dectector. The filters used in this study extract the wavelength range which corresponds to the positions of the bands on the Multispectral Scanner and Thematic Mapper (Table 2). The liquid crystal digital display gives the analogue of the reflectance in each channel and the ratio of the two channels (channel 1/channel 2).

Measurement Technique

Prior to target reflectance measurement the instrument was claibrated against a standard of Fibrafax [5]. Calibration involved adjusting the amplification (gain) of each channel until the energy passing through each channel was equal and within the operating range of the instrument.

The instrument had previously been operated with narrow bandpass filters. This had necessitated an increase in the base amplification in order for the signal from the target to fall within instrument operation range. When the narrow bandpass filters were replaced with broad bandpass MSS and TM filters the signal was so amplified that it exceeded the instrument operation range on Fibrafax and could not be manually adjusted to within the range. The signal only fell outside the operating range of the instrument on Fibrafax, which has an extremely high reflectance, unlike the lithologics under examination. This required the adoption of a new lower reflectance standard, to permit instrument calibration. An ideal low-reflectance standard would have been Kodak grey paper. Alternatively netral density gelatin filters could have been used to reduce the overall reflectance energy entering the instrument. Niether of these were available in the field, thus four pieces of wood were sanded smooth and given two uniform coats of black paint. The new black standards were excellent, and their reflectances were much

---

[5]Fibrafax is the trade name of a non-asbestos insulating material manufactured by the Carborundum Company. Fibrafax has a high, spectrally diffuse reflectance in the visible and near infrared range.

closer to the lithological reflectances. These standards were calibrated to $BaSO_4$ and a correction applied to the data to account for variations from the flat uniform spectral response of $BaSO_4$.

The instrument was calibrated before and checked after each reading. If these readings differed significantly the measurement was re-taken.

The instrument was not operated under fluctuating cloud conditions, rain or low sun angles which caused shadowing. Readings were taken from directly above the sample and the instrument held steady on a tripod. Great care was taken to make sure the standard was horizontal during calibration and replaced in its exact location when checking for any fluctuations after each reading. All sets of readings were made on the same location.

X. APPENDIX II

A. Initial Data Costs

Digital Thematic Mapper Scene	3,465.00
Digital Multispectral Scanner Scene	1,050.00
Hard-Copy Multispectral Scanner Band 3 Image	80.00
Hard-Copy Radar L Band Image	U$ 45.00
Digital Regional Gravity Data	36.75
Digital Regional Aeromagnetic Data	355.00